THE UNIVERSITY *of* EDINBURGH

Design and Analysis of New Surface Wave Antennas for CubeSat and Other Small Satellites

Khalid Mubarak Alrushud

THE UNIVERSITY
of EDINBURGH

A thesis submitted for the degree of Doctor of Philosophy.
The University of Edinburgh.
November 2023

Abstract

The rise of small satellites, particularly CubeSats, has brought about the demand for innovative antenna solutions and compact circuit designs offering high performance at a low cost. Although these small satellites cannot fully replace traditional systems, they are reshaping the future landscape of space satellites. Technological advancements, including digital signal processing, micro-electromechanical systems, low-power programmable systems, integrated circuits, and miniaturisation, have enabled these satellites to efficiently handle increasingly complex tasks despite their small size. However, designing antennas for CubeSats poses distinct challenges, primarily related to size, weight, and power limitations, making it a crucial yet intricate aspect of these miniature satellite systems.

Researchers have explored innovative techniques such as integrating non-deployable antennas with solar panels on CubeSats, creating additional space for solar cells, sensors, and communication devices. While many SmallSat antennas radiate signals broadly, the direction in which these signals travel may not always align with the intended orientation of the CubeSat and in the required direction. For example, endfire antennas radiate electromagnetic fields precisely in the longitudinal direction of the antenna structure, making them potentially more suitable for CubeSat applications. These types of antennas can also offer a low aerodynamic drag profile, especially when compared to some broadside antennas, making them advantageous for other related practical scenarios such as on airplanes and cars.

In this thesis, the primary objective is to bridge the gap in high-gain antennas integrated with solar cells, particularly for high-frequency and endfire radiation applications. The focus is on possible techniques for integrating the solar panel aperture with the antenna to minimise space requirements on the CubeSat platform. Innovative planar configurations are introduced as efficient and low-profile antenna solutions for CubeSats and other Small Satellites, employing advanced concepts like substrate integrated waveguide (SIW) technology, surface wave (SW), and leaky wave (LW) principles. The first approach involves a leaky SIW T-junction for compact feeding, creating a uniform wavefront in a truncated parallel plate waveguide (PPW) section. This leads to the development of a planar quasi-endfire surface wave antenna (SWA) utilising the fundamental TM_0 SW mode at the edge of a grounded dielectric slab (GDS). To enhance performance, a sub-wavelength matching section (SMS) is added to ensure a smooth transition

between the PPW and GDS, improving antenna radiation characteristics. The measured prototype demonstrated realised gain values of 13.3 dBi at 18.6 GHz for a competitive structure size of $5\lambda_0 \times 4.8\ \lambda_0$ and with a simulated total radiation efficiency of 93.4%. The second approach focuses on achieving a truly endfire high gain antenna designed for 3U CubeSats. This design incorporates an air vias (AV) section and a dual-layer structure based on the distributed aperture principle. In the design, the transverse equivalent network (TEN) was applied and results are supported by the theoretical framework and the developed equations. This experimentally demonstrated antenna is fed by two leaky SIW T-junctions with a 180° phase shift between them and a common ground plane and an AV section with a fixed diameter to modify the relative permittivity. This enabled full, endfire radiation and the possibility to integrate solar cells. The measured prototype established a peak realised gain of 17.5 dBi at 18.6 GHz and with high radiation efficiency and low sidelobe levels. Lastly, an endfire high-gain antenna suitable for 1U CubeSats was also developed. This design employs an ungrounded substrate featuring AV sections with varying diameters, facilitating a gradual change in permittivity for minimal reflections to the air region. To feed this ungrounded substrate, a series of SIW horn antennas operating in phase are utilised in an array, ensuring optimal radiation performance and simple feeding. Simulation results show a directive endfire pattern with a directivity of 21.3 dBi at 24 GHz.

Lay Summary

Over the past two decades, the rapid growth of small satellites, particularly CubeSats, has been remarkable, with exponential expansion in the last five years. This surge in interest extends beyond academic and research circles including industry, government agencies, and military institutions. These organisations have enthusiastically embraced CubeSat space programs, often surpassing research initiatives conducted within universities. Consequently, while traditional satellite systems cannot be entirely replaced, the future vision for space satellites is undergoing a transformation, characterised by the development of more efficient and technologically advanced small satellites.

Antennas play a pivotal role in enhancing these satellite capabilities by enabling electromagnetic signal transmission and reception. The scientific community is actively engaged in designing innovative antenna systems that meet specifications for improved bandwidth and high data rates, all within the confines of CubeSat size and weight standards. Designing these antennas poses unique challenges due to the small satellite size and power limitations. Researchers have explored new methods for solar panel integration, especially when employing non-deployable antennas on CubeSats, maximising space for additional solar cells, sensor technologies, and communication devices.

Within this context, endfire antennas emerge as a possible solution. Unlike broadside antennas that radiate in a direction perpendicular to the aperture, endfire antennas direct electromagnetic fields into free space and along the direction of the antenna structure. These antennas are advantageous for CubeSats, particularly concerning their physical placement on the satellite. For example, endfire antennas can send a signal downward toward the Earth while solar panels can be positioned for best possible solar power collection. Additionally, they offer a low aerodynamic drag profile, especially when compared to broadside antennas in specific practical applications.

This thesis introduces novel solutions to these CubeSat and Small Satellite antenna challenges, presenting planar configurations that offer efficient and low-profile options. These antennas provide quasi and full endfire beam patterns, for solar cell integration and high-gain capabilities. These configurations represent a significant advancement in the field of CubeSat antennas,

supported by comprehensive theoretical analysis, full-wave simulations, and experimental measurements for proof-of-concept demonstrators.

Declaration of originality

I hereby declare that the research recorded in this thesis and the thesis itself was composed and originated entirely by myself in the Institute for Imaging, Data and Communications (IDCOM) in the School of Engineering, The University of Edinburgh. The thesis has not been submitted, either in whole or in part, in any previous application for a degree. Except where it states otherwise by reference or acknowledgment, the work presented is entirely my own.

Acknowledgements

First and foremost, I am very grateful to Almighty God, Allah, for blessing me and giving me the strength, and knowledge to achieve this significant milestone.

I sincerely express my deep sense of gratitude to my supervisor, Dr Symon K. Podilchak, for his endless support and valuable advice through this remarkable journey. I thank him for his technical and mental help over all these years, specifically during the pandemic. I am short of words to thank him for being very patient, supportive, and very helpful during the entire time of my research. He believed in me, and his motivation and guidance helped me to build my skills as an academic researcher. Our weekly meetings have been inspirational to me. I will always be grateful to him.

I would also like to thank the Examination Committee, Prof Antonis Giannopoulos, and Dr Masood Ur Rehman for their time and effort in evaluating the thesis. Their valuable comments have helped and improved the quality of the work.

To my great parents, Tarfah and Mubarak, who raised me with heartfelt love and guidance and provided incredible support and encouragement to follow my dreams. I am forever indebted to you for giving me the opportunities and experiences that have made me who I am. I would never be able to thank you enough. Many thanks also to my family, Norah, Noha, Haya, Hind, Ahmad, Abdullah, and Mohammed, for your support and encouragement.

I would like to express my heartiest thanks to Bandar Alshammari, my dearest colleague in KACST and Edinburgh University and my friend for his support and motivation that helped me through this journey. A special thanks to my colleagues and friends at The University of Edinburgh and Heriot-Watt University. Especially Dr Victoria Gómez-Guillamón Buendía, Dr Maksim Kuznetcov, Dr Zain Shafiq, Dr Khaled Aliqab, Dr Abdulmalik Aldharrab, Dr Michael Sheehan, Dr Hussien Alrakah, Mazen Almalki, Dr Meshari Alsharari, Dr Kostas Kossenas, Dr Cristian Alistarh, Callum Hodgkinson, Alexander Don, Iram Shahzadi, Sadia Riaz, Aqsa Ahmad, and many more... I'm confident I may have overlooked some individuals, and I apologize for this, it was a long and challenging journey and you helped me through it. All in all, it has been a delightful adventure, filled with countless hours of engaging discussions, mutual learning, and continuous support from one another.

To all my friends in the UK, thank you for making this journey a very joyful time. Especially Dr Ghazi Alanazi, Dr Yousef Almajed, Dr Abdulaziz Alomiery, Raied Alotaibi, Khalid Alyousef, Khalid Alfawzan, Dr Mohammed Alqarni, Mohammed Alnefaie, Ebraheem Alanazy, and Abdullah Bin Girad.

Lastly, but certainly not least, special thanks go to the Saudi government and King Abdulaziz City for Science and Technology (KACST) who sponsored my postgraduate study and gave me this great chance.

Contents

Abstract . . . ii
Lay Summary . . . iv
Declaration of originality . . . vi
Acknowledgements . . . vii
Contents . . . ix
List of figures . . . xi
List of tables . . . xvi
Acronyms and abbreviations . . . xvii
List of Symbols . . . xix

1 Introduction **1**
1.1 Goals and Motivation . . . 1
1.2 Methodology of the Research . . . 2
1.3 Thesis Outline . . . 5

2 Background **7**
2.1 Small Satellite Antennas . . . 7
2.2 State-of-the-art Antenna Review . . . 10
2.2.1 Low Gain Antennas . . . 10
2.2.2 High Gain Antennas . . . 13
2.2.3 Challenges for Small Satellite Antennas . . . 20
2.3 Relevant Background Theory . . . 25
2.3.1 Substrate Integrated Waveguide Overview . . . 26
2.3.2 Overview of Surface Waves and Surface wave Antennas . . . 28
2.3.3 Leaky Waves Overview . . . 35
2.4 Summary . . . 40

3 Compact Substrate Integrated Waveguide Quasi-EndFire Antenna **41**
3.1 Introduction . . . 41
3.2 An Overview of Previous Works and Challenges with Compact CubeSat Antennas 41
3.3 Chapter Overview . . . 43
3.4 Antenna Design Approach . . . 44
3.4.1 Leaky SIW T-Junction . . . 44
3.4.2 Matching Section and GDS . . . 51
3.4.3 Microstrip to SIW Transition . . . 54
3.4.4 Excited Fields and Modes . . . 55
3.5 Simulations and Measurements . . . 57
3.6 Summary . . . 62

4 Planar Surface Wave Antenna with Directive Radiation Exactly at Endfire **63**
4.1 Introduction . . . 63
4.2 Background Literature . . . 63
4.3 Chapter Overview . . . 64

4.4 Motivations, Analysis & Design . . . 67
4.4.1 Radiation Principles by Cascaded Matching & Guidance . . . 68
4.4.2 Transverse Equivalent Network for the Proposed SWA . . . 70
4.5 Design, Simulation Results, & Discussions . . . 74
4.5.1 Single-layer Design & Operation . . . 75
4.5.2 Operation of the Dual-layer Design . . . 78
4.5.3 Comparison of the Single-Layer and Dual-Layer Designs . . . 80
4.5.4 Feeding Considerations and Practical Implementation . . . 82
4.6 Experimental Validation & Discussions . . . 84
4.7 Summary . . . 91

5 Optically Semi-Transparent Planar Endfire Antenna 93
5.1 Introduction . . . 93
5.2 Background Literature . . . 94
5.3 Overview of the Proposed Design . . . 96
5.4 Approach to Designing the SWA . . . 97
5.4.1 Determination of the Effective Relative Dielectric Constant with the Air Via (AV) Sections . . . 98
5.5 Ideal Feeding for the SWA . . . 100
5.6 Practical Feeding Approaches For the SWA . . . 102
5.6.1 SIW Horn Feeding . . . 103
5.6.2 Design A . . . 104
5.6.3 Design B . . . 104
5.6.4 Comparison Between Designs A, B, and C . . . 105
5.7 SIW Horn Array Feeding . . . 107
5.8 Summary . . . 112

6 Conclusion and Future Work 114
6.1 Conclusions . . . 114
6.2 Key Contributions . . . 115
6.3 Future Work . . . 117

A List of Publications 119

B Transverse Equivalent Network Codes 121
B.1 Calculating Z_{SMS} Code . . . 121
B.2 Calculating Z_{SW} Code . . . 123
B.3 Calculating Z_{AV} Code . . . 124
B.4 Generating α_{LW} and β_{LW} using TEN Code . . . 124

C Application to Millimetre-wave Structures 129

D Feeding Considerations and Practical Implementation 133
D.1 Microstrip Line Feeder . . . 133
D.2 RF Connector . . . 135

References 137

List of figures

1.1 (a) CubeSat with an antenna and solar panel system (a) separated, and (b) integrated. . . . 2
1.2 Diagram of a CubeSat with an endfire antenna integration. . . . 3

2.1 Kinds of antennas for CubeSats that been achieved by the scientific community. LGAs and HGAs. . . . 10
2.2 General design steps for CubeSat antennas. . . . 22
2.3 (a) Section of an SIW configuration, and (b) its equivalent dielectric loaded waveguide. . . . 27
2.4 Diagram of SW propagation considering a GDS. . . . 31
2.5 (a) The schematic of the TEN model for the GDS structure, and (b) the equivalent structure for the GDS. . . . 33
2.6 The normalised TM_0 SW mode phase propagation constant for the GDS with $\epsilon_r = 2.2$ and $h = 1.575$ mm for the frequency from 0 to 300 GHz. . . . 34
2.7 Examples of different types of LWAs. . . . 37
2.8 An SIW LWA and its radiation principle. . . . 38
2.9 Illustration of LWs considering a GDS, where the bound fields are perturbed by the periodic structure at the air-dielectric interface, causing them to radiate. . . . 39

3.1 (a) Examples of the placement of the proposed antenna on a 1U CubeSat illustrating the quasi-endfire beam pattern, (b) top-view of the proposed endfire antenna structure defining the design parameters and sections. As illustrated in (a), a solar panel array could also be placed on top of the planar antenna if the microstrip-SIW feedline is removed and the structure is excited by a vertical probe. This is possible because the covered part of the SWA would all be metal. 43
3.2 The simulated electric-field distribution inside the conventional SIW T-junction; i.e. in the middle of the slab. . . . 45
3.3 Simulated electric field showing a uniform distribution within the PPW, the SMS, and the GDS. . . . 46
3.4 TEN circuit model and the normalised LW phase and attenuation constants. The splitting-condition; i.e., $\alpha \approx \beta$ can be observed at ≈18 GHz. . . . 47
3.5 (a) Diagram showing the unit cell consisting of one via which forms the PRS while two vias form the PEC, (b) simulated electric field for 3 and 4 unit cells where it can be noticed that the field has leaked into the PPW region, and (c) results of the normalised LW phase and attenuation constants using Bloch analysis and numerically determined using Matlab. . . . 48
3.6 Normalised LW phase and attenuation constants analysis for different values of (a) W_{WG}, and (b) P_{PRS} . . . 52
3.7 Simulated and measured beam patterns in the yz plane ($\phi = 90°$). Measured results are plotted at 18.6 GHz. Dashed lines represent the simulated beam patterns without the SMS and without the PPW and SMS. The simulated 3D pattern is also reported (right). . . . 58

3.8 Reflection coefficient versus frequency for the designed SWA (see inset). It should be pointed out that initial simulations were completed considering $\epsilon_r = 2.2$ (blue solid line) while the green lines consider practical permittivity tolerances. Simulations on the CubeSat body are also reported. 59
3.9 Screenshot of CST simulation model of the proposed antenna with the CubeSat. 59
3.10 Measured and simulated maximum RG in the yz plane. 60
3.11 Simulated and measured beam patterns in the xy plane ($\theta = 90°$). 60
3.12 Measured beam patterns for different frequencies from 18.1 to 18.7 GHz in the yz plane ($\phi = 90°$). 61
3.13 Top and bottom views of the CST mesh calculation screenshot for the proposed antenna structure. 61

4.1 Top and bottom view of the proposed SWA were the different sections for the structure are defined. Note: both sides of the SWA are analogous. 65
4.2 (a): Cross-section view for the SWA where the two dielectric layers are illustrated as well as the ground plane and input microstrip lines (top and bottom). This basically defines two stacked SWAs with a common ground plane. (b): Top or bottom view for the SWA where the optimised dimensions are outlined (see Table 4.1). (c): Photograph of the fabricated prototype. 66
4.3 Examples of possible placement for the proposed SWA on a 3U CubeSat: (a) 3D and front view where the SWA is placed on one side of CubeSat with the solar cells integrated underneath the AV section and on top of the GDS region, (b) 3D, front, and back views where the SWA and solar cells are deployed. . . . 69
4.4 TEN circuit model and the corresponding SWA. Note the common colours for each part of the SWA within the TEN circuit and highlighted for the representative section. 71
4.5 Numerically determined attenuation and phase constants, α_{LW} and β_{LW}, respectively, for the leaky SIW T-junction feeder representing the complex solution for the TRE (with k_0 normalisation). Results show that the SWA is designed to work at about 18 GHz. 74
4.6 Single-layer SWA simulations: (a) normalised beam patterns in the yz plane ($\phi = 90°$), and (b), the reflection coefficient versus frequency. A comparison is made with 22 rows for the AV section and without the AVs. 77
4.7 Single-layer SWA simulations (42 rows of AVs and a GDS length of 68 mm or $24\lambda_g/4$): RG pattern in (a) the yz plane ($\phi = 90°$) and (b) the xy plane ($\theta = 90°$). The design was optimised (and compared against a variety of single-layer structure dimensions), however, a beam maximum directly at endfire with low SLLs was not achieved. This problem was overcome with the proposed two-layer SWA (see patterns in Figure 4.9). 78
4.8 Examined double-layer SWAs with a different number of rows for the AV section defining S_4: (a) 22, (b) 42, and (c) 62. All other dimensions as defined in Table 4.1. 79
4.9 Simulated RG in the (a) yz plane ($\phi = 90°$), and, (b) the xy plane ($\theta = 90°$) for the different number of AV rows (see Figure 4.8). 80

4.10 Comparison of the single-layer and double-layer SWA for various cases. In particular, the electric field is shown for the longitudinal cross-section view within the structure and the air region (for the near-field, and in the yz plane): without the AVs and no SMS, without the AVs and with the SMS, with 22 rows of AVs and without the SMS, and, with 22 rows of AVs and with the SMS. . . . 81
4.11 Simulated maximum RG versus frequency for the single- and dual-layer SWA structures with 22, 42, and 62 rows for the AV section: (a) the yz plane ($\phi = 90^\circ$) and (b) the xy plane ($\theta = 90^\circ$). 82
4.12 (a): Simulated MLD versus frequency for single- and dual-layer SWA structures with 22, 42, and 62 rows for the AV section in the yz plane. (b): Sames as (a), but SLL. 83
4.13 Simulated efficiency: (a) radiation and (b) total antenna efficiency. 83
4.14 Manufactured prototype: (a) top and (b) bottom views of the dual-layer SWA. Also shown in (c) is the far-field measurement setup, and (d) a photograph of the fabricated proof-of-concept structure with its external 180° coupler enabling differential feeding. 85
4.15 Reflection coefficient versus frequency for the dual-layer SWA. It should be mentioned that simulations were initially completed considering ϵ_r = 2.2 (blue line), while the green, yellow, and purple lines consider a practical shift in the value of the relative dielectric constant and are within the tolerance for the PCB material. Measurements also shown (red and black lines) for the top and bottom layers. 86
4.16 Measured and simulated maximum RG versus frequency in: (a) the yz plane ($\phi = 90^\circ$) and (b) the xy plane ($\theta = 90^\circ$). 87
4.17 Gain patterns in the yz plane ($\phi = 90^\circ$). Results are 17.7 dBi and 17.5 dBi for the simulated and measured peak gain, respectively. 88
4.18 Gain patterns in the xy plane ($\theta = 90^\circ$). Results are 17.7 dBi and 17.4 dBi for the simulated and measured peak gain, respectively. 89
4.19 Measured beam patterns for different frequencies from 18.0 to 18.6 GHz in the yz plane ($\phi = 90^\circ$) and the xy plane ($\theta = 90^\circ$). 89
4.20 Top and bottom views of the CST mesh calculation screenshot for the proposed dual-layer SWA structure. 90

5.1 Example of the possible placement for the proposed SWA array on a 1U CubeSat is depicted, showing 3D, front, and back views with the integration of solar cells underneath the AV section. 94
5.2 Top view for the AV sections where the optimised dimensions and where different AV sections are outlined. 96
5.3 Comparison of the ungrounded and grounded dielectric slab antenna structures. The electric field is shown for the longitudinal cross-section view within the structure and the air region (for the near-field, and in the yz plane). For the ungrounded case, the fields are clearly shown to be radiated in a more directive orientation at the end of the substrate, and this can lead to a more directive far-field beam pattern. 98
5.4 Top and bottom views of the proposed antennas with large wave ports are shown: (a) with AV sections and a short GDS, (b) without AV sections and with a short GDS, and (c) without AV sections and with a full ground. 101

5.5 Simulated 3D patterns for the proposed antennas with large wave ports are shown: (a) with the AV sections and a short GDS, (b) without AV sections and with a short GDS, and (c) without AV sections and with a full ground. . . 101
5.6 Simulated beam pattern in (a) the yz plane ($\phi = 90°$) and (b) the xy plane ($\theta = 90°$) for the studied antennas with large wave ports. 102
5.7 Top and bottom views of the proposed antennas with a single SIW horn are shown: Design A: with straight rows of AV sections, Design B: with curved rows of AV sections, and Design C: with curved rows on the sides and straight rows in the middle of the AV sections. 103
5.8 Simulated beam pattern for different frequencies from 21 to 24 GHz in (a) the yz plane ($\phi = 90°$) and (b) the xy plane ($\theta = 90°$) for the proposed Design A antenna (see Figure 5.7). 104
5.9 Simulated beam pattern for different frequencies from 21 to 24 GHz in (a) the yz plane ($\phi = 90°$) and (b) the xy plane ($\theta = 90°$) for the proposed Design B antenna (see Figure 5.7). 105
5.10 Simulated 3D patterns at 24 GHz for the proposed antennas with a single SIW horn (see Figure 5.7) are shown: Design A: with straight rows of the AV sections, Design B: with curved rows of AV sections, and Design C: with curved rows on the sides and straight rows in the middle of AV sections. 106
5.11 Simulated beam pattern in (a) the yz plane ($\phi = 90°$) and (b) the xy plane ($\theta = 90°$) for the proposed antennas Designs A, B, and C with a single SIW horn at 24 GHz (see Figure 5.7). 106
5.12 (a) Top and (b) bottom views for the proposed antennas with an array of eight SIW horns with AV sections. 108
5.13 Simulated beam pattern for different frequencies from 21 to 24 GHz in (a) the yz plane ($\phi = 90°$) and (b) the xy plane ($\theta = 90°$) for the proposed antenna with an array of eight SIW horns with AV sections. 109
5.14 Simulated 3D patterns for the proposed antennas with an array of eight SIW horns: (a) with AV sections, (b) without AV sections. 110
5.15 Simulated beam pattern in (a) the yz plane ($\phi = 90°$) and (b) the xy plane ($\theta = 90°$) for the proposed antenna with an array of eight SIW horns at 24 GHz with and without AV sections. In the yz plane, the SLL are at -9.2 dB and -4.7 dB for the structures with and without AV sections, respectively. Additionally, in the xy plane, the SLL for both structures is -11 dB. 110
5.16 Top and bottom views of the CST mesh calculation screenshot for the proposed semi-transparent SWA structure. 111

C.1 Numerical α and β calculations for the modelled SIW antenna feeder and loading defined by the different SW guiding sections (see Figure 4.1). In particular, the normalised LW phase constant β/k_0 is in blue and α/k_0 in red: (a) original 18 GHz design, (b) validation design 1 (55 GHz), (c) validation design 2 (77 GHz), and (d) validation design 3 (110 GHz). These results show the complex solution of the TRE (see Equation 4.1) defined by the proposed TEN as in Figure 4.4. 129
C.2 Simulated reflection coefficient versus frequency for the various microwave and millimetre-wave frequency designs 130

C.3 RG patterns in (a) the yz plane ($\phi = 90^\circ$) and (b) the xy plane ($\theta = 90^\circ$) for the various microwave and millimetre-wave frequency designs. Very consistent peak gain values and patterns are shown, and all with low SLLs and radiation exactly at endfire. 130

D.1 Possible microstrip line structures for the SWA, (a) straight microstrip line, (b) 10 mm 90° curve microstrip line, (c) spline microstrip line, (d) 20 mm 90° curve microstrip line, and (e) full 90° curve microstrip line. 134
D.2 Simulated reflection coefficient versus frequency for the different proposed microstrip line structures for the SWA. 134
D.3 Simulated electric field inside the substrate for the different microstrip feeding considerations, (a) straight microstrip line, (b) 10 mm 90° curve microstrip line, (c) spline microstrip line, (d) 20 mm 90° curve microstrip line, and (e) full 90° curve microstrip line. 135
D.4 Simulated beam pattern in (a) the yz plane ($\phi = 90^\circ$) and (b) the xy plane ($\theta = 90^\circ$) for the dual-layer SWA with 42 rows of AVs and 68 mm GDS dimension with straight microstrip line, full 90° curve microstrip line with and without RF connector. 136
D.5 Simulated reflection coefficient versus frequency for the dual-layer SWA design. 136

List of tables

2.1 Low gain antennas (LGAs) comparisons. 14
2.2 High gain antennas (HGAs) with small stowage volume comparisons. 17
2.3 High gain antennas (HGAs) with large stowage volume comparisons. 20

3.1 Gain and SLL for the designed SWA with different numbers of patches per row (see Figure 3.1(b)) in the yz plane ($\phi = 90^\circ$) and the xy plane ($\theta = 90^\circ$) at 18 GHz. 53
3.2 Endfire Antenna Comparisons (Optimized Results) 60

4.1 SWA Dimension for the Structure as Illustrated in Figure 4.2 (Dimensions in Millimetres) 68
4.2 Single-Layer SWA Performance for Different Lengths of the PPW Section . . . 76
4.3 Single-Layer SWA Performance for Different Lengths of the GDS Section . . . 76
4.4 Single-Layer Directivity & MLD for Different Number of Rows for the AV Section 77
4.5 Double-Layer SWA Performance for Different Number of Rows for the AV Section 80

5.1 Parameters values for the proposed antenna with eight AV sections (see Figure 5.2). 100
5.2 Directivity and SLL for the three design structures (see Figure 5.7) in the yz plane ($\phi = 90^\circ$) and the xy plane ($\theta = 90^\circ$) for four frequencies: 21, 22, 23, and 24 GHz. 107
5.3 Directivity and SLL for the designs structures with single and array SIW horn in the yz plane ($\phi = 90^\circ$) and the xy plane ($\theta = 90^\circ$) for the wanted frequency 24 GHz. 111

6.1 Endfire Surface Wave Antennas Comparisons 115

C.1 Numerically Determined Dimensions for the SWA Considering the Original Design & Three Other Validation Frequencies: 55 GHz, 77 GHz, and 110 GHz . 131

Acronyms and abbreviations

1D	One-dimensional
2D	Two-dimensional
3D	Three-dimensional
1U	One CubeSat unit volume
2U	Two CubeSat unit volumes
3U	Three CubeSat unit volumes
4U	Four CubeSat unit volumes
6U	Six CubeSat unit volumes
12U	Twelve CubeSat unit volumes
RF	Radio frequency
PCB	Printed circuit board
PEC	Perfect electric conductor
BW	Bandwidth
SIW	Substrate integrated waveguide
LW	Leaky wave
SW	Surface wave
LWA	Leaky wave antenna
SWA	Surface wave antenna
SWL	Surface wave launcher
HGA	High gain antenna
LGA	Low gain antenna
CP	Circular polarisation
SLL	Sidelobe level
TRT	Transverse resonance technique
TRE	Transverse resonance equation
TEN	Transverse equivalent network
HF	High frequency
VHF	Very high frequency
UHF	Ultra high frequency

GDS	Grounded dielectric slab
PRS	Partially reflective screen
TE	Transverse electric
TEM	Transverse electromagnetic
TM	Transverse magnetic
PPW	Parallel-plate waveguide
SMS	Sub-wavelength matching section
AV	Air via
RG	Realised gain
MLD	Main lobe direction

List of Symbols

ϵ_0	Permittivity in free-space
ϵ_r	Permittivity in the dielectric
$\epsilon_{r_{eff}}$	Relative effective permittivity
μ_0	Permeability in free-space
μ_r	Permeability in the dielectric
k_0	Wavenumber in free-space
λ_0	Wavelength in free-space
λ_g	Guided wavelength
ω	Angular frequency
γ	Complex propagation constant
α	Attenuation constant or leakage rate
β	Phase propagation constant
c	Speed of light
f_c	Cutoff frequency
f	Operation frequency

Chapter 1
Introduction

This chapter will briefly outline the motivation behind the development of CubeSats antennas in this thesis. Additionally, it will outline the goals of this thesis in terms of designing antennas for CubeSats and other small satellites. The chapter then discusses the research methodology, and describes the approach taken. Furthermore, the structure and content of the thesis are detailed, providing a clear roadmap for the reader.

1.1 Goals and Motivation

Recent advancements in satellite antenna technology emphasise integration, including innovations like higher frequency bands, optical communication, expanded bandwidth (BW), and integration with personal and wireless services [1] - [5]. The future of antenna systems includes hybrid designs capable of producing specific high-gain radiation patterns, offering wide scanning capabilities and precise beam shaping [4]. CubeSats, a distinct category within SmallSats, are compact satellites measuring 10 x 10 x 10 cm^3 and weighing approximately 1 kg, utilising commercially available components [6]. Moreover, CubeSat system-level specifications are typically defined by the standard volume of one CubeSat unit (1U) [1], [3], [7]. Although not poised to fully replace larger satellites, CubeSats significantly complement them and can be made into a network, finding applications in scientific missions, Earth observation, telecommunications, weather forecasting, navigation, technology demonstrations, and education. Their potential is substantial, especially with ongoing technological advancements, enabling them to undertake missions of significant scientific and commercial importance [6].

The motivation behind this research is to integrate the solar panel aperture with the antenna to minimise space requirements on the CubeSat platform. This is illustrated in Figure 1.1. More conventionally, CubeSat antennas have been designed for broadside radiation. The goal of this research is to propose and design novel antennas tailored for CubeSats and other SmallSats. These new antennas aim to address the gap in CubeSat antenna design by enabling integration

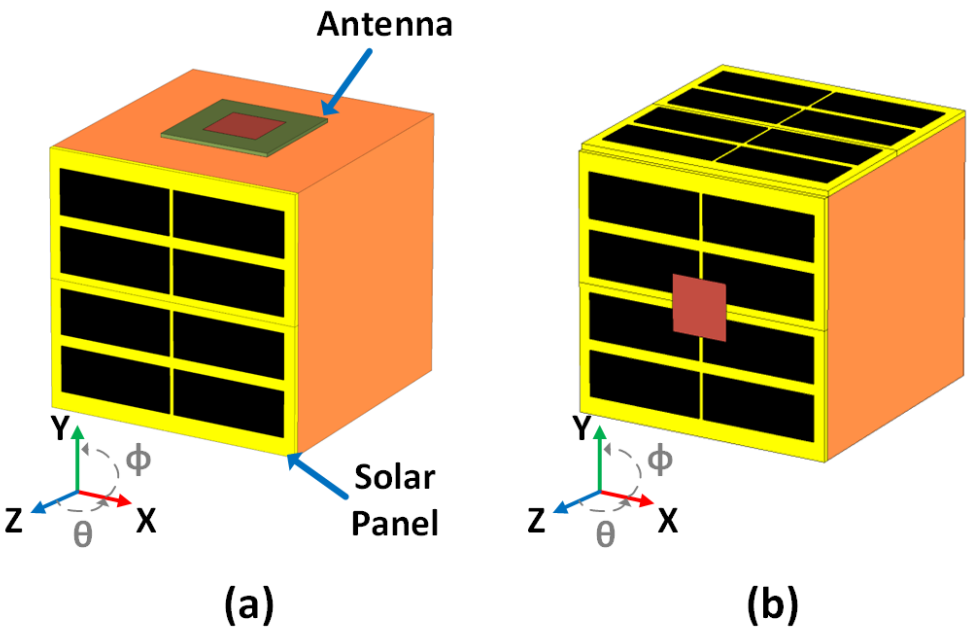

Figure 1.1: *(a) CubeSat with an antenna and solar panel system (a) separated, and (b) integrated.*

with the solar panel aperture while offering high gain and endfire radiation capabilities, particularly at higher frequencies. Figure 1.2 illustrates the usefulness of designing an antenna with endfire radiation and integrating it with the solar panel. This antenna placement with endfire beam patterns can provide increased link connectivity, while being connected to the Earth ground station, and therefore allow light rays from the Sun to radiate onto the solar cells simultaneously. To the best knowledge of the author, no similar antenna structures as reported in this thesis have been reported previously.

1.2 Methodology of the Research

To achieve these goals, a comprehensive examination of the current challenges encountered by CubeSats and other small satellites was completed, with a particular emphasis on technologies that are highly affected by these limitations due to their physical attributes. Once the identified challenges were well understood, the design process commenced, which can be outlined in the following stages:

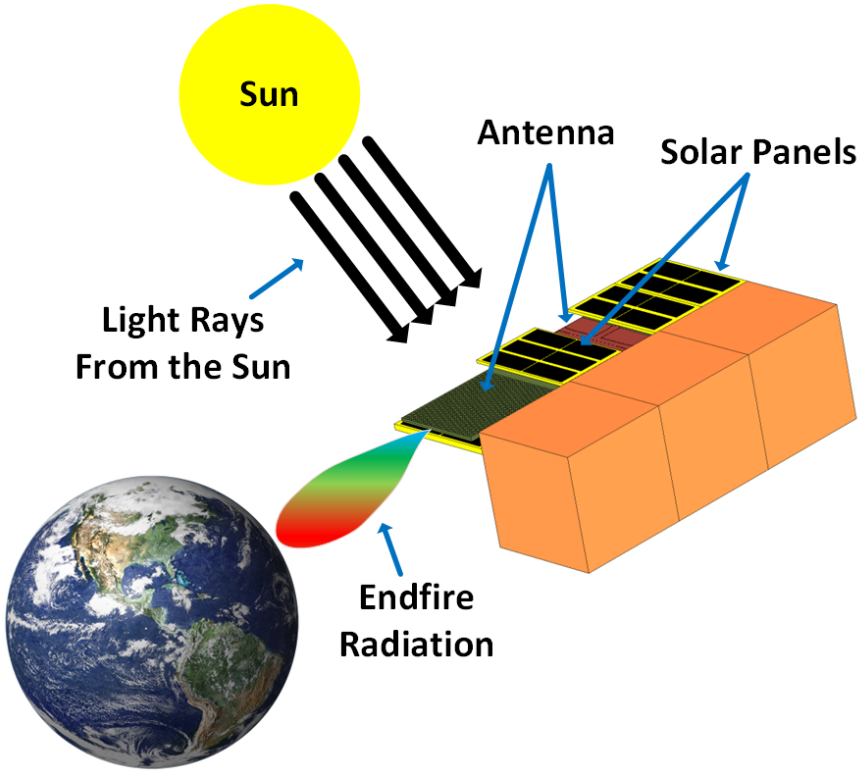

Figure 1.2: *Diagram of a CubeSat with an endfire antenna integration.*

Theoretical Analysis

The purpose of these analyses is to validate the feasibility of the proposed antenna systems and establish a robust starting point for their optimal design. Theoretical methods such as mode propagation, dispersive analysis, Bloch analysis, transverse resonance networks (TRN), radiated field calculations and impedance matching [8] were explored. These analyses were completed utilising software tools such as Matlab [9] and Mathematica [10].

Full-wave Simulations

Full-wave simulations were conducted using the electromagnetic solver CST, short for Computer Simulation Tool [11]. Full-wave solvers serve as the foundational computational engines in CST Studio Suite and similar software packages. These solvers comprehensively solve Maxwell's equations, considering all electromagnetic phenomena such as reflection, refraction, diffraction, scattering, and absorption. CST Studio Suite offers a comprehensive platform for electromagnetic simulation across various applications, including antennas, RF/microwave components, and high-speed digital systems [12]. Featuring a user-friendly interface, it provides a wide range of tools for model setup, simulation, and post-processing. Additionally,

CST Studio Suite offers various simulation tools for electromagnetic analysis, encompassing both time-domain and frequency-domain solvers [12].

Time-domain solvers, such as the Finite Integration Technique (FIT) used in CST, directly solve Maxwell's equations in the time domain. They discretize both space and time into a grid of cells and iteratively update the electromagnetic fields over small time steps. This approach enables accurate modelling of transient electromagnetic phenomena and wideband signals [12]. On the other hand, frequency-domain solvers, such as the Finite Element Method (FEM) and Method of Moments (MoM) in CST, analyse electromagnetic fields in the frequency domain. They decompose Maxwell's equations into algebraic equations and solve them at specific frequencies. Frequency-domain solvers are well-suited for analysing resonant structures and steady-state responses [12]. The simulations in this thesis utilised the frequency domain solver, which dissects the structure into small triangles to derive straightforward equations. These equations are then assembled into a comprehensive system representing the discretized structure and the antenna under design and study.

The outcomes from these simulations were employed to validate theoretical concepts and refine design parameters. Parametric simulations were employed for design optimisation, and field sources were placed to capture 2D near-field profiles and far-field radiation patterns.

Manufacturing and Measurements

The various configurations discussed in this thesis were fabricated using printed circuit boards (PCBs), which were externally and internally etched by Printech Circuit Laboratories Limited and the Electrical and Mechanical Workshop at the University of Edinburgh. Subsequently, measurements were conducted in the Microwave Labs at the University of Edinburgh and Heriot-Watt University, utilising available equipment, including a calibrated anechoic chamber, Diamond far-field acquisition software, 2-port and 4-port vector network analysers (VNAs), and other instrumentation for testing microwave PCBs and antennas.

Post-processing

Post-processing involves comparing the measured outcomes with theoretical predictions and simulations to validate the concepts. Matlab [9] was employed as the primary tool for this analysis.

1.3 Thesis Outline

The remainder of this thesis is organised as follows:

Chapter 2

This chapter outlines the needed background framework for this thesis. It offers a comprehensive survey of the existing landscape of CubeSat antennas, categorising them into low-gain antennas (LGAs) and high-gain antennas (HGAs) according to their gain levels. The chapter delves into the challenges faced in the domain of small satellite antennas. Additionally, it provides a detailed exposition of pertinent background theories, including SIWs, surface waves (SWs), leaky waves (LWs), and explains the fundamental principles of the transverse resonance technique (TRT) and the transverse resonance equation (TRE).

Chapter 3

In this chapter, a novel and planar quasi-endfire SWA utilising SIW technology for integration with CubeSats and other small satellites is introduced. This antenna achieves a quasi-endfire beam pattern through the radiation of the fundamental TM_0 SW mode at the edge of a grounded dielectric slab (GDS). This mode is excited via a leaky SIW T-junction, generating a uniform wavefront that travels through a truncated parallel-plate waveguide (PPW). To enhance antenna performance, a matching section, employing an array of sub-wavelength patches, is incorporated at the PPW-GDS interface, reducing reflections and improving radiation characteristics. Additionally, this chapter illustrates the TEN circuit model and presents the normalised LW phase and attenuation constants derived through the TRE. Furthermore, an alternative method for determining the LW phase and attenuation constants, utilising CST results, is introduced using Bloch analysis [8].

Chapter 4

In this chapter, the primary objective is to develop a highly competitive truly endfire high-gain antenna suitable for 3U CubeSat applications. This goal is achieved through the introduction of the AV section, using the distributed aperture principle defining the dual-layer structure, and the application of TEN methodologies by applying the relevant theory and deriving the needed equations. The antenna is fed by two leaky SIW T-junctions with a 180° phase shift between them. These T-junctions establish a uniform wavefront that propagates through a truncated PPW, as outlined in Chapter 3. To optimise the endfire pattern of the antenna, a series of

matching sections are introduced. This sequence commences with a sub-wavelength matching section (SMS) positioned between the PPW and the GDS to ensure a seamless transition for the phase constant and this minimises reflections. Additionally, a grounded AV section with a fixed diameter is incorporated to modify the relative permittivity, simplifying the field transition from the GDS to the air region for endfire radiation. The chapter further includes numerical modelling employing the transverse resonance technique (TRT). This modelling is applied to the TEN, primarily to ascertain the operating frequency for the SWA while extracting the LW phase and attenuation constants, crucial in defining the feeder. Moreover, this modelling guarantees a smooth field transition for the propagating field at the end of the structure, ensuring optimal endfire radiation.

Chapter 5

In this chapter, a planar optically semi-transparent endfire antenna will be introduced, designed also based on SIW technology and TM_0 SWs. Utilising an ungrounded dielectric slab featuring eight AV sections, the antenna achieves an endfire beam pattern, ensuring seamless transitions and minimal reflections in the air region. The feeding process for this antenna involves several stages, spanning from the theoretical ideal feeding concepts to practical applications involving both single and arrays of SIW horns. Within this chapter, three distinct designs (Design A, B, and C) featuring different arrangements for the AVs on the ungrounded dielectric slab are proposed. This ungrounded dielectric slab, fed by eight SIW horns, forms the final SWA configuration, characterised by high-gain endfire radiation and integrated solar cells, making it suitable for 1U CubeSat applications. This configuration can support high data rate capabilities for downlink communications in CubeSats.

Chapter 6

The last chapter provides a conclusion, summarising the primary contributions of the thesis, and explores possible activities for future research.

Chapter 2
Background

2.1 Small Satellite Antennas

High-performance satellites were dominant in the space industry, which might have heavy and expensive payloads, to deliver high-quality services. The timeline for the lifecycle of large conventional satellites, from proposal to launch, is subject to considerable variation based on factors such as mission complexity, funding accessibility, regulatory clearances, technical limitations, and the availability of launch vehicles. Nevertheless, a standard duration for this process typically falls within 5 to 10 years. These satellites are generally of high cost, i.e. starting from 100 million US dollars to 2 billion US dollars depending on the satellite itself [1]. However, in the last twenty years, small satellites have grown dramatically; CubeSats in particular, have increased exponentially in the previous five years. Additionally, the university and research sectors are not the only sectors which are excited about CubeSats. Industries are also interested in these SmallSats; for instance, commercial businesses, government agencies and military institutions have CubeSat space programs. As a matter of fact, these sectors latterly override the research done at universities relating to CubeSats today. As a result of this increase and while typical satellite systems cannot be entirely replaced by SmallSats, the future vision for space satellites is starting to develop [1], [2].

From a mechanical point-of-view, the CubeSat standard consists of one cube or more and every single cube should be 10 x 10 x 10 cm^3, while the mass should not be more than 1.33 kg. Additionally, CubeSat system-level specifications are typically defined by this standard volume; i.e. one CubeSat unit volume (1U) [1], [3], [7]. Following this standard, the Picosatellite platform has also evolved, defined by a 5 x 5 x 5 cm^3 volume. This technology started in 1999 by engineers at Stanford University and California Polytechnic State University as a method to introduce students to the practical process of designing, fabrication, integration, launching and operation of satellites [3]. Since this time, modern technology evolution has improved the capabilities of these small satellites enabling them to be more efficient and to do more complex functions based on their size. There has also been significant commercialisation of

small satellite networks by industry such as the Starlink Network [13]. Moreover, examples of the added technologies on the CubeSat platforms are additional digital signal processing, micro-electromechanical systems, low-power programmable systems, integrated circuit inclusions, and miniaturisation.

Antennas are one of the critical components that enable these satellites to transmit and receive signals by electromagnetic radiation and propagation. The scientific community is working hard to develop novel antenna systems to achieve specifications for improved bandwidth (BW) and high data rates. Communications can be to the ground station, large conventional satellites, or other SmallSats. Additionally, antenna designs must take into account any size and weight limitations while also abiding by the CubeSat standard, the challenging operating environment of space, and, the critical need to survive satellite launch. Given these important aspects, non-deployable antenna systems might be the preferred option to ensure reliable satellite operation [1] - [3].

There are many previous examples of these CubeSat antennas. One such design, which is an alternative to more classic deployable systems for low data rate communications is the folded-shorted patch compact array [14] - [18]. Operation has been for Picosatellites, CubeSats, and other SmallSats at UHF and L-band frequencies. An interesting patch design with high gain for the S-band was also achieved by making the four rectangular patches properly excited [19]. Additionally, the dimension of this antenna allows it to fit within the CubeSat standard. A wideband patch antenna which used an aperture coupled stripline-feed was also presented in [20]. This antenna used an elegant technique for integrating the structure into the satellite chassis.

Clever and state-of-the-art methods for solar panel integration when considering non-deployable antennas on CubeSats have also been investigated [21] - [24]. In this way, extra space is made available on the satellite structure for more solar cells, other sensor technologies, and communication devices. This can enhance the battery charging capabilities in that more solar power can be collected. This is important since these approaches do not add much mass to the satellite structure, but at the same time, can increase design complexity. Regardless, having more solar cells on the satellite itself can enhance solar power collection leading to more advanced mission capabilities.

All these SmallSat antenna examples generally offer broadside radiation. This might be impor-

tant for some applications, but depending on the antenna placement on the CubeSat chassis, the broadside beam could be pointing in the wrong direction. For example, radiating away from the Earth when considering downlink transmission; i.e. into empty space with no relevant direction for the propagating signal, or, into the sun. These situations can waste precious power levels within the CubeSat or render faulty system operation, simply, due to the incorrect radiation pattern generated by an inappropriate antenna design which might be better suited for a different mission task or alternative placement on the CubeSat structure.

Endfire antennas, on the other hand, radiate and direct electromagnetic fields into free space and along the direction of the antenna structure itself. These types of antennas might be more appropriate for CubeSats whilst considering physical placement on the satellite. These endfire antennas can also provide a low aerodynamic drag profile when compared to broadside antennas in some practical applications, for instance, in missiles, high-speed aircraft, and radar. As a result of this low profile and radiation along the structure, these antennas typically offer high gain and are employed in many military and commercial applications [25]. Achieving endfire radiation can be done with many techniques. Examples include planar antennas that employ directive surface wave launchers (SWLs) [26]. Also, a metal structure which utilises leaky waves (LWs) has been reported in [27]. The structure of this antenna is similar to a centipede, whilst having many radiating elements. Recent substrate integrated waveguide (SIW) horn antennas [28], which use dielectric-loading at the end of the single-layer horn, are also of interest for achieving endfire radiation.

Figure 2.1 displays various types of CubeSat antennas, categorised into low-gain antennas (LGAs) and high-gain antennas (HGAs). LGAs include patch, dipole, monopole, and helical antennas. HGAs are further divided based on their stowage volume, with smaller volume HGAs including metasurfaces, patch arrays, SIWs, and reflect arrays. Larger volume HGAs comprise inflatable, mesh reflectors, membrane, and reflect-array antennas. Section 2.2 will explore the current state of CubeSat antennas, classifying them as LGAs or HGAs based on their gain. This section will also delve into the challenges encountered in the realm of small satellite antennas. Section 2.3 will provide an overview of the relevant background theories, encompassing SIWs, surface waves (SWs), LWs, and fundamental concepts of the transverse resonance equation (TRE). Finally, Section 2.4 will offer a summary of this chapter.

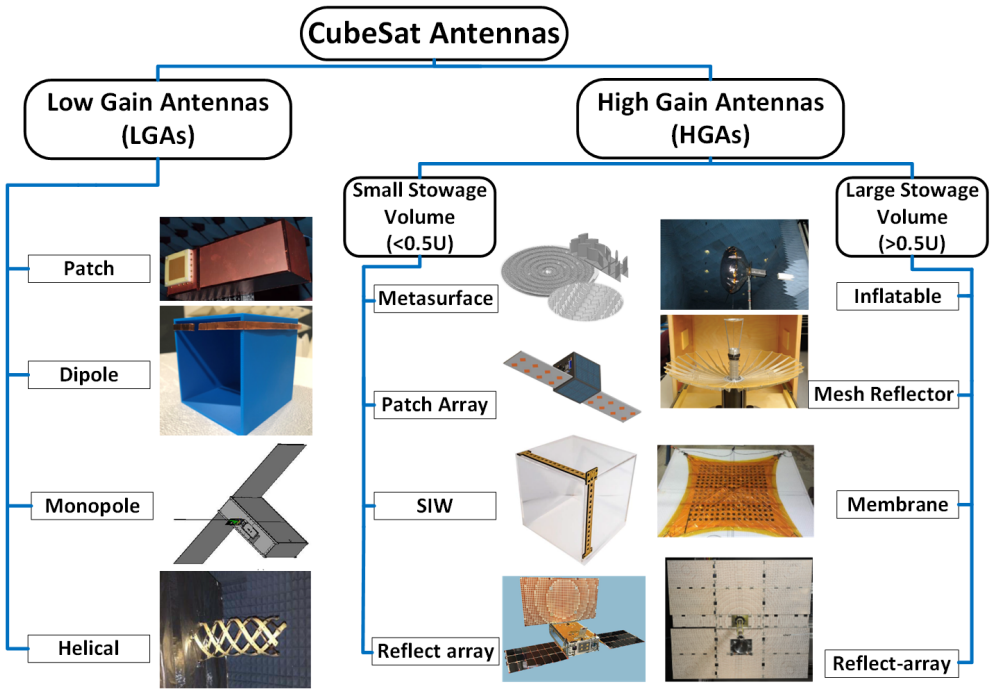

Figure 2.1: *Kinds of antennas for CubeSats that been achieved by the scientific community. LGAs [20, 29, 30, 31] and HGAs [32, 33, 34, 35, 36, 37, 38, 39].*

2.2 State-of-the-art Antenna Review

This section will provide further details on CubeSat antennas with examples. Section 2.2.1 discusses LGAs and their practical applications, while Section 2.2.2 showcases instances of HGAs. Furthermore, Section 2.2.3 outlines the challenges inherent in designing these antennas for CubeSat applications.

2.2.1 Low Gain Antennas

LGAs designed for CubeSats provide a wider signal coverage with modest gain. These antennas are commonly used for CubeSat missions where the primary objective is to provide general coverage and communicate with ground stations over a broader area rather than long-range, high-data-rate communications. Thanks to their broad beamwidth, LGAs allow for telemetry at lower data rates without requiring precise pointing. This feature makes them invaluable for emergency communication during spacecraft anomalies when pointing accuracy may be compromised. Even under uncertain satellite orientations, LGAs ensure essential links [1], [5], [40]. Compared to high-gain alternatives, LGAs are typically simpler in design and can take

the form of a patch, dipole, monopole, or helical antenna.

Patch

Patch antennas are popular for CubeSats due to their low profile and ease of fabrication [1]. The study in reference [41] presents a novel transparent mesh patch antenna designed for 3U CubeSat communication with ground stations. This antenna is notable for its high transparency, allowing it to be placed atop solar cells and enabling surface area reuse. The antenna achieved a total gain of 5.3 dBi at 2.43 GHz. A compact circularly polarised meshed patch antenna designed for small satellites, including 1U CubeSats was introduced in [21]. This antenna is fully integrated with a solar cell and operates at 2.45 GHz (S-band). The authors achieved circular polarisation (CP) and improved both BW and overall antenna gain by exciting the antenna with two orthogonal ports and integrating the feed network under the solar cell. To ensure high transparency and sunlight penetration to the solar cells, the meshed lines of the antenna are placed over a glass layer. Moreover, the proposed antenna demonstrated a gain of 4.8 dBi at 2.45 GHz.

Another example of patch antennas was reported in [42], with an array placed on one face of a 1U CubeSat, designed for intersatellite communications. The face of the CubeSat consisted of nine identical sub-array elements, each comprised of 2×2 individual rectangular patch elements that are fed sequentially in phase. The antenna array operates at 5.8 GHz, achieving a small, measured reflection coefficient of -21 dB, and a simulated total gain of 7 dBi. Shorting walls and pins are also techniques that are used to reduce antenna size without impacting performance. Many CubeSat antennas used this technique to design their antenna, such as the folded-shorted patch compact array which operated at the ultra-high frequency (UHF) range, S-band, and L-band frequencies as presented in [14] - [18], [43]. A high gain F-shaped patch antenna that operated at S-band was introduced in [44], which uses three shorting pins between the radiating patch element and the ground plane. A dual-band CP patch antenna operating at two different frequencies, 1.57 GHz (L-band) and 2.2 GHz (S-band) was also reported [45]. The antenna achieved measured gains of 6 and 5.4 dBi for the S-band and L-band, respectively. Other designs for patch antennas for CubeSats can be found in [22], [46], [47].

Dipole and Monopole

Wire antennas, such as dipole, monopole, and helical antennas, are commonly employed in

CubeSats. These antennas are typically installed on the exterior of the CubeSat chassis, providing room for other electronic components. During transit, these antennas are frequently stored inside the satellite and later deployed once it reaches orbit. They are particularly suitable for applications in the high-frequency (HF), very high frequency (VHF), and UHF ranges [1].

Dipole and monopole antennas are among the most basic and are typically stowed (or made deployable). They are widely known and well-understood. In [48], a single monopole antenna was designed to operate at two different frequencies, 146 MHz (VHF) and 438 MHz (UHF), for transmitting and receiving data simultaneously. This unique feature makes it useful for both uplink and downlink communications, freeing up more space on the CubeSat for other sensors, while reducing interference between the antennas and electronics inside the CubeSat. According to the authors, the antenna has a total gain of 2.06 dBi for VHF and 3.35 dBi for UHF frequencies. An alternative dual-band antenna design, employing the diplexer approach, was described in [49], where a single antenna serves as both the transmitter and receiver. This antenna is also a deployable, functioning in the VHF and UHF frequency ranges and offering gains of 2.6 dBi and 3.9 dBi, respectively.

Printed dipoles have also been adapted in CubeSats in [50] and [51]. Paper [50] discusses a configuration of a 3×1 printed dipole antenna array system suitable for 1U CubeSats. The central concept involves mounting each 3×1 sub-array on distinct surfaces of the CubeSat. This innovative arrangement enhances gain, directivity, and BW, thereby eliminating the need for a deployment mechanism. Additionally, this antenna achieved a total gain of 5.03 dBi. In [51], a novel square-shaped printed dipole antenna tailored for 1U CubeSats was reported. This unique antenna setup incorporates four dipoles intricately with a phase delay line, enabling the generation of CP. Moreover, this printed dipole antenna design delivers a total gain of 3.49 dBi at 2.45 GHz. The primary advantage of this proposed design is its compact size and broad BW.

Helical

Helical antennas consist of conducting wires that are wound in the shape of a helix. The wires may be of the same or different lengths and are typically mounted on a ground plane [52]. These antennas are extensively used in satellite applications because they are affordable, simple to build, and can produce circularly polarised radiation [5]. A modified helical-shaped antenna design for 3U CubeSat, which can be deployed, has been introduced in [53]. The antenna is capable of achieving a unidirectional pattern with a wide BW at UHF. This antenna

achieved a gain of 8.44 dBi, and has a small reflection coefficient of -20 dB at 550 MHz. Recently, quadrifilar helix antennas have been receiving increased attention as a viable design for satellite communication, as indicated in [54] and references therein. For example, a deployable quadrifilar helix antenna, specifically designed for CubeSat applications, was detailed in [55]. This antenna exhibits multi-frequency operation within the UHF range, covering frequencies from 270 to 450 MHz. Across these frequencies, the antenna demonstrated variable gains, with the highest gain recorded at 400 MHz, reaching 5.64 dBi. At 270 MHz, the antenna exhibited a gain of 3.56 dBi, while at 350 MHz and 450 MHz, the gains measured were 4.7 dBi and 5.41 dBi, respectively.

In [31], a new design for a deployable quadrifilar helical antenna for a 6U CubeSat operating in UHF frequency was introduced. The design offers an effective structure that improves packaging and deployment mechanisms, thereby reducing the chances of deployment failure. The antenna achieved a total gain of 8.38 dBi at a frequency of 365 MHz, making it an efficient option for UHF operations. Table 2.1 presents a comparison of all the LGAs based on various parameters, including frequency, size, gain, type of CubeSat, deployability, and polarization. It is evident that conventional dipole and monopole antennas, as well as helical antennas, are designed for the VHF and UHF frequency bands, necessitating deployable features due to their longer wavelengths. In contrast, patch antennas and printed dipole and monopole antennas are tailored for the L, S, and C-bands, with no deployment mechanism except for the antenna in [47]. Section 2.2.2 will examine HGAs that are specifically designed for CubeSats.

2.2.2 High Gain Antennas

HGAs with narrow beam widths play a critical role in the ability of CubeSats to venture into deep space and deliver substantial scientific data for telecommunications and planetary research [40]. In this section, comprehensive details about HGAs for CubeSats will be provided. These antennas can be categorised into two types based on their storage size: small or large. Section 2.2.2.1 will showcase examples of HGAs with small storage volume ($< 0.5U$). Some of these antennas include metasurface, patch array, SIW, and reflect array antennas. On the other hand, Section 2.2.2.2 will introduce examples of HGAs with large storage volumes ($> 0.5U$). Such antennas include inflatable, mesh reflector, membrane, and reflect array antennas.

Antenna Type	Ref.	Oper. Freq. (GHz)	Size ($\lambda_o \times \lambda_o$)	Gain (dBi)	CubeSat Type	Deploy.	Polar.
Patch	**[21]**	2.45 (S-band)	0.19×0.20	4.8	1U	No	CP
	[22]	2.43 (S-band)	0.81×0.81	7.2	1U	No	LP
	[41]	2.43 (S-band)	0.23×0.35	5.3	3U	No	n/a
	[42]	5.80 (C-band)	1.93×1.93	7.0	1U	No	CP
	[43]	1.1 (L-band) 2.4 (S-band)	0.18×0.18	0.0 2.0	1U	No	CP
	[44]	2.45 (S-band)	0.82×0.82	8.5	3U	No	LP
	[45]	1.57 (L-band) 2.20 (S-band)	0.80×0.80	6.0 5.4	3U	No	CP
	[46]	2.45 (S-band)	0.67×1.51	5.4	3U	No	CP
	[47]	2.30 (S-band)	0.46×0.20	4.4	1U	Yes	n/a
Dipole and Monopole	**[48]**	0.146 (VHF) 0.438 (UHF)	0.26 (long)	2.1 3.4	3U	Yes	LP
	[49]	0.144 (VHF) 0.435 (UHF)	1.42 (long)	2.6 3.9	1U	Yes	CP
	[50]	2.50 (S-band)	Printed 0.66×0.66	5.0	1U	No	LP
	[51]	2.45 (S-band)	Printed 0.45×0.45	3.5	1U	No	CP
Helical	**[31]**	0.365 (UHF)	0.12×0.12	8.4	6U	Yes	CP
	[53]	0.550 (UHF)	0.22×0.22	8.4	3U	Yes	CP
	[55]	0.270 (VHF) 0.350 0.400 0.450 (UHF)	0.35×0.35	3.6 4.7 5.6 5.4	3U	Yes	CP

Table 2.1: *Low gain antennas (LGAs) comparisons.*

2.2.2.1 Small Stowage Volume

This section will provide more details on examples of HGAs with small stowage volumes ($< 0.5U$). Multiple design technologies have been explored to create such structures, which can take the form of a metasurface, patch array, SIW, or reflect array.

Metasurface

Metasurface antennas could be a reliable solution for CubeSat HGAs due to their low profile and mass [32], [56]. In paper [32], a novel millimetre-wave high-gain antenna design was presented. This antenna utilises a class of metal-only metasurface and features thousands of subwavelength metallic cylinders with varying elliptical cross sections and heights. These cylinders are arranged in a square lattice on a ground plane, maintaining antenna flatness and lightweight characteristics. The use of an all-metallic structure eliminates concerns related to electrostatic discharge, streamlining qualification testing for space applications [32]. The antenna generates a pencil beam right-handed circular polarisation (RHCP) and with a maximum measured gain of 24.4 dBi at 31.5 GHz. A silicon (Si)–gallium arsenide (GaAs) semiconductor-based holographic metasurface antenna, which operated at 94 GHz, was introduced in [56]. The antenna utilises a holographic technique to shape the radiated beam. This was achieved through modulation of a guided mode generated by a pillbox beamformer. The pillbox beamformer was connected to three integrated horns using SIW technology, all positioned in the focal plane of the pillbox beamformer. This antenna demonstrated a maximum directivity of 31.9 dBi reported at 94 GHz.

Patch Array

Patch arrays represent a straightforward solution for obtaining higher gain in a specific direction when it comes to CubeSat antennas [40]. A high gain X-band patch array antenna for small satellites, including CubeSats, to achieve high aperture efficiency, low sidelobes, and CP radiation in [57], which operated between 7.52 to 8.82 GHz, was reported. The antenna comprised a 4×4 array of CP stacked patch antenna elements. These elements were connected via an unequal tapering using a 1-to-16 power divider network, which enabled the antenna to achieve the desired high gain and low sidelobe characteristics. The final design was compact, measuring 10×10 cm with a low profile. It attained a peak gain of 20 dBi, SLL below -20 dB, and an aperture efficiency ranging from 65.0% to 97.5%. A dual aperture-coupled microstripline-fed

antenna array designed for CP in the C-band was presented in [33]. The primary goal was to create a four-patch antenna array intended for installation on CubeSat deployable wings, alongside a layer of solar panels. This approach aims to optimise available space and enhance the link budget for a standardised 1U CubeSat.

Substrate Integrated Waveguide

SIWs are engineered to minimise mutual coupling between antennas and other components, along with mitigating the impact of unwanted substrate and surface waves [58]. This distinctive transmission line technology enables SIW-based circuit elements to be positioned in close proximity, leading to a reduction in the overall system dimensions. Consequently, SIW can represent an effective solution in small satellite applications [59], [60]. In a recent study, a compact dual slot antenna integrated with a small aperture-coupled SIW cavity was introduced [60]. This prototype antenna demonstrated a gain of 8.4 dBi at 15 GHz. To explore high-gain applications, the study also examined an array configuration consisting of a 2×4 arrangement of these antenna elements, and experimental validation confirmed a gain of 16 dBi. A novel planar leaky wave antenna (LWA) and its array have been introduced for CubeSat communication applications in [34], featuring flexibility in CP and beam scanning. Utilising SIW technology, the proposed LWA is realised by etching periodic fan-shaped slots on the surface of a SIW, covering a broad frequency range from 27.4 to 37.3 GHz. Leveraging the special element design in [34], a conformal high-gain LWA array comprising two vertically arranged units for a 1U CubeSat was achieved, achieving an overall gain of approximately 17 dBi.

Reflect Array

In 1996, John Huang proposed a deployable reflect array made of flat panels that could be combined with solar cells [61], [62]. This concept was first realised with the CubeSat Integrated Solar Array and Reflectarray Antenna (ISARA) technology demonstration [63], which marked the first reflectarray in space. ISARA achieved an impressive 33 dBi gain at 26 GHz for LEO communication. This research was expanded to an X-band communication system employing a reflectarray that was deployed from a 6U CubeSat [35], [63]. This CubeSat was launched with the NASA InSight Mars lander mission. The transmit-only reflectarray exhibited a substantial gain of 29.2 dBi at 8.4 GHz. The selection of the deployable patch array HGA for the Mars cube one (MarCO) mission was primarily motivated by the necessity to store a physically large aperture within the extremely constrained volume of the spacecraft. To stow the antenna, the

Antenna Type	Ref.	Oper. Freq. (GHz)	Size ($\lambda_o \times \lambda_o$)	Gain (dBi)	CubeSat Type	Deploy.	Polar.
Metasur.	**[32]**	31.5 (Ka-band)	5 (Radius)	24.4	n/a	No	CP
	[56]	94.0 (W-band)	15.6×15.6	32.0 Directivity	1U	No	n/a
Patch Array	**[33]**	5.5 (C-band)	4.2×1.9	12.4	1U	Yes	CP
	[57]	8.2 (X-band)	2.7×2.7	20.0	1U	No	CP
SIW	**[34]**	28 (Ka-band)	18.4×0.5	17.0	1U	No	CP
	[60]	15.0 (Ku-band)	2.1×1.5	16.0	1U	No	CP
Reflect Array	**[35]**	8.4 (X-band)	9.4×16.8	29.2	6U	Yes	CP
	[63]	26 (K-band)	29.4×20.7	33.0	3U	Yes	CP

Table 2.2: *High gain antennas (HGAs) with small stowage volume comparisons.*

three flat panels were folded against the CubeSat side, occupying minimal stowage space.

Table 2.2 provides a comparison of all HGAs with small stowage volume antennas, focusing on parameters such as operational frequency, size, maximum gain, polarization, deployability, and CubeSat type. In general, it is observed that metasurface, patch array, and SIW antennas are compatible with 1U CubeSats and do not incorporate deployable techniques, except for the patch array antenna in [33], which is designed with a deployable structure. Reflect array antennas are associated with 3U and 6U CubeSats, both antennas featuring deployable structures. Notably, all antennas listed in this table generate CP.

2.2.2.2 Large Stowage Volume

This section provides additional details about HGAs characterised by substantial stowage volumes. Various design techniques, such as inflatable and mesh reflectors, membranes, and reflect arrays ($> 0.5U$).

Inflatable and Mesh Reflectors

High-gain reflector antennas have gained prominence in the CubeSat field due to their poten-

tial for high gain and fine resolution, particularly for higher orbits and deep space missions. These antennas can achieve gains exceeding 30 dBi across a wide frequency range. However, their mechanical complexity and large profile pose integration challenges within the limited CubeSat volume, necessitating the development of deployment mechanisms for such antenna systems [1], [5], [64]. An innovative solution involves the use of inflatable antennas, which have undergone thorough testing, particularly at S-band [65] and X-band [66], for deep-space communication applications. This antenna design features an inflatable reflector, either conical or cylindrical in shape, with a diameter of 1 m. It is designed to be attached to the end of a 3U CubeSat. While in its folded state, this reflector occupies minimal space on the CubeSat, but upon deployment in space, it transforms into a substantial reflector dish, featuring a patch antenna at the feeding point. The resulting antenna configuration offers impressive performance, delivering a maximum gain of 25 dBi at the S-band [65] and 34 dBi at the X-band [66].

Several innovative deployable mesh reflector solutions have been created for CubeSats, functioning in X-band, or Ka-band frequencies, as illustrated in [37], [67], [68]. A deployable mesh reflector antenna, operating in the Ka-band with a 0.5 m diameter, was developed for use in deep space communication [37] and Earth science missions [67]. Despite its compact design to fit within a restricted 1.5 U volume, the antenna exhibited remarkable performance, achieving a gain of 42.4 dBi with an efficiency of 60% at a frequency of 34 GHz. The design incorporated a mesh reflector equipped with 32 ribs and included components such as a feed horn, four struts, a hyperbolic reflector, and the 0.5 m deployable mesh reflector. In [68], an innovative 1 m deployable mesh reflector, designed for deep space network telecommunications, was introduced. This antenna is suitable for 12U CubeSats and operates in both X-band and Ka-band for uplink and downlink purposes. Prior to deployment, during launch, the antenna is stowed within a 3U CubeSat volume. The mesh reflector boasts an effective diameter of 1 m and a focal length of 0.75 m. Impressively, the antenna achieves high gain in the X-band, with values of 36.1 dBi for the uplink frequency band and 36.8 dBi for the downlink frequency band. Furthermore, in the Ka-band, the antenna delivers remarkable gains of 48.4 dBi for the uplink frequency band and 48.7 dBi for the downlink frequency band.

Membrane

Membrane antennas have been extensively studied by John Huang at the NASA Jet Propulsion Lab (JPL) for small satellites [69], [70]. These antennas are attractive due to their ability to provide a large aperture while occupying minimal stowage volume. These membrane antennas

can take the form of patch arrays [38] or reflectarrays [71] and are a logical choice for CubeSats. The fundamental concept involves constructing the antenna on a flexible, fabric-like material. This design feature enables the antenna to be conveniently folded and stored in a compact space [1]. Nevertheless, its primary limitation lies in the reliance on a sophisticated deployment mechanism, which could potentially result in mission failure if the antenna fails to deploy as intended [5].

A significant 16×16 patch array, intended for remote sensing applications on a 6U CubeSat, offers deployable functionality [38]. This antenna design employs two tensioned membranes that can be neatly folded into a compact 2U payload size. With the aid of four deployable boom structures, it operates at 3.6 GHz (S-band), achieving an impressive gain of 30.5 dBi. An X-band reflectarray membrane antenna is currently in the developmental phase at JPL [71]. This antenna is configured to be accommodated within a 4U CubeSat volume while in stowage but can significantly expand, providing a substantial aperture of 1.5m $\times$ 1.5 m upon deployment. Notably, it demonstrated an impressive gain of 39.6 dBi at 8.4 GHz during measurement using a feed horn located at its focal point.

Reflect Array ($> 0.5U$)

To achieve a narrower beamwidth suitable for remote sensing applications, a deployable reflectarray antenna has been developed for 6U-class CubeSats [39]. Notably, it is the largest Ka-band CubeSat-compatible antenna to date. This Ka-band high-gain reflectarray antenna utilises Cassegrain optics, allowing it to incorporate a deployment mechanism for stowing the reflectarray panels and feed assembly within a confined space. Despite the challenging mechanical constraints imposed by the small wavelengths in the Ka-band, this linearly polarised antenna demonstrated exceptional performance, achieving a remarkable gain of 47.4 dBi at 35.75 GHz [39].

Table 2.3 presents a comparison among HGAs with large stowage, focusing on parameters such as frequency, size, gain, polarization, deployability, and CubeSat type. It is notable that all antennas listed in this table feature deployable structures with significantly high gain. The membrane antennas target lower bands, specifically the S and X-bands, while the reflect array is tailored for the high band, namely the Ka-band. Additionally, reflector antennas, available in two types, inflatable and mesh, are designed for all bands, including S, X, and Ka-bands.

After analysing the information provided in the literature and Tables 2.1, 2.2, and 2.3, it be-

Antenna Type	Ref.	Oper. Freq. (GHz)	Size ($\lambda_o \times \lambda_o$)	Gain (dBi)	CubeSat Type	Deploy.	Polar.
Inflatable and Mesh Reflectors	**[37]**	32.0 (Ka-band)	53.3 (diameter)	42.0	6U	Yes	CP
	[65]	2.4 (S-band)	8.0 (diameter)	25.0	3U	Yes	n/a
	[66]	8.4 (X-band)	28.0 (diameter)	34.0	3U	Yes	n/a
	[67]	34.0 (Ka-band)	56.6 (diameter)	42.4	6U	Yes	n/a
	[68]	7.2 8.4 (X-band) 32.1 34.5 (Ka-band)	23.9 (diameter) 107.0 (diameter)	36.1 36.8 48.7 48.4	12U	Yes	CP
Membrane	**[38]**	3.6 (S-band)	18.4*×8.4	30.5	6U	Yes	LP
	[71]	8.4 (X-band)	42.0×42.0	39.6	4U	Yes	n/a
Reflect Array	**[39]**	35.7 (Ka-band)	109.8×124.9	47.4	6U	Yes	n/a

Table 2.3: *High gain antennas (HGAs) with large stowage volume comparisons.*

comes evident that there is a gap in the availability of high-gain antennas integrated with solar cells for high-frequency and endfire radiation applications. Hence, the motivation behind this research is to integrate the solar panel aperture with the antenna to minimise space requirements on the CubeSat platform. Additionally, the focus is on designing new antennas for such applications with endfire radiation capabilities, where endfire beam patterns can enhance link connectivity. Section 2.2.3 will outline the challenges associated with achieving these objectives, while Section 2.3 will present the relevant background theory for designing these antennas.

2.2.3 Challenges for Small Satellite Antennas

The concept of small satellites typically encompasses both their mass and size characteristics. These satellites are defined by their relatively low mass and compact dimensions compared to traditional larger satellites. Although there is no universally accepted definition, SmallSats generally refer to satellites weighing below 500 kg and exhibiting dimensions ranging from a few centimetres to several meters in length, width, and height. This category includes minisatellites

(100–500 kg), microsatellites (10–100 kg), nanosatellites (1–10 kg), picosatellites (0.1–1 kg), and femtosatellites (<0.1 kg) [1], [2]. The emphasis on mass and size is crucial because these factors significantly influence various aspects of the satellite design, deployment, and operation. Small satellites offer several advantages, including lower costs, quicker development timelines, and the capability to be launched in clusters or constellations. As a result, they facilitate a broad spectrum of applications in space exploration, Earth observation, communications, and scientific research [2], [72], [73].

CubeSats are among the standardised small satellites with defined design and size specifications. The standard outlines a modular design structured around 10 cm cubic units known as "1U". These units are combinable to form larger CubeSat configurations. The dominant CubeSat configurations range from 1U to 12U, representing multiples of the 10 cm cubic unit [2], [72], [73]. Furthermore, the Canadian Space Agency stipulates that the maximum allowable configuration consists of 24U [72].

In general, the design steps for CubeSat antennas, as outlined in the literature and primary CubeSat organisations [72] - [75], are outlined in Figure 2.2. The process begins with identifying the mission requirements, followed by selecting the frequency range. For these initial steps, multiple applications typically need to be submitted to the Space Services Department (SSD) within the International Telecommunication Union (ITU) [76], the organisation responsible for managing this sector. Subsequently, the design phase begins, involving decisions on antenna type, radiation pattern, and integration method with the CubeSat. This is followed by simulation and analysis, fabrication and testing, and environmental testing, culminating in final regulatory approval from the ITU. Finally, the process involves verification, system integration, and satellite launch and operation preparation.

Designing antennas for CubeSats poses a set of distinctive challenges primarily due to the small size of the satellite and power limitations. The confined space within CubeSats restricts the physical dimensions of antennas, limiting their potential gain and directivity. Selecting the appropriate frequency band for communication or scientific objectives is another complex task, considering issues such as interference and adherence to regulatory standards. Overcoming the gain-size trade-off is crucial as CubeSats often require high-gain antennas for effective long-range communications, necessitating innovative compact design approaches. Managing power constraints, ensuring antennas can survive the harsh space environment, and facilitating frequency agility for diverse mission needs also rounds out the tough challenges in CubeSat

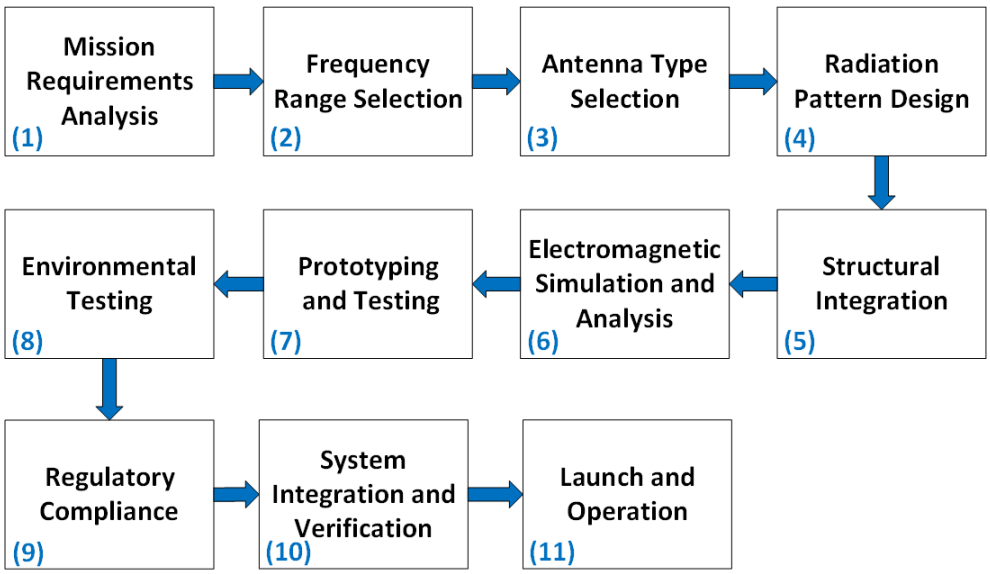

Figure 2.2: *General design steps for CubeSat antennas.*

antenna design [1], [2], [4], [5].

The literature on CubeSat antennas has identified several critical challenges that encompass high gain, operational BW, compact size, low mass, and CP. Each of these challenges plays a pivotal role in enhancing antenna performance. High-gain antennas, for example, enable inter-satellite communications, support deep space missions, and facilitate high-speed data downlink. Wider BW and multiband capabilities enhance mission throughput, allowing a single antenna to operate at multiple frequencies and thereby enabling a broader range of applications, including remote sensing. The emphasis on small size and low mass contributes to cost-effectiveness and mass production while providing additional space for solar panels and reducing the overall weight budget. Additionally, CP offers advantages by eliminating polarisation mismatch losses caused by antenna misalignment, mitigating the effects of Faraday rotation, increasing link reliability, and supporting inter-satellite communications [2], [4], [5], [6]. Next, each of these challenges will be presented and discussed, along with the techniques used in the literature to address and improve these metrics when considering CubeSat antennas.

High Gain

High gains in CubeSat antennas can be achieved through various techniques, namely the cavity technique, SIW, and increasing the aperture size. The cavity technique, as demonstrated in papers such as [20] and [24] for CubeSat antennas, is a popular approach for enhancing antenna

gain [5]. However, a key limitation is the increase in the overall antenna profile and weight.

SIW (which will be intensively explained in the next section), on the other hand, is designed to reduce the size and cost of rectangular waveguides while facilitating integration with planar components [58]. This technique offers the advantage of controlling SWs at high operating frequencies, thereby increasing antenna efficiency. Moreover, papers like [34] and [60] have employed SIW in CubeSat antennas and successfully achieved high gain.

Regarding aperture size, the CubeSat community has adopted various innovative methods to accommodate large apertures within the CubeSat form factor, which can be deployed once the satellite is in orbit [1]. These techniques encompass folding apertures or employing collapsible substrates as seen in reflectarrays [35], [39], [63], membranes [38], [71], and when replacing conventional reflectors with inflatable structures [65], [66], or deploying mesh reflectors [37], [67], [68].

Bandwidth

Expanding BW and achieving multiband capability in CubeSat antennas can be realised through various techniques, including the utilisation of shorting pins, aperture coupling and stacked structures, quadrifilar arrangements, and subwavelength periodicity, as highlighted in [5].

One effective technique to enhance BW and reduce the size of patch antennas involves employing shorting pins and effective metallic walls [5]. These pins, when strategically placed at the edges of the patch, lower the first resonant frequency mode. Additionally, they facilitate antenna miniaturisation by effectively extending the electrical length of the patch antenna (and this reduces the operating frequency) while not increasing its physical size. An example of this technique in practice from the literature is the F-shaped patch antenna [44].

The aperture-coupled and stacked structure presents another approach for widening the BW of microstrip slot antennas. This method isolates the microstrip feedline from the radiating patch element by inserting a ground plane between them. The radiating element resides on the upper substrate, while the feedline is situated on the lower substrate, ensuring no direct connection between them [5]. A practical application of this technique from the literature can be found in [57] which considers X-band antennas.

The quadrifilar helix antenna design is characterised by orthogonal quadrifilars rotated by 90° with respect to each other. This configuration is significant as it imparts CP and extends the BW

of the antenna [5]. Notable instances of antennas employing this method from the literature can be found in references [31] and [55].

In reflectarrays, the subwavelength periodicity technique is frequently employed to increase gain and BW. This approach involves arranging the reflectarray elements or unit cells in a grid pattern with spacing less than half a wavelength [5], [77]. This effectively broadens the BW of the antenna. Examples of CubeSat antennas employing this technique from the literature can be found in references [35] and [63].

Size and Mass

CubeSat antennas can achieve small size and reduced weight through various techniques, including solar panel integration, meandering, mesh grid reflectors, and diplexers with LC loading, as detailed in [5].

The integration of solar panels into antennas, often referred to as transparent antennas, is a popular approach for minimising mass and size while efficiently utilising CubeSat real estate. This design strategy allows CubeSats to share space between the antenna and solar cell subsystems without the need for additional payload volume. Examples of CubeSat antennas adopting this technique can be found in references like [21], [22], [41], and [63].

The meandering technique is another method utilised for patch antennas to achieve miniaturisation without altering the operating frequency of the antenna. Meander line geometries are created by folding and bending conductors back and forth, effectively reducing the the physical size of the antenna. Antennas employing this technique provide broad BWs while occupying minimal surface area. Examples of CubeSat antennas utilising meandering techniques can be found in references like [43], [46], and [47].

In reflector-based CubeSat antennas, meshing reflector apertures have gained popularity. This method approximates the parabolic surface of conventional reflectors with a mesh structure, resulting in weight reduction and deployment mechanisms [67], [68]. Additionally, diplexers are employed to enable each antenna to function as a transceiver, reducing the overall number of antennas required. This allows for transmission and reception at different operating bands. The diplexer and other loading techniques have been applied in CubeSat antennas for VHF and UHF operation, as demonstrated in references such as [48] and [49].

Circular Polarisation

In space communications, challenges like polarisation mismatch and signal attenuation can be effectively mitigated through the use of CP antennas. CP antennas have the advantage of making up/downlink or intersatellite communication robust against antenna misalignment. This is particularly helpful in CubeSat communications with ground stations, where signals traverse the atmosphere and Faraday rotation can distort the signal. The Faraday rotation, also known as the Faraday effect, is the phenomenon where the polarization of electromagnetic waves is altered by a magnetic field as they travel through a medium. This effect results in the rotation of the field maximum for the propagating radio wave. The degree of rotation experienced, is determined by various factors, including the intensity of the magnetic field, the concentration of free electrons within the medium, and the frequency of the radio wave [78]. CP antennas function by exciting two orthogonal modes with a 90-degree phase difference and equal amplitude around the resonant frequency [78] and [79].

Patch antennas for example, can achieve CP through two primary techniques: corner-truncated and sequential-feeding [5]. These techniques find application in single patch antennas, patch antenna arrays, reflectarray feeds, etc. Basically, sequential-phase feeding (with equal amplitude) and corner truncation are the two prominent approaches widely adopted by CubeSat antenna designers. Notable instances of CubeSat antennas employing these techniques from the literature can be found in references like [43] and [57].

In response to these challenges and limitations, the research in this thesis endeavours to propose and design novel antennas tailored for CubeSats and other SmallSats. These new antennas aim to address the gap in CubeSat antenna design by enabling integration with the solar panel aperture while offering high gain and endfire radiation capabilities, particularly at higher frequencies. The upcoming technical chapters will comprehensively present these designs. However, before delving into the design specifics, Section 2.3 will provide an overview of the essential background theories that support the design of these antennas. This will encompass fundamental information on SIW, SWs, and the principles of LWs.

2.3 Relevant Background Theory

In this section, comprehensive information pertaining to the relevant background theory will be provided. Section 2.3.1 will delve into the SIW technology, outlining its fundamental princi-

ples, equations, and comparison with the conventional structure, which is a rectangular waveguide. Subsequently, Section 2.3.2 will offer an overview of Surface Wave Antennas (SWAs), delving into the general guided-wave phenomenon. This section will provide an in-depth exploration of SWs propagation in planar guides, specifically along a grounded dielectric slab (GDS). Additionally, the fundamental principles of the transverse resonance technique (TRT) will be explained, which is a method that will be used for the following technical chapters. Lastly, Section 2.3.3 will present a historical perspective on LWAs, their various types, and a general discussion on a comparison between SWs and LWs.

2.3.1 Substrate Integrated Waveguide Overview

SIW structures are characterised by their width (W_{SIW}), post-separation (P), and diameter (d) as illustrated in Figure 2.3(a). However, one potential drawback of SIW structures is their tendency to produce leakage losses into the substrate due to the practical spacing of the vias (P). These losses can be rendered negligible when the ratio between P and d is sufficiently small ($P/d < 2$) [80]. In this case, a dense wall of vias behaves effectively as a perfect electric conductor (PEC). Alternatively, when the value of P is larger, it can induce power leakage, leading to considerable losses. Under these circumstances, the array of vias effectively functions as a partially reflective screen (PRS) [81]. To elaborate further, a substantial P value can facilitate the conversion of a portion of the propagating wave within the SIW into the TEM parallel-plate waveguide (PPW) modes. This characteristic becomes advantageous when designing efficient planar LWAs in SIW, as shown in studies such as [82], [83], and [84], where precise control over these two parameters is required to achieve antenna leakage and radiation into the far-field.

When designing the SIW guide for standard and non-radiating situations, the subsequent guidelines can be considered to reduce these losses and minimise unwanted radiation within an SIW type of transmission line [85]:

$$d < \frac{\lambda_g}{5} \tag{2.1}$$

$$P \leq 2d \tag{2.2}$$

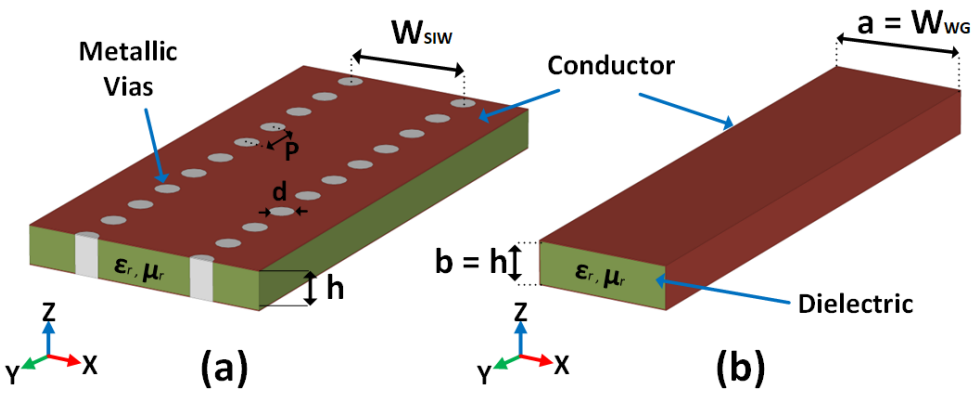

Figure 2.3: *(a) Section of an SIW configuration, and (b) its equivalent dielectric loaded waveguide.*

following Equations 2.1 and 2.2 will ensure that the radiation loss remains at a minimal level, allowing the SIW to be modelled similarly to a conventional rectangular waveguide, where λ_g is the guided wavelength and defined as [58]:

$$\lambda_g = \frac{\lambda_0}{\sqrt{\epsilon_r\left(1 - (\frac{f_c}{f})^2\right)}} \tag{2.3}$$

where λ_0 is the free space wavelength at the operational frequency, ϵ_r is the relative permittivity of the dielectric, f_c is the cutoff frequency, and f is the operation frequency.

When these conditions for non-leaky behaviour are met, the dispersion characteristics of the SIW align with those of rectangular waveguides. Thus, the equations used to determine the width (W_{SIW}) are associated with the equivalent width of a rectangular waveguide (W_{WG}) operating at the same frequency, along with the P/d ratio, as detailed in [80]. While these equations offer a reliable approximation for designing SIW structures, they may lack flexibility when dealing with non-standard P/d relationships. To address this limitation, a viable solution involves conducting a comprehensive full-wave analysis to obtain a precise estimation of the propagation constant across a broad range of P/d values.

The dispersion characteristics of both SIW and rectangular waveguides are similarity, as confirmed by [80]. Consequently, the SIW cutoff frequency and equivalent impedance (Z_e) can be determined by employing the equivalent width of a rectangular waveguide (W_{WG}), as outlined in [58], [80], [86]:

$$f_{c_{TE_{10}}} = \frac{1}{2W_{WG}\sqrt{\mu_0\mu_r\epsilon_0\epsilon_r}} \tag{2.4}$$

$$f_{c_{TE_{20}}} = \frac{2}{2W_{WG}\sqrt{\mu_0\mu_r\epsilon_0\epsilon_r}} \tag{2.5}$$

$$Z_e = \frac{\pi^2}{8}\frac{h}{W_{WG}}\sqrt{\frac{\epsilon_0\epsilon_r}{\mu_0\mu_r}}\frac{1}{\sqrt{1-\left(\frac{\lambda_0}{2}W_{WG}\right)}} \tag{2.6}$$

where h, ϵ_r, and μ_r are thickness, relative permittivity, and relative permeability of the substrate, respectively, ϵ_0, and μ_0 are the permittivity and permeability of free space.

Hence, the SIW width (W_{SIW}) can be determined by [80]:

$$W_{SIW} = W_{WG} - 1.08\frac{d^2}{P} + 0.1\frac{d^2}{W_{WG}} \tag{2.7}$$

These equations will be employed to compute the parameters required for the non-radiating SIW guides for feeding throughout the thesis.

2.3.2 Overview of Surface Waves and Surface wave Antennas

SWAs represent a category of travelling-wave antenna that typically exhibit a beam pattern resembling endfire in the far-field, providing significant gain and vertical polarisation. Their popularity stems from their low profile, lightweight nature, and compatibility with various surfaces, making them applicable across diverse platforms [87]. SWAs can be constructed from metal or via PCB technology and may or may not have a metal backing. In these antennas, SWs are generated and radiated at points of discontinuity, such as corrugations or structural truncations.

SWAs typically have gains that do not surpass 20 dB, as described in Zucker's classic Surface-Wave Antennas Chapter [87], and their ability to control pattern shapes, including sidelobes, is limited. They usually have narrow BWs. These antennas operate across a frequency range from VHF, where Yagi-Uda antennas are commonly used, to microwave and millimeter-wave

frequencies in printed antennas. In contrast, arrays stimulated by SWs can, in theory, generate patterns with exceptionally high gain and precision, comparable to those of nonresonant slot arrays, and offer better control over their characteristics [87].

In order to understand the principles of SWs and its philosophy, firstly, general concepts concerning the guided wave phenomenon and their bounded propagation on planar guiding surfaces are further discussed in Sections 2.3.2.1 and 2.3.2.2. Further insight into the propagation of SWs in GDS regarding key aspects such as wavenumbers, fields excitation, and impedances are provided in Sections 2.3.2.3 and 2.3.2.4. Additionally, the application of the TRT specific to a GDS configuration, is thoroughly explained in these sections.

2.3.2.1 General Guided-Wave Phenomenon

The behaviour of an electromagnetic wave in any medium can be described using its wavenumber and is mathematically expressed by the Helmholtz wave equations [8]. In a rectangular coordinate system, the representation of this wavenumber can be represented as follows:

$$k^2 = k_x^2 + k_y^2 + k_z^2 \tag{2.8}$$

and in general, the wavenumber can be complex for any value of k_i:

$$k_i = \beta_i + j\alpha_i \tag{2.9}$$

where β_i is the phase constant in radians per unit length and α_i is the attenuation in nepers per unit length. These phase and attenuation constants, which represent the wavenumbers, are useful when describing electromagnetic waves in any medium, such a PPW, GDS or for plane-wave propagation.

2.3.2.2 Bound Surface Waves on Planar Guiding Surfaces

An electromagnetic SW follows Equation 2.8 and behaves as a type of guided wave confined within the guiding structure. This implies that the electromagnetic fields are mainly restricted to the guiding surface, propagating away from the excitation source, which is assumed to be

positioned at the origin as illustrated in Figure 2.4. Typically, a SW travels parallel to an interface or guiding surface and exhibits vertical decay from that same interface. This means that the SW phase constant in the vertical direction is zero ($\beta_z = 0$), while it is non-zero along the interface or in the direction of propagation ($\beta_y \neq 0$). As SWs undergo vertical attenuation in the z-direction ($k_z = -\alpha_z$), the SW attenuation constant, α_z, is defined as positive. Consequently, according to Equation 2.8, k_y must be purely real [88]:

$$k_y^2 = \beta_y^2 = k^2 + \alpha_z^2 \ . \tag{2.10}$$

This ensures that there is no attenuation along the direction of propagation (y). Consequently, the field components of a SW in this situation, for propagation in the y-direction, can be described as follows:

$$\vec{E} = yE_y e^{-\alpha_z} e^{-j\beta_y y} \ . \tag{2.11}$$

2.3.2.3 Surface wave Propagation along a Grounded Dielectric Slab

A suitable area for the propagation of SW is the interface between air and a GDS [8], [87], defining a planar guiding surface as depicted in Figure 2.4. The wavenumber in the upward transverse air region (z) is determined by:

$$k(air) = k_0 \tag{2.12}$$

while the wavenumber within the dielectric is associated with the relative permittivity of the substrate, ϵ_r:

$$k(substrate) = \sqrt{\epsilon_r} k_0 \ . \tag{2.13}$$

The field distributions in both regions are matched in phase at the interface, and propagation in the y-direction can be characterised by a real propagation constant. Figure 2.4 depicts a typical profile of the SW field as it propagates along the y-direction, showing evanescent field decay away from the air-dielectric interface at $z = h$ (where h represents the thickness of the

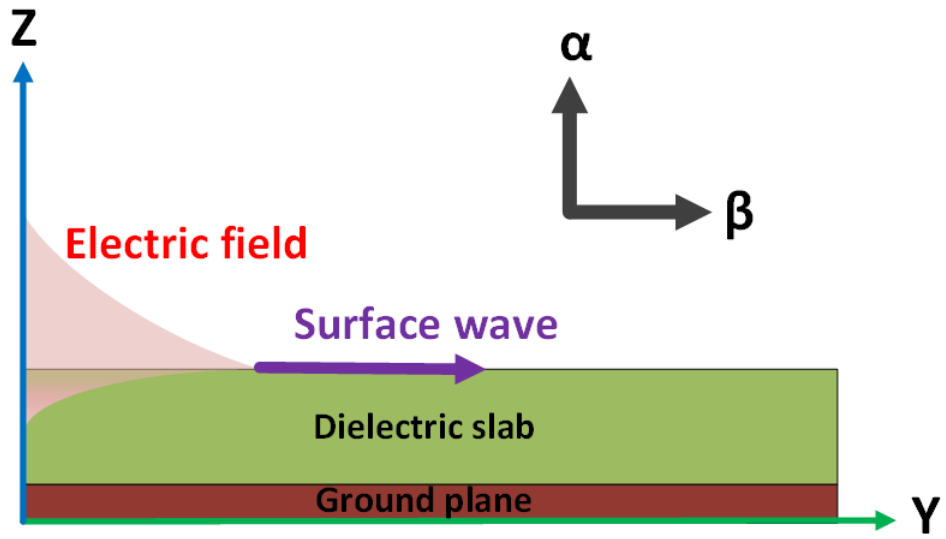

Figure 2.4: *Diagram of SW propagation considering a GDS.*

dielectric slab). Phase propagation along the guiding surface is defined by β_y, and the SW experiences attenuation α_z towards the interface. Accordingly [88]:

$$k_y = \beta_y \tag{2.14}$$

$$k_z = -j\alpha_z \tag{2.15}$$

These explanations assume that these guided SWs are not influenced by changes in the x direction, meaning that k_x is zero and that the propagation primarily occurs in the $+y$ direction and the guide structure is lossless.

SWs are classified as slow waves because their phase velocity is always less than or equal to the velocity of air in the hosting medium; in other words, the phase constant is higher than the propagation constant in free space ($\beta_y > k_0$) [89]. Another significant characteristic of SWs on a GDS is the presence of TM and TE modes above a specific cutoff frequency, as defined in [8]:

$$f_c(TM) = \frac{nc}{2h\sqrt{\epsilon_r - 1}}, n = 0, 1, 2, ..., \tag{2.16}$$

$$f_c(TE) = \frac{(2n-1)c}{4h\sqrt{\epsilon_r - 1}}, n = 0, 1, 2, ..., \tag{2.17}$$

where c is the speed of light. Additionally, regarding these cutoff frequencies, the TM_0 SW mode is the dominant and fundamental mode propagating in the GDS [8]. Its cutoff frequency is 0 Hz, implying that it exists and operates at any frequency; it merely requires a matching system. This mode plays a crucial role in fulfilling the objective of this thesis in designing CubeSat antennas, mainly since it is the dominant mode and can propagate for any frequency. Calculating the TM SW phase propagation constant, denoted as $k_y = \beta_y$ for this specific GDS example, as explained earlier, can be determined using the TRT [8] after knowing h, ϵ_r, and λ_0. Section 2.3.2.4 illustrates this method that will be used next in the following chapters, utilising this specific example, where Section 2.3.2.5 shows the TM_0 SW field distributions for this example as well.

2.3.2.4 Basics of the TRE Approach

The TRT is a general method which can be used to analyse communication systems and help calculate various important quantities, such as wavenumber for complicated waveguiding structures (SWs, LWs, dielectric-loaded waveguides, etc.) and resonance frequencies of resonant cavities. This technique can easily define the propagation constant by solving the transmission line equivalent circuit, which is based on the cutoff condition of the waveguide. The transverse resonance method involves selecting a reference plane and enforcing Kirchhoff's current law (where the entering and leaving currents at a node in a closed circuit are equal) and Kirchhoff's voltage law (where the sum of voltages at a node in a closed circuit is equal to zero), which leads to the TRE (see Equation 2.18). The location of this reference plane is arbitrary; a good selection will typically simplify the derivation of the TRE and the complexity of the final TRE [8]. The first step in setting up the TRE, is assigning the input impedances looking up and down at an interface and defining an equation for calculation:

$$\overleftarrow{Z_{in}} = -\overrightarrow{Z_{in}} \tag{2.18}$$

where $\overleftarrow{Z_{in}}$ is the sum of the input impedances seen looking to the right of the reference plane, and $\overrightarrow{Z_{in}}$ is the sum the input impedances seen looking to the left of the reference plane.

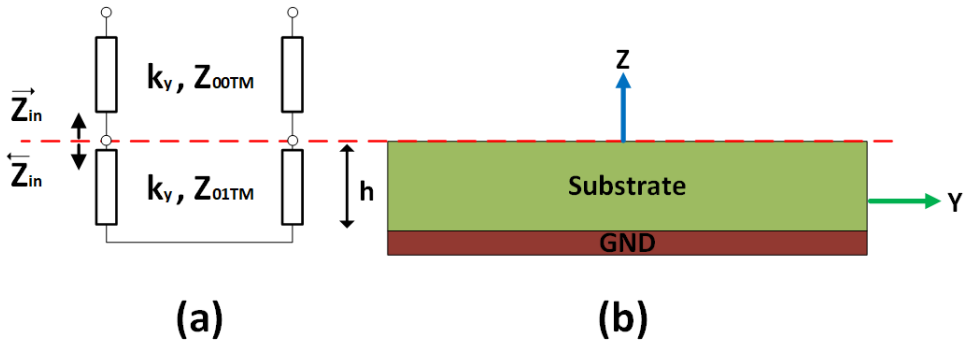

Figure 2.5: *(a) The schematic of the TEN model for the GDS structure, and (b) the equivalent structure for the GDS.*

To illustrate the method, a basic derivation of an equation for the wavenumber of the TM_0 SW mode on GDS using the TRE is outlined. Figure 2.5 illustrates the TEN and the transverse profile structure of the GDS. This derivation assumes that there is no variation of the fields in the x direction, and the propagation is along the y direction. The reference plane is chosen at the interface between the substrate and the air regions. Figure 2.5 considers that the characteristic impedances for the transmission lines with the TEN, in the z direction are as follows [8]:

$$Z_{00TM} = \frac{k_{z0}}{\omega \epsilon_o} \tag{2.19}$$

$$Z_{01TM} = \frac{k_{z1}}{\omega \epsilon_r \epsilon_o} \tag{2.20}$$

where

$$k_{z0} = \sqrt{k_0^2 - k_y^2} = -j\sqrt{k_y^2 - k_0^2} = -jK_{TM_{z0}} \tag{2.21}$$

$$k_{z1} = \sqrt{\epsilon_r k_0^2 - k_y^2} = K_{TM_{z1}} \tag{2.22}$$

and

$$k_0 = \omega\sqrt{\mu_o \epsilon_o} \tag{2.23}$$

where k_y is the phase propagation constant, k_0 is the wavenumber in the free space, ϵ_r is the permittivity in the substrate, ϵ_o is the permittivity in free space, μ_o is the permeability in free

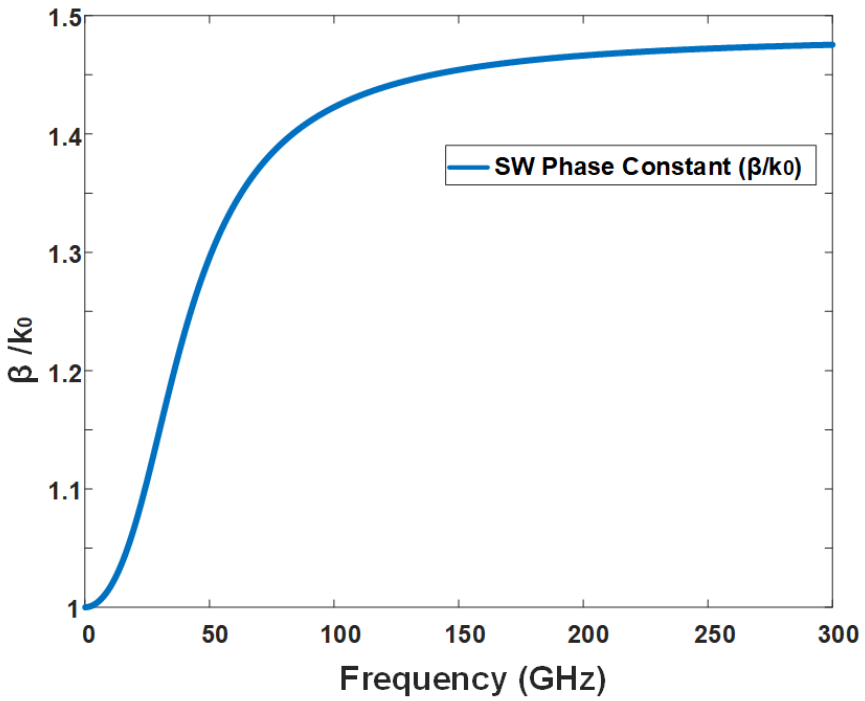

Figure 2.6: *The normalised TM_0 SW mode phase propagation constant for the GDS with $\epsilon_r = 2.2$ and $h = 1.575$ mm for the frequency from 0 to 300 GHz.*

space, $\omega = 2\pi f$ is the angular frequency, $K_{TM_{z0}}$ is defined as $\sqrt{ky^2 - k_0^2}$, and $K_{TM_{z1}} = \sqrt{\epsilon_r k_0^2 - k_y^2}$.

Equation 2.24 shows the derivation after implementing the TRE (Equation 2.18) to this TEN [8]:

$$jZ_{01TM}\tan(hk_{z1}) = -Z_{00TM} \tag{2.24}$$

where h is the thickness of the substrate. The left-hand side of this equation is due to an effective short circuit (or ground plane) positioned at the bottom of the substrate at a distance h from the air-dielectric interface. The right-hand side is the upper input looking into an infinite air space defined by Z_{00TM}. Equation 2.25 presents the derivation after simplifying and expanding Equation 2.24 [8]:

$$\epsilon_r\sqrt{k_y^2 - k_0^2} = \sqrt{\epsilon_r k_0^2 - k_y^2}\tan\left(h\sqrt{\epsilon_r k_0^2 - k_y^2}\right) . \tag{2.25}$$

Figure 2.6 depicts the normalised TM_0 SW mode phase propagation constant for the GDS

after using the Equation 2.25 and numerically solving for the phase propagation constant using Mathematica (see the relevant code in Appendix B). The permittivity for this slab is 2.2 with a thickness of 1.575 mm, for the range of frequencies from 0 Hz to 300 GHz. It can be seen that the maximum normalised phase constant value of this mode is around 1.48, which is equal to $\sqrt{\epsilon_r}$ or the refractive index of the GDS medium for the relevant TM_0 mode.

2.3.2.5 Transverse Magnetic Surface-Wave Field Distributions

The field components that exist for TM SWs on the GDS are the E_y, E_z, and H_x field distributions. By following the expressions in [8] the solutions are as follows:

$$E_y = \begin{cases} A\ sin(K_{TM_{z1}} z)\ e^{-j\beta_y y} & 0 \leq z \leq h \\ A\ sin(K_{TM_{z1}} h)\ e^{-K_{TM_{z0}}(z-h)}\ e^{-j\beta_y y} & h \leq z < \infty \end{cases}$$

$$E_z = \begin{cases} A\ \frac{-j\beta_y}{K_{TM_{z1}}}\ cos(K_{TM_{z1}} z)\ e^{-j\beta_y y} & 0 \leq z \leq h \\ A\ \frac{-j\beta_y}{K_{TM_{z0}}}\ sin(K_{TM_{z1}} h)\ e^{-K_{TM_{z0}}(z-h)}\ e^{-j\beta_y y} & h \leq z < \infty \end{cases} \tag{2.26}$$

$$H_x = \begin{cases} A\ \frac{-j\omega}{K_{TM_{z1}}}\ \epsilon_r\ \epsilon_0\ cos(K_{TM_{z1}} z)\ e^{-j\beta_y y} & 0 \leq z \leq h \\ A\ \frac{-j\omega}{K_{TM_{z0}}}\ \epsilon_0\ sin(K_{TM_{z1}} h)\ e^{-K_{TM_{z0}}(z-h)}\ e^{-j\beta_y y} & h \leq z < \infty \end{cases}$$

where A is the constant relative to the magnitude of the excited SW field distribution, $\beta_y = k_y$ from Equation 2.15, $K_{TM_{z0}} = \sqrt{ky^2 - k_0^2}$ from Equation 2.21 for the TM_0 SW mode on GDS, and $K_{TM_{z1}} = \sqrt{\epsilon_r k_0^2 - k_y^2}$ from Equation 2.22 [8], [88].

2.3.3 Leaky Waves Overview

LWAs employ discontinuities like slots or metallic strips in guiding structures to manipulate travelling waves, generating radiation [90]. The concept traces back to 1940 when a patent described a waveguide with a continuous slot on one side (see Figure 2.7 (a)), causing radiation by allowing energy to leak from the waveguide into free space [91]. This falls into the category

of 1D uniform LWAs, where the introduced perturbation element maintains a consistent geometry along the structure [90]. However, in this setup, there is limited control over leaked energy, leading to broad-beam patterns [91].

A modified approach was presented a decade later, replacing the long slot with closely spaced holes along the waveguide side wall (see Figure 2.7 (b)) [92], [93]. This configuration, is considered quasi-uniform due to the closeness of the holes, and employs the fundamental mode for radiation and still maintains a fast-wave property. This is defined by a phase velocity greater than the speed of light. This development enabled the practical realisation of 1D LWAs, and this type of structure achieved a directive (or narrow-beam) radiation pattern in the far-field [90], [92], [93].

After the initial advancements in antennas with discontinuities, a periodic printed LWA design was introduced in [94]. This structure involved a coplanar transmission line that was periodically modulated using shapes like triangles, sinusoids, and trapezoids. These kinds of structures are described as 1D periodic LWAs (see Figure 2.7 (c)). Moreover, the periodic shapes can be represented by metallic strips or gratings. The key distinction from quasi-uniform structures lies in the fact that periodic LWAs operate based on a slow wave which does not radiate (TM_0 SW mode or TE_{10} waveguide mode), where its phase velocity is lower than the speed of light, supported within the guiding structure [90], [93]. Additionally, the introduction of a periodic array of strips or gratings leads to the excitation of an infinite number of spatial harmonics due to the periodicity. This radiating harmonic (also named the fundamental spatial harmonic) is associated with the dominant bound (or slow) mode of the structure, which is responsible for radiation [95].

Simultaneously with their 1D counterparts, 2D LWAs, inherently planar, were introduced in [96]. These antennas achieved highly directive pencil beams with gains ranging from 15.0 to 20.0 dBi. This was achieved through a planar cavity incorporating a partially reflective screen or surface above the antenna source. This partially reflective screen (PRS) could be composed of either a stack of substrates [97], [98] or a periodic array of slots or metallic gratings [99], [100] (as depicted in Figure 2.7 (d) and (e)). A key characteristic of these 2D systems is their ability to produce either a pencil beam at the broadside or an omnidirectional conical beam, depending on the specific design and feeding technique [90], [93].

1D LWAs have found applications across various technologies in the microwave and millimeter-

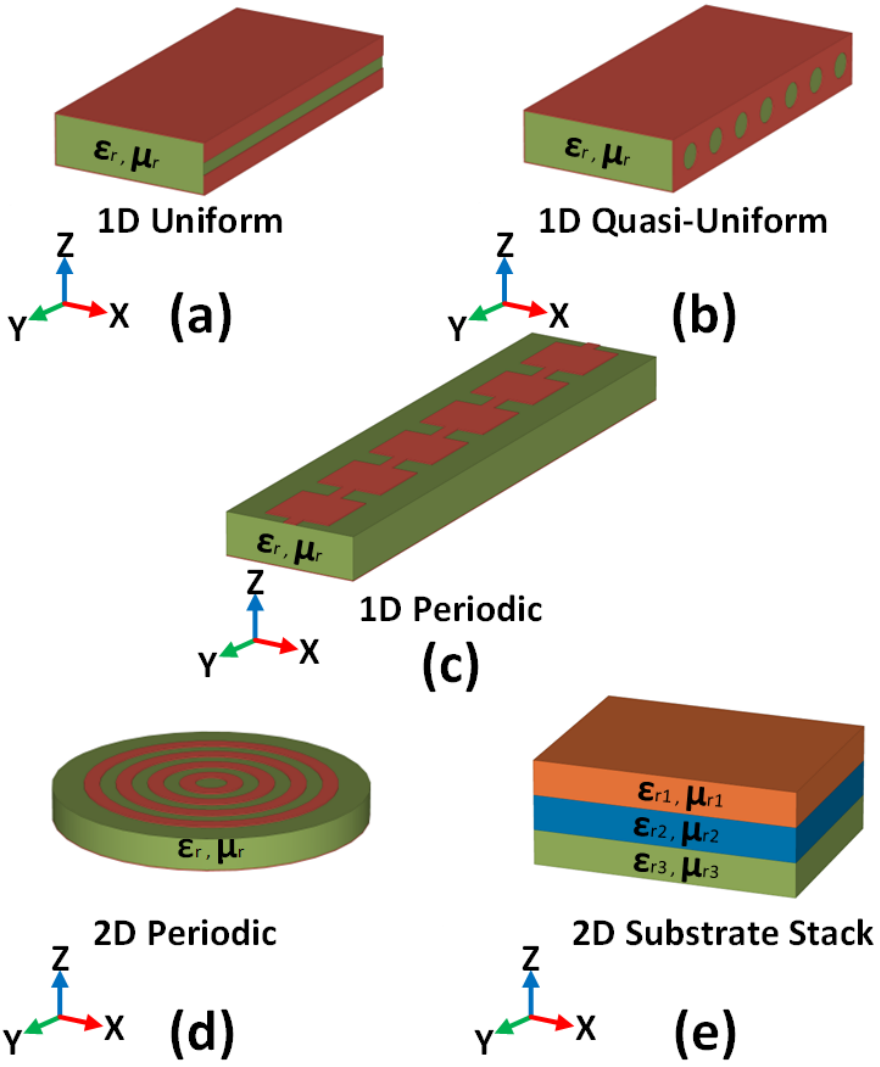

Figure 2.7: *Examples of different types of LWAs.*

wave ranges. Specifically, in many communication systems, dielectric image guides have been employed due to their low losses at higher frequencies. The initial implementation of a LWA using dielectric image guides utilised a corrugated structure [101], where grooves were introduced on the top of the dielectric image guide. This design exhibited excellent performance, serving as a foundation for subsequent high-frequency LWAs. Conversely, the utilisation of periodic strip gratings, instead of modified dielectric slabs, is common for this kind of technology due to the simplicity of manufacturing offered by microstrip technology [102], [103].

However, the realm of 1D LWAs has expanded beyond dielectric image guides with the introduction of SIW technology (as illustrated in Figure 2.8). Many LWAs previously con-

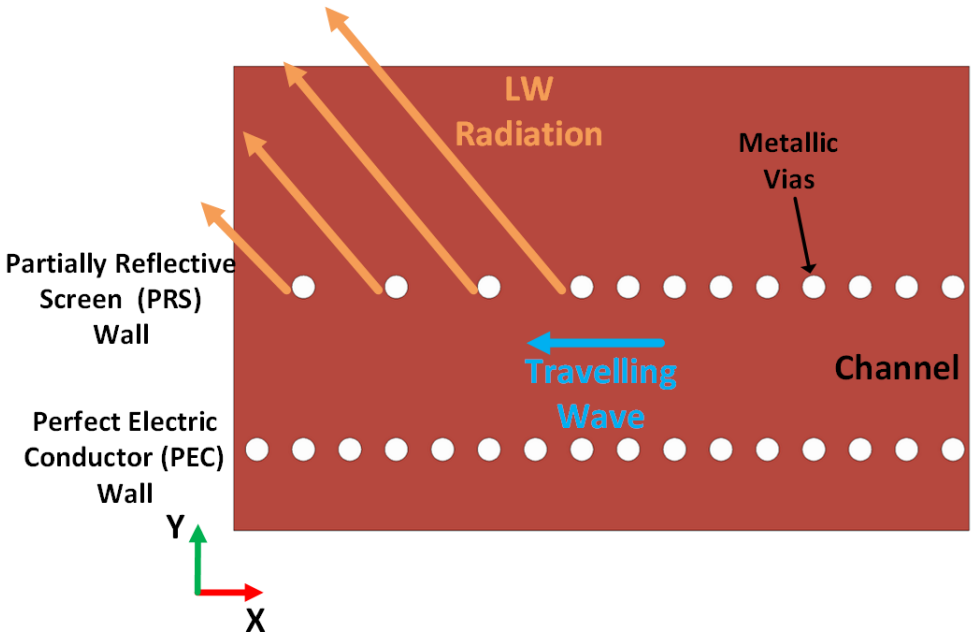

Figure 2.8: *An SIW LWA and its radiation principle.*

structed using conventional waveguides or non-planar structures have been re-designed into planar forms through this SIW technology. This transformation offers notable advantages, such as competitive power handling capabilities and low losses at the relevant frequencies, making it a favourable choice over its non-planar counterparts [80]. Moreover, SIW allows for straightforward feeding mechanisms using microstrip and other planar designs [104].

A simple method to induce LW radiation in these structures involves incorporating a PRS on one side of the SIW guide, while the opposite side serves as a PEC wall, as elaborated in [83], [84], and [105]. Specifically, the dominant mode in SIW is a fast wave, which can be transformed into a leaky mode by the introduction of this PRS. This approach will serve as the technique for creating a leaky SIW T-junction SWL, the upcoming chapter will comprehensively report on this type of structure.

The studies conducted by Oliner and Jackson [93], [106] - [109] significantly advanced our understanding of LW radiation, a phenomenon more complex than its SW counterpart. LWs are characterised as fast waves (with $\beta < k_0$) that continuously leak power while propagating as waves in a guiding medium [93]. For the sake of simplicity and explanations, the author will again consider a lossless GDS, as illustrated in Figure 2.9. The LW travels away from its source, releasing power along the structure, in this situation, through periodic perturbations

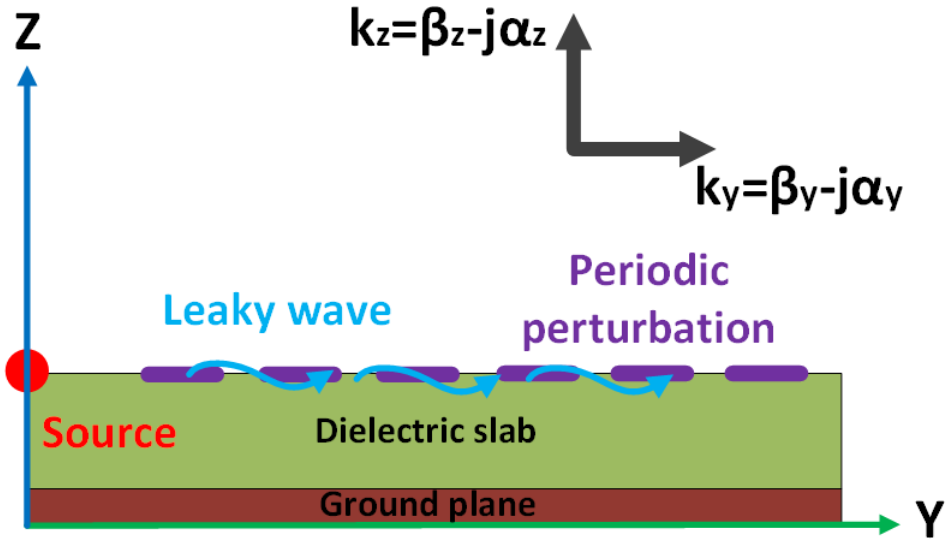

Figure 2.9: *Illustration of LWs considering a GDS, where the bound fields are perturbed by the periodic structure at the air-dielectric interface, causing them to radiate.*

on the GDS. Due to this energy leakage, both the longitudinal and transverse wavenumbers become complex and are described as [90]:

$$k_y = \beta_y - j\alpha_y \tag{2.27}$$

$$k_z = \beta_z - j\alpha_z \tag{2.28}$$

and those two equations can be related by $k_z = \sqrt{k_0^2 - k_y^2}$, where k_0 is the propagation constant for free space as has explained in Section 2.3.2 (Equation 2.23).

2.3.3.1 Leaky Waves and Surface waves

As explained in this chapter, SWs are generally non-radiating and remain bound as they propagate along a GDS. Radiation can occur at specific points of discontinuity or when the structure tapers, such as at the finite edge of a GDS where endfire radiation takes place. In contrast, LWs continuously emit radiation along the antenna aperture as they propagate. Essentially, the amplitude of the LW field decreases as the wave moves along the guiding surface [88].

At this stage, the characteristics of LWs and SWs propagating along a lossless guiding surface have been explained. Bounded SWs are characterised by a real propagation constant, $k_y = \beta_y$ (see Figure 2.4), indicating attenuation in the transverse direction. In contrast, LWs exhibit complex propagation, radiating above the guiding surface in the z-direction $k_z = \beta_z - j\alpha_z$ with field attenuation in the longitudinal y-direction $k_y = \beta_y - j\alpha_y$ (see Figure 2.9). Both types of guided waves, SWs and LWs, can be exploited for different types of feeding and for antenna radiation [88], [90], [93], [110].

2.4 Summary

In this chapter, a comprehensive review of the literature and theoretical foundations have been presented. It can be summarised that significant research has been conducted in the past few decades concerning small satellite antennas, exploring aspects such as increased gains, smaller sizes, and various antenna types. Moreover, the challenges inherent in designing these antennas have been highlighted, including the difficulties in achieving high gain, expanding BW, attaining multiband capability, managing size and mass constraints, and to generate CP.

The theoretical framework essential for comprehending the forthcoming designs, in the upcoming chapters, has also been outlined. Notably, detailed explanations have been provided on the general SIW structure (in this chapter) as well as leaky and surface-wave theories, which are integral to the all the CubeSat antenna systems reported in this thesis. Furthermore, specific theories, such as the guided-wave phenomenon and the behaviour of SWs and LWs on planar guiding surfaces were introduced. Additionally, the TRT was discussed concerning a GDS. These foundations serve as the basis for the designs to be presented in the subsequent chapters. As preferred in this thesis, the use of SIW, LW, SW, and GDS implementations are used to advance the state-of-the-art and bridge the gap in CubeSat antennas. This is achieved in terms of designing clever planar structures which achieve endfire radiation. Moreover, this also involves integrating the solar panel aperture with the antenna to minimise space requirements on the CubeSat platform itself. Furthermore, these non-deployable design approaches are safer and of lower risk, and thus can foster an alternative way to develop new antennas. As shown in the following, these planar antennas can offer high gain and endfire radiation capabilities for operation at microwave and millimeter-wave frequencies.

Chapter 3
Compact Substrate Integrated Waveguide Quasi-EndFire Antenna

3.1 Introduction

In the previous chapter, Chapter 2, the focus was on providing a literature review of small satellite antennas and their challenges. Various examples were listed depending on their gain, whether high or low. Additionally, the last chapter provided an overview of some relevant background theories that this research used, including substrate integrated waveguide (SIW), leaky waves (LWs), surface waves (SWs), and the transverse resonance technique (TRT).

This chapter will present the first major contribution of this thesis by proposing a planar quasi-endfire surface wave antenna (SWA) using SIW technology for integration with CubeSats and other small satellites. A quasi-endfire beam pattern is achieved by the radiation of the fundamental TM_0 SW mode at the edge of a grounded dielectric slab (GDS). This mode is excited by a leaky SIW T-junction, creating a uniform wavefront that propagates through a truncated parallel-plate waveguide (PPW). To reduce reflections and improve antenna radiation performance, a matching section based on an array of subwavelength patches is also added at the interface between the PPW and the GDS.

3.2 An Overview of Previous Works and Challenges with Compact CubeSat Antennas

As a result of the increasing interest for affordable Earth and planetary observation networks, telemetry systems, tracking and control, as well as remote sensing and navigation services, small satellites have seen a rapid growth in the last two decades. Due to this technology trend, and whilst conventional satellite systems cannot be entirely replaced by small satellites, many academic and industrial efforts are focusing on the development of compact and innovative systems. Subsequently, the trend for these small satellites is to offer more communication services

in a generally highly constrained volume when compared to larger satellites. This is especially challenging for antenna engineers as additionally to the RF performance requirements, they also need to consider the inherent CubeSat constraints in terms of volume, weight and cost [1], [2].

Following these trends, there are challenging requirements and antenna specifications in terms of pattern directivity and realised gain (RG), for example, that could restrict design selection when considering said high data rate applications. This has resulted in extensive research into CubeSat antennas which have focused on achieving these important requirements. For instance, the work reported by NASA for remote sensing, which integrated large antennas with a compact stowage box while aiming for high directivity, was based on a meshed deployable reflector antenna system having a stowed volume of 3U [68], [111]. Additionally, in [35], a folded panel reflectarray operating at X-band was stowed in a 6U CubeSat providing a lightweight configuration ($<$1 kg) while keeping high gain values of 29.2 dBi. Planar and nondeployable structures have also been explored when lower gains are required, for instance, as with the folded-shorted patch compact array for telemetry and intersatellite links [14], [15], [18]. These miniaturised patch antennas usually have a resonant length of $\lambda/2$, and can be reduced to a fraction of $\lambda/4$ by a shorting wall and structure folding. These antennas have been designed at UHF and L-band frequencies for small satellites [112] such as the Maritime Monitoring and Messaging Microsatellite (M3MSat) mission for the Canadian Space Agency.

Planar antennas attached to the satellite, as proposed herein (see Figure 3.1), could then be advantageous with respect to deployable systems, due to the degrees of freedom when adopting PCB design and possibly higher reliability in space environments, where debris and strong vibrations or extreme thermal conditions during launching could lead to failed deployments [1], [2], [3]. Moreover, they also allow for innovative integration techniques such as on top of solar cells, as presented in [21], [23], [24]. In this way, extra space is made available on the satellite for additional antennas, sensors, image capturing devices, etc. as well as more solar cells.

Many of these CubeSat antenna examples offer broadside radiation. However, due to the limited space available, chassis placement, and the satellite structure integration requirements, the beam pattern of the antenna may be pointing in the wrong direction. Therefore, it may be necessary to steer the antenna radiation in a different direction such as endfire, being useful for downlink communications for instance. Also, there are not many examples in the literature of

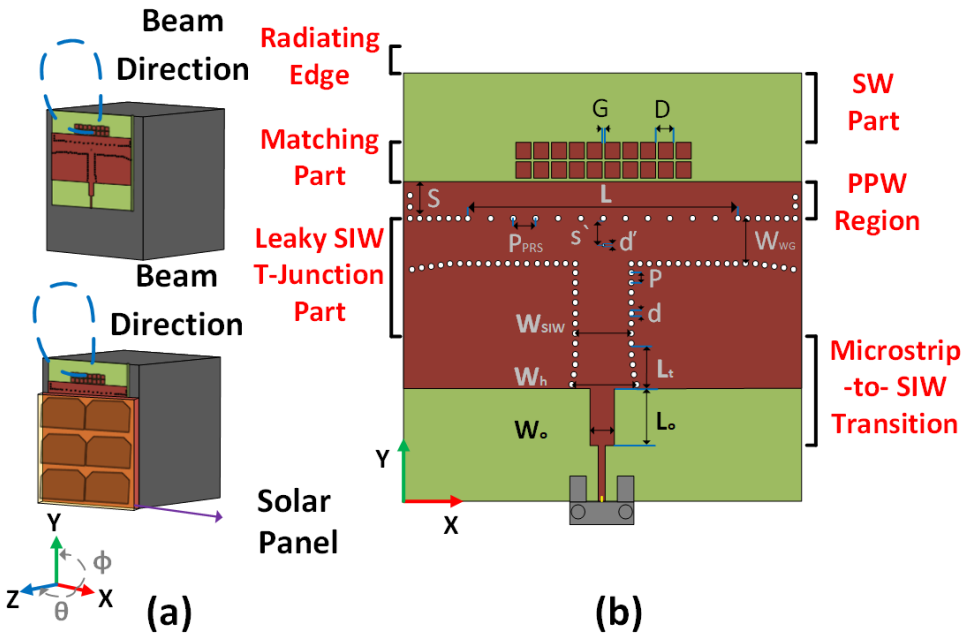

Figure 3.1: *(a) Examples of the placement of the proposed antenna on a 1U CubeSat illustrating the quasi-endfire beam pattern, (b) top-view of the proposed endfire antenna structure defining the design parameters and sections. As illustrated in (a), a solar panel array could also be placed on top of the planar antenna if the microstrip-SIW feedline is removed and the structure is excited by a vertical probe. This is possible because the covered part of the SWA would all be metal [From [110] ©2021 IEEE].*

planar endfire antennas specifically designed for CubeSat applications, and this may be due to integration constraints when aiming to achieve proper endfire or quasi-endfire radiation. More classical implementations, such as Yagi-Uda arrays [113] or complementary dipoles [114], may not be suitable if metallic structures are underneath the radiating element or the space available is highly constrained. These challenges require more clever solutions such as miniaturisation [115] or mechanical steering of the antenna [116].

3.3 Chapter Overview

The researcher proposes herein a compact planar K-band endfire antenna (see Figure 3.1) based on SIW technology [117], [118], LW principles, and TM SWs. The newly studied antenna design employes an adapted version of the PPW launcher (i.e. a nonradiating feed system), as previously reported for a lower frequency band in [82] and [119]. Both of those works focused on the implementation and optimisation of the PPW launcher as a feeding network suitable

for slotted PPW antenna arrays [119], and, a phase control technique to help achieve a uniform and guided wavefront for a nonradiating, two-port demonstrator [82]. The excitation efficiency, which was more than 90% in those previous works, as well as the controlled phase front demonstrated, inspired the modification and adaptation of this feed system to drive a new endfire antenna suitable for downlink applications at K-band on CubeSats and where directive beam patterns are required. The thickness of the substrate was also increased from [82], [119], mainly, to improve and further enhance the SW excitation efficiency for the designed and experimentally measured SWA, providing alternatives to other SW feeding schemes as in [120] and references therein.

Detailed simulations, numerical analysis, and measurements examining the performance of the SWA are reported in this chapter. This proposed planar structure could also be attached to the body of the satellite, achieving a compact and low-profile design. Figure 3.1(a) illustrates examples of the possible CubeSat placement as well as its far-field beam pattern. An explanation on the antenna design is provided in Section 3.4. Discussions on the simulated and measured results will follow in Section 3.5, while Section 3.6 concludes this chapter.

3.4 Antenna Design Approach

The proposed endfire antenna consists of four parts: the microstrip to SIW transition, the leaky SIW T-junction using a PPW, the matching section made by a subwavelength array of patches, and the GDS section for bound SW propagation and then radiation (see Figure 3.1(b)).

3.4.1 Leaky SIW T-Junction

Another name for this antenna part is the open T-junction. The implementation of the conventional T-junction based on SIW technology is the first step in the design process [117], [118]. The primary function of this T-junction is to divide the power over the aperture equally, as shown in Figure 3.2. It should be mentioned that adding an extra inductive post in the middle of this junction will improve the matching [121]. This inductive via has been optimised with a diameter of $d' = 0.21$ mm and a position $S' = 3.07$ mm (see Figure 3.1 (b)).

The SIW TE_{10} fundamental mode is coupled into the transverse electromagnetic (TEM) mode of the PPW section. This is made possible since the broad arms of the T-junction walls are

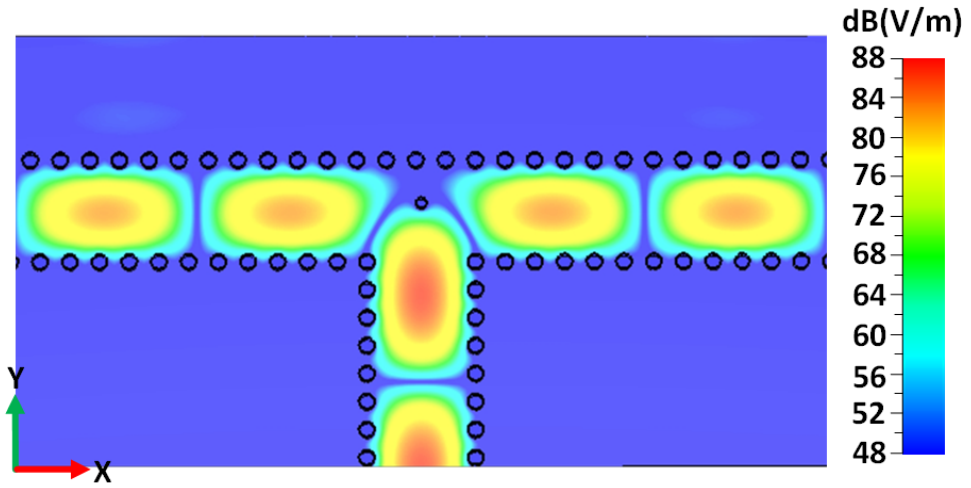

Figure 3.2: *The simulated electric-field distribution inside the conventional SIW T-junction; i.e. in the middle of the slab.*

made lossy to leak out power [82], [122]. Thus, vias are required to be separated more than the regular condition for guided and confined propagation within the SIW ($P \leq 2d$, where P and d are the via periodicity and diameter, respectively [80], [117]). This creates a partially reflective screen (PRS) to allow leakage from the SIW structure to the PPW, which can be designed following the general guidelines in [82] and [83]. The complex propagation constant for the relevant LW mode needs to be analysed to design this PRS. The phase constant β determines the propagation direction for the TEM mode in this PPW region (β is the real part of the complex propagation constant for this mode, see Equation 2.9, [82], [83]). Simultaneously, the leakage rate α controls the coupled power into the PPW TEM mode (α is the imaginary part of the complex propagation constant for this mode, see Equation 2.9, [82], [83]). Moreover, α depends on the spacing between the vias, and the higher this spacing the shorter this PRS length L needs to be [82], [123]. Furthermore, α needs to be high enough for suitable leakage; i.e. such that most of the power from the input feed point is coupled into the PPW section, and not reaching the two side arm ends of the SIW T-junction.

To achieve uniform phase propagation inside the PPW region and the matching section (see Figure 3.3), the operating frequency must be slightly above the cutoff frequency of the SIW, which in this case has been selected to be 18 GHz, and, at the splitting condition where $\beta \approx \alpha$ [122]. The frequency selection of 18 GHz has been chosen to align with operational bands used in previous CubeSat missions [124], [125], for downlink communication with ground stations. The PRS aperture length L can then be found by setting the aperture efficiency to 90%,

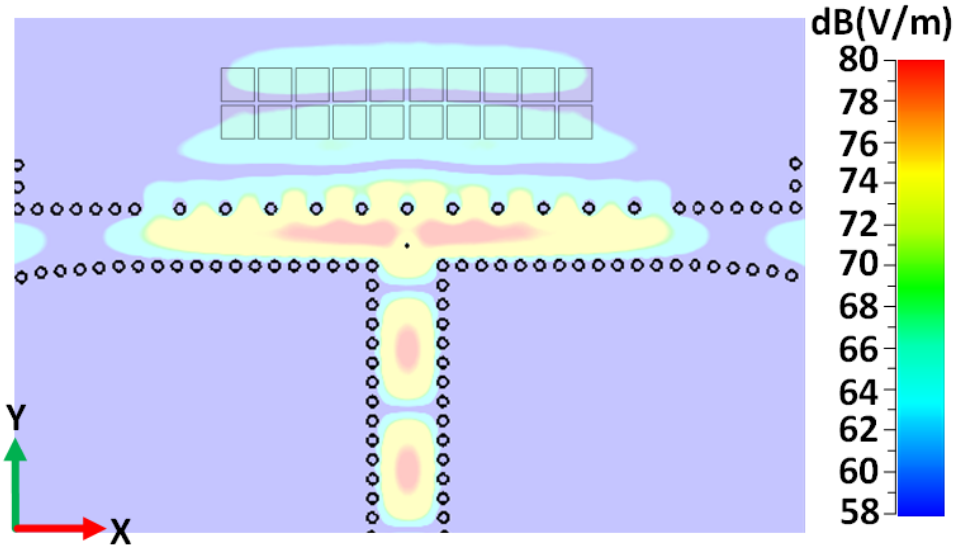

Figure 3.3: *Simulated electric field showing a uniform distribution within the PPW, the SMS, and the GDS [From [110] ©2021 IEEE].*

requiring $L = 2.3/\alpha$ [122]. The dispersive analysis depending on the antenna parameters, can then be performed by a transverse equivalent network (TEN) [8], which is based on an equivalent transmission line circuit of the structure to define the impedance TRE (basics have been explained in Section 2.3.2.4) related to the complex propagation constant. The adopted TEN circuit is the same as in [82] and is depicted in Figure 3.4, where the final dispersive analysis results are also included. It can be observed that the splitting condition occurs in the proximity of 18 GHz.

This analysis of leaky mode dispersion is necessary to adjust the values of W_{WG} and P_{PRS} (see Figure 3.1(b)) that determine the dimensions of the leaky SIW, providing the desired beam-splitting conditions ($\beta \approx \alpha$). In order to easily identify the correct mode or solution using a theoretical approach, it is important to note that mathematically, the TRE for this structure has numerous solutions, with the wanted TEM mode in the PPW region being one of them. To accurately determine the dispersion analysis, the researcher recommends using a quick simulation approach with the Bloch analysis technique [126], which utilises CST results to generate α and β values. Section 3.4.1.1 provides a comprehensive explanation of the Bloch analysis for this particular structure, and then one solution for any frequency will be taken as the first root to be used in the theoretical approach. This will help to easily identify the mode and solution for this structure and tune all the necessary parameters accordingly. Section 3.4.1.2 will present

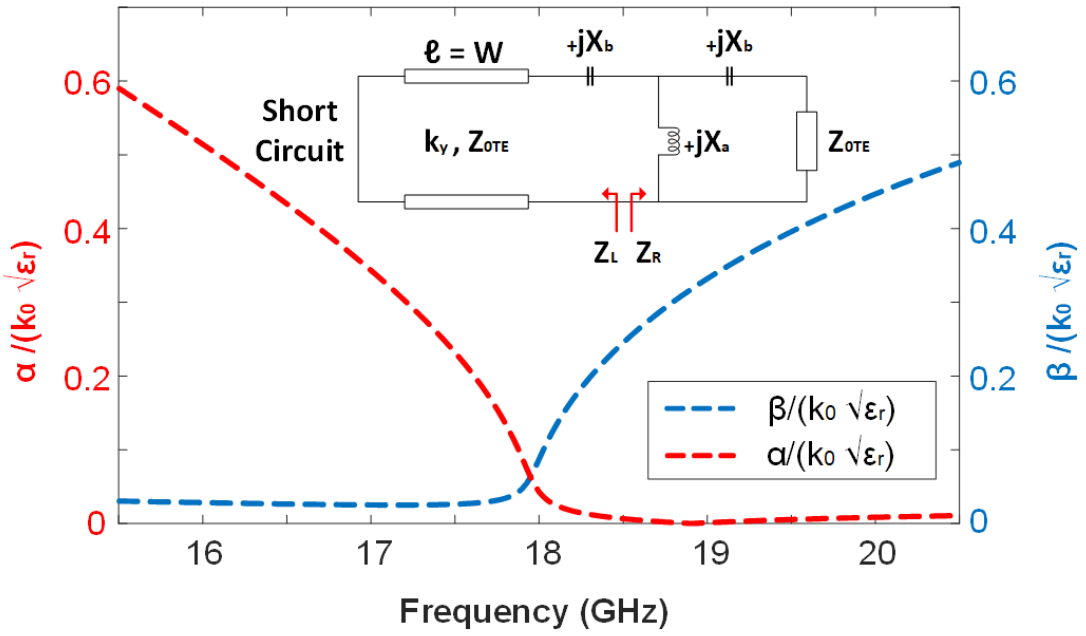

Figure 3.4: *TEN circuit model and the normalised LW phase and attenuation constants. The splitting-condition; i.e., $\alpha \approx \beta$ can be observed at ≈18 GHz [From [110] ©2021 IEEE].*

the tuned parameters for the leaky SIW T-junction.

3.4.1.1 Bloch Analysis

The Bloch analysis, which utilises CST results for its calculation in this thesis, is another method used for generating the dispersive response of the T-junction [126]. Simulations were conducted on multiple unit cells, referred to as N, that consist of a straight SIW section. One side of the section is a PEC wall while the other is a leaky PRS wall. In each unit cell, there are two vias from the PEC wall and one via from the PRS wall, as shown in Figure 3.5 (a). Based on [127], the S-parameters for this structure are used to calculate the transfer matrix (T-matrix), wherein the propagation constant is defined following the equation found in [8]:

$$\cosh \gamma d = (A + D)/2 \tag{3.1}$$

where γ is the complex propagation constant ($\gamma = \alpha + j\beta = jk$), and A and D are the elements from the T-matrix. This matrix will be described in full in the upcoming discussions.

In order to determine the complex propagation constant γ, it is necessary to conduct simula-

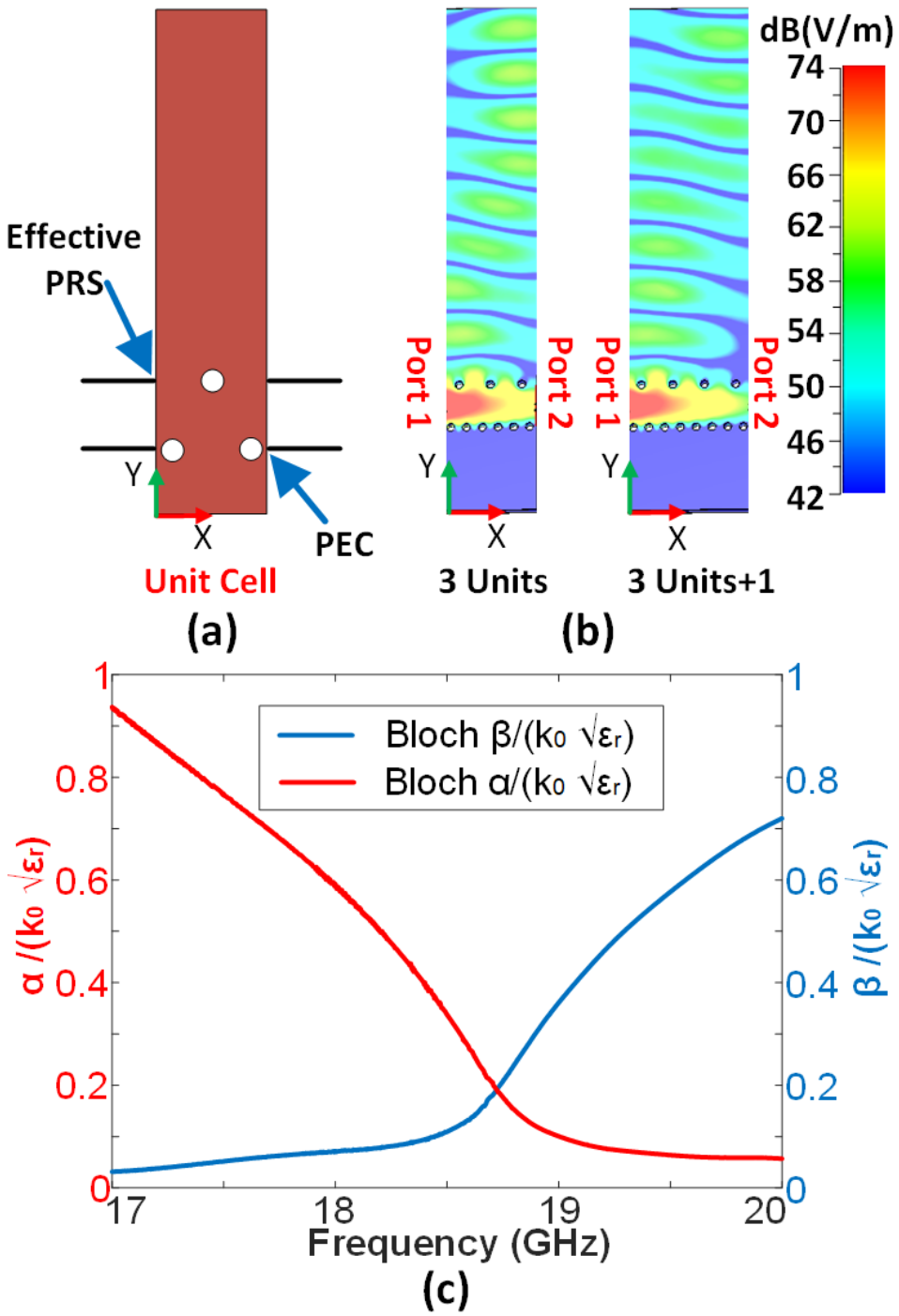

Figure 3.5: *(a) Diagram showing the unit cell consisting of one via which forms the PRS while two vias form the PEC, (b) simulated electric field for 3 and 4 unit cells where it can be noticed that the field has leaked into the PPW region, and (c) results of the normalised LW phase and attenuation constants using Bloch analysis and numerically determined using Matlab.*

tions on the CST system with N and $N+1$ unit cells. This will allow for determination of the T-matrix by analysing the S-parameters at the individual ports. In particular, by utilising Equations 3.2, 3.3, 3.4, and 3.5 [8]:

$$A = \frac{(1+S_{11})(1-S_{22})+S_{12}S_{21}}{2S_{21}} \tag{3.2}$$

$$B = Z_0\frac{(1+S_{11})(1+S_{22})-S_{12}S_{21}}{2S_{21}} \tag{3.3}$$

$$C = \frac{1}{Z_0}\frac{(1-S_{11})(1-S_{22})-S_{12}S_{21}}{2S_{21}} \tag{3.4}$$

$$D = \frac{(1-S_{11})(1+S_{22})+S_{12}S_{21}}{2S_{21}} \tag{3.5}$$

where Z_0 is the characteristic impedance ($Z_0 = 50\Omega$). The T-matrix for the two systems can then be defined as Equations 3.6 and 3.7:

$$T_N = \begin{pmatrix} A_N & B_N \\ C_N & D_N \end{pmatrix} \tag{3.6}$$

$$T_{N+1} = \begin{pmatrix} A_{N+1} & B_{N+1} \\ C_{N+1} & D_{N+1} \end{pmatrix} \tag{3.7}$$

According to the equation presented in [127], the division of the two matrices can be performed as follows:

$$T = \frac{T_{N+1}}{T_N} = \begin{pmatrix} A & B \\ C & D \end{pmatrix} \tag{3.8}$$

γ can now be determined using Equation 3.1. Figure 3.5 provides a detailed diagram of the unit cell developed for this analysis. Additionally, this figure illustrates the electric field for the two unit cell lengths (see Figure 3.5(b)). One design consists of three unit cells (representing the

N structure in the Bloch method), while the other comprises four unit cells (representing the $N + 1$ structure). Using the S-parameters for these two proposed structures, and following the equations mentioned earlier, Figure 3.5(c) presents the normalised α and β obtained through the above described Bloch analysis procedure.

It can be noticed from Figure 3.5(c) that $\beta \approx \alpha$ at around 18.8 GHz; and this is consistent with the centre frequency of the structure [110]. As described earlier, the Bloch analysis is a useful tool to identify the frequency response for β and α, and this is a useful method to support the findings for the TRE of the TEN. Basically, this makes it easier to generate α and β using the TRE with knowledge of the Bloch analysis findings. For the Bloch analysis, the following dimensions were utilised: the diameter of the vias for the SIW section was 1 mm (d), the separation between the vias in the PEC wall and PRS wall was 2 mm (P) and 4 mm (P_{PRS}) respectively. The width between these two walls was 6.6 mm, which is the initial width used in a conventional T-junction structure for 18 GHz using the SIW equation (Equation 2.7).

These dimensions were chosen to satisfy the conditions for bound and leaky propagation within SIW (Equations 2.1 and 2.2) and also to address the limitations of Bloch analysis. The choice of a 2 mm and 4 mm separation was made to facilitate the easy identification of the unit cell. It is worth noting that one of the drawbacks of employing Bloch analysis for SIW lies in the requirement for precise structural details. Section 3.4.1.2 will present the optimised parameters for the leaky SIW T-junction after conducting dispersive analysis and fine-tuning all the necessary parameters accordingly using the TRE and with optimisations completed by CST.

3.4.1.2 Optimised Structure Parameters

Following these preliminary numerical calculations and utilising the TRT to derive the LW phase and attenuation constant represents the initial step in tuning the values of W_{WG} and P_{PRS} (see Figure 3.1(b)) to determine the leaky SIW dimensions that achieve the desired beam splitting condition ($\beta \approx \alpha$) at the designated frequency (18 GHz). Figure 3.6 illustrates a parametric study generated using the TRT to fine-tune the key values for these two parameters. It can be observed that the leakage rate can be controlled by adjusting W_{WG} and P_{PRS}. As inferred from SIW theory, higher cutoff frequencies are attained with smaller values of W_{WG}. Conversely, the leakage rate is influenced by P_{PRS}.

After determining the values for those two parameters and by using the optimisation scheme

using CST Microwave Studio, all structure parameters were optimised. The optimised final values for this leaky T-Junction are: $W_{SIW} = 6.99\,\text{mm}$, $d = 1\,\text{mm}$, $P = 1.93\,\text{mm}$, $W_{WG} = 5.67\,\text{mm}$, $P_{PRS} = 4.5\,\text{mm}$, and $L = 54\,\text{mm}$. Figure 3.1(b) displays these parameters and their position within the designed structure considering Rogers RT5880 as the employed substrate with a relative permittivity of ϵ_r = 2.2 and a thickness of 1.575 mm. This Rogers material is suitable for use in high-reliability, aerospace and defence applications, as outlined on their website [128].

3.4.2 Matching Section and GDS

The distance to the truncation of the PPW region is defined as $S = 5.33\,\text{mm}$ (see Figure 3.1 (b)), this is because it is required to be set as a multiple of $\lambda_g/4$, being λ_g the guided wavelength. This can reduce any reflected power from the leaky T-Junction, and by following conventional $\lambda_g/4$ transformer concepts to control impedances [8]. The same applies to the matching section, defined by subwavelength patches, which is essential to prevent an abrupt transition from the TEM mode inside the PPW to the TM_0 SW mode of the GDS.

The number of these patches also helps to control the leaked power from the T-junction allowing for a smooth transition (see Figure 3.3). During the simulations and optimisations in CST, it was found that the number of subwavelength patches for this SWA should be 10 for every row. The objective is to assess the trade-off between SLL and antenna performance to identify the optimal structure. The parametric study presented in Table 3.1 illustrates the simulated gain and SLL for the yz and xy planes across different numbers of patches per row, ranging from 9 to 21 at 18 GHz. This table illustrates the increase in SLL in the xy plane before and after the design with 10 patches. Moreover, this table highlights that the optimal results are achieved for the SWA structure when 10 patches are used.

The subwavelength square patches are an array of metallic microstrip segments printed on the top of the substrate. This matching section has two parameters, D, the distance between patches, and G, the gap between them (see Figure 3.1(b)). The surface grid impedance Z_g is related to G and allows the fields within the matching section to be controlled and well-matched to the TM_0 SW mode of the GDS [129], [130]. The reason why this is classified as a subwavelength array is because the distance D is more than four times smaller than the free-space wavelength [130]. These parameters can be determined by using the following equations [129] and [130]:

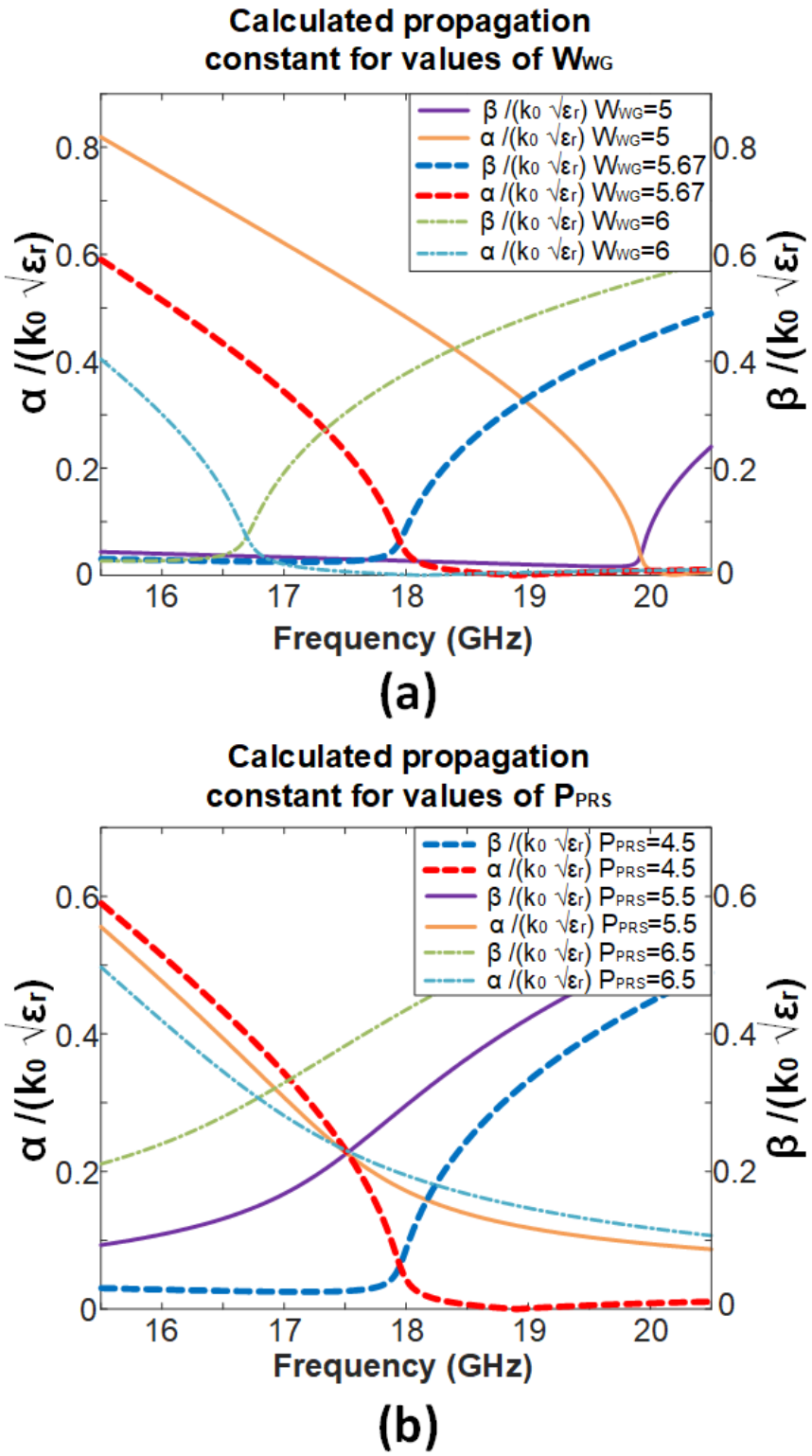

Figure 3.6: *Normalised LW phase and attenuation constants analysis for different values of (a)* W_{WG}*, and (b)* P_{PRS} .

Number of Patches Per Row	yz plane ($\phi = 90°$)		xy plane ($\theta = 90°$)	
	Gain (dBi)	**SLL (dB)**	**Gain (dBi)**	**SLL (dB)**
09	13.7	-12.1	9.14	-11.0
10	13.9	-14.8	9.21	-11.4
11	13.9	-15.7	9.06	-10.7
12	13.9	-15.7	9.06	-10.2
13	13.9	-15.1	9.10	-10.0
14	13.9	-14.9	9.11	-10.1
15	14.0	-15.0	9.14	-10.0
16	13.9	-14.6	9.15	-10.1
17	13.9	-15.1	9.11	-10.0
18	13.9	-15.5	9.08	-9.9
19	13.9	-15.5	9.10	-9.9
20	14.0	-14.3	9.17	-10.1
21	14.0	-13.8	9.15	-10.0

Table 3.1: *Gain and SLL for the designed SWA with different numbers of patches per row (see Figure 3.1(b)) in the yz plane ($\phi = 90°$) and the xy plane ($\theta = 90°$) at 18 GHz.*

$$Z_g = -j\frac{\eta_{eff}}{2\gamma} \tag{3.9}$$

$$\eta_{eff} = \sqrt{\frac{\mu_0}{\epsilon_0 \epsilon_{eff}}} \tag{3.10}$$

$$\gamma = \frac{k_1 D}{\pi} \ln \frac{1}{\sin\left(\frac{\pi G}{2D}\right)} \tag{3.11}$$

$$\epsilon_{eff} = \frac{\epsilon_r + 1}{2} \tag{3.12}$$

$$k_1 = k_0\sqrt{\epsilon_r} \tag{3.13}$$

where Z_g is the surface grid impedance, the wavenumber in the free space $k_0 = \omega\sqrt{\mu_o \epsilon_o}$, ϵ_r is the permittivity in the substrate, ϵ_o is the permittivity in free space, μ_o is the permeability in free space, and $\omega = 2\pi f$ is the angular frequency.

After following the equations above and full-wave simulations, the microstrip patch size was set to $D = 3.485$ mm with $G = 0.355$ mm. Also, as it is well known for travelling wave antennas [87], reflections need to be minimised to prevent unwanted backward radiation, therefore matching techniques, such as the $\lambda_g/4$ PPW section and the subwavelength array of patches, are needed to improve the front-to-back ratio. This is examined in Figure 3.7 where it can be observed that the backward radiation is considerably higher, by more than 12 dB, when the patches are removed. This is also the case for the GDS section (see Figure 3.1 (b)), as it is important to optimise its length and to prevent reflections back from the truncated edge of the dielectric.

At this point within the feed structure and after the sub-wavelength matching section (SMS), the phase propagation constant is already demonstrating slow-wave behaviour, and therefore, the TM_0 SW within the GDS section can be radiated at structure discontinuities. This achieves endfire radiation defining the SWA, and this distance was optimised after a parametric study using CST Microwave Studio to be 8 mm. It should also be mentioned that this SWA was designed in the presence of a ground plane, and when attached to the CubeSat body, the far-field beam pattern can deviate from full-endfire towards quasi-endfire. However, the structure can also be modified and optimised to remove the ground plane of the GDS making it a full endfire SWA, which is useful for other applications and need not to be placed on a metallic surface.

3.4.3 Microstrip to SIW Transition

The tapered microstrip line [104] is widely used for the microstrip-to-SIW transitions as it enhances the matching from the 50-Ω microstrip line to the SIW input [104], [131], [132]. However, there are cases in which the impedance of the SIW section is higher than the one in the microstrip line, and therefore, conventional microstrip tapering cannot be implemented. This occurs in our structure and this is solved by tapering the SIW instead [132]. The reason for this is that the field distribution in the microstrip line is wider than the one in the SIW. Even an optimised design of the traditional microstrip tapered transition cannot achieve good field coupling, as described in [132]. As has been described earlier in Section 2.3.1, the equivalent impedance (Z_e) of SIW can be determined by employing the equivalent width of a rectangular waveguide (W_{WG}). Moreover, the impedance of the SIW is defined by [133]:

$$Z_{SIW} = Z_e = \frac{2h}{W_{WG}} \frac{\eta_0}{\sqrt{\epsilon_r}} \frac{1}{\sqrt{1 - (\frac{f_c}{f})^2}} \tag{3.14}$$

where h is the dielectric substrate thickness, η_0 is the intrinsic impedance of the free space, f_c is the cutoff frequency, and f is the operation frequency. By varying the width W_h (see Figure 3.1), the impedance of the SIW would decrease, leading to a significant improvement in matching. As is typical in the design of matching networks, the length of this taper should be configured as a multiple of $\lambda_g/4$ for best matching. The specific values for the width W_0 and length L_0 of the microstrip line are determined based on the desired frequency and impedance, as outlined in reference [8].

After determining the maximum width of W_h for the desired impedance, the spacing between the subsequent vias must be established. Positioning the vias for this transition should follow an exponential distribution as explained in [132]:

$$y = 0.01 \frac{W_{SIW}}{2} e^{bx} + 0.99 \frac{W_{SIW}}{2} \tag{3.15}$$

$$b = \frac{\ln\Big(100 \frac{W_h}{W_{SIW}} - 99\Big)}{L_t} \tag{3.16}$$

where y is half of the separation between vias at both sides, x is the longitudinal coordinate relative to the first via with a separation equal to it W_{SIW}, and L_t is the length of the transition. Taking into account all the equations and explanations provided above, the parameters for this section have been optimised using the optimisation scheme in CST Microwave Studio as follows: $W_h = 9\,\text{mm}$, $L_t = 8.85\,\text{mm}$, $W_o = 4.85\,\text{mm}$, and $L_o = 12.2\,\text{mm}$.

3.4.4 Excited Fields and Modes

To gain a deeper understanding of the field excitation in this structure, it is crucial to analyse it comprehensively, encompassing all components from the port to the radiation edge (as depicted in Figure 3.1). The dominant mode of the microstrip transmission line is quasi-TEM. In this configuration, while the electric field is primarily confined within the dielectric, it also extends slightly above the dielectric into the free space region, hence the term quasi-TEM in that the

fields are not consistent in both regions, which is different to propagation within a coaxial cable, for example. For this microstrip dominant mode, the electric fields stretch between the two conductors (the ground and the top plate of the microstrip line), while the magnetic field surrounds the conductor [8].

However, within the SIW section, the dominant mode is like the TE_{10} mode in rectangular waveguides, where there is no electric field component along the direction of propagation ($E_y = 0$), while the magnetic field component is non-zero ($H_y \neq 0$). Given the striking resemblance in the dispersion characteristics of both SIW and rectangular waveguides, as explained in the preceding chapter (Section 2.3.1), the excited field for the dominant TE_{10} mode can be described as follows [8]:

$$H_y = A_{10}\, cos(\frac{\pi x}{W_{WG}})\, e^{-j\beta y} \tag{3.17}$$

$$E_z = -A_{10}\, \frac{\omega \mu W_{WG}}{\pi}\, sin(\frac{\pi x}{W_{WG}})\, e^{-j\beta y} \tag{3.18}$$

$$H_x = A_{10}\, \frac{\beta W_{WG}}{\pi}\, sin(\frac{\pi x}{W_{WG}})\, e^{-j\beta y} \tag{3.19}$$

$$E_x = E_y = H_z = 0 \tag{3.20}$$

where A_{10} is the arbitrary amplitude constant for the mode.

Subsequently, the field will leak into the PPW from this leaky SIW T-Junction and couple into the TEM mode. Inside the PPW region, there are no y-directed field components for the TEM mode ($E_y = 0$, $H_y \approx 0$) [8]. Furthermore, upon truncating the PPW, the TEM mode will couple into the TM_0 SW mode inside the GDS. The field distribution here precisely aligns with the illustration in Section 2.3.2.5, where ($E_x, H_y, H_z = 0$) and ($H_x, E_y, E_z \neq 0$) as represented in Equation 2.26. The fields in the matching section are the same as those in the GDS, where this section is designed to facilitate a smooth transition from the TEM mode in the PPW to the TM_0 mode in the GDS, as previously explained.

3.5 Simulations and Measurements

The quasi-endfire SWA was fabricated and measured in a calibrated anechoic chamber. Results are reported in Figures 3.7-3.12. Agreement was also generally observed between the simulations and measurements.

A minor frequency shift can be noted for the reflection coefficient in Figure 3.8, which is likely related to possible manufacturing tolerances, including via drilling, metallization, and substrate property variation. To understand this frequency shift further, additional simulations were performed for different relative permittivities. After this parametric analysis, results suggested that $\epsilon_r \approx 2$, is more representative of the substrate at about 18 GHz (rather than ϵ_r = 2.2 as rated on the data sheet [134], which is probably due to the anisotropy effect [135]). This effect is also shown in Figure 3.10 where there is a better agreement between the simulated and measured RG versus frequency. This noted frequency shift in $|S_{11}|$ and the RG is also likely related anisotropy of the GDS, where the relative dielectric constant in the vertical direction can be different than the horizontal direction at higher frequencies [135], [136], [137]. This anisotropy, which can be significant for thick substrates, is a result of manufacturing and has some frequency dependence (see [135] pp. 758, Appendix A). As discussed in [136], by changing the value for the dielectric constant (a similar procedure was reported in [120]), a better agreement between simulations and the measurements can be observed.

When the SWA is attached to the satellite body, there is little effect on its performance as observed in the dashed lines of Figure 3.8 due to the presence of a large ground plane (Figure 3.9 displays a screenshot from CST illustrating the simulated model of the SWA integrated with the CubeSat). Also, the measurements imply that the centre frequency for the quasi-endfire SWA is higher than originally intended. In fact, results depicted in Figure 3.8 show that the centre frequency for the fabricated structure was around 18.6 GHz and not 18.1 GHz as per the original design. This can be observed by checking the measured $|S_{11}|$, which is below -15 dB at around 18.6 GHz.

Simulation and measurement results for the far-field beam patterns are shown in Figures 3.7 and 3.11. The maximum measured realized gain is 13.3 dBi at 18.6 GHz (due to the shifted frequency of operation) in the yz plane ($\phi = 90^\circ$) (see Figure 3.7), which is slightly reduced in comparison to the simulated 14 dBi. This gain reduction is likely related to the noted practical change in the ϵ_r value and to the employed connector. Also, the simulated radiation efficiency

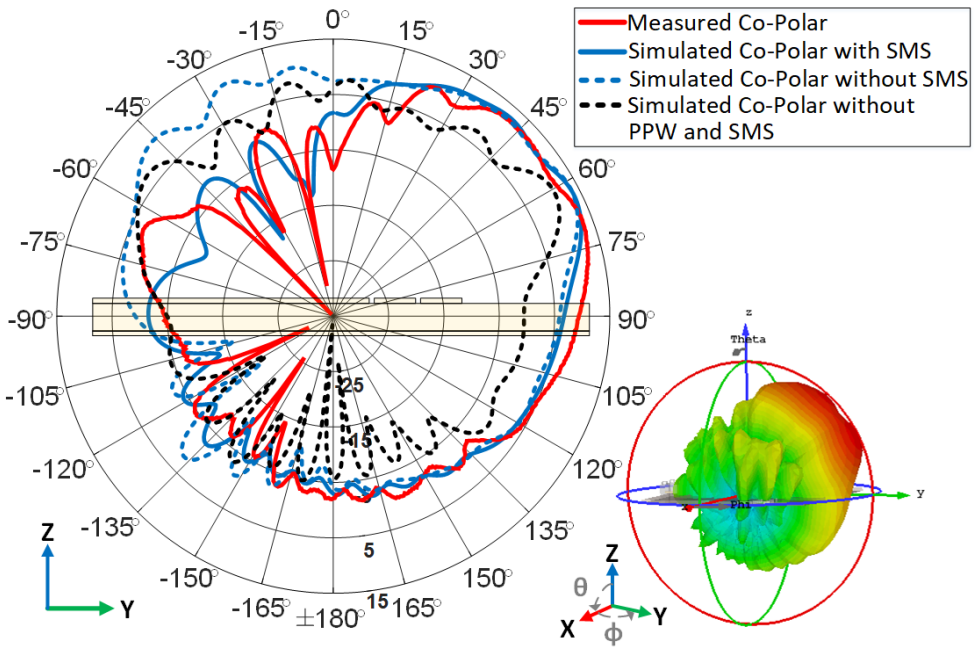

Figure 3.7: *Simulated and measured beam patterns in the yz plane ($\phi = 90°$). Measured results are plotted at 18.6 GHz. Dashed lines represent the simulated beam patterns without the SMS and without the PPW and SMS. The simulated 3D pattern is also reported (right) [From [110] ©2021 IEEE].*

is over 92% with and without the connector from 18 GHz up to 18.8 GHz. However, the total efficiency is between 84% and 95% for the antenna without the connector and between 75% to 94% with the connector for the same frequency range.

The measured RG in the xy plane ($\theta = 90°$) (see Figure 3.11) is 5.5 dBi. This value is significantly lower because the main beam is pointing towards quasi-endfire ($\theta = 70°$) and not full endfire ($\theta = 90°$). Regardless of the practicalities mentioned above, general agreement between the simulated and measured beam patterns can be observed. Figure 3.12 also reports the measured beam patterns for the the yz plane ($\phi = 90°$) over a wide frequency range from 18.1 GHz up to 18.7 GHz. It can be observed that the pointing angles and SLLs are very similar through frequency. These features can support high data-rate downlink communications. Also, as compared to other antennas in the literature [138] - [143], our proposed SWA offers a very competitive high radiation efficiency while maintaining a compact structure size. This is outlined in Table 3.2. Figure 3.13 displays the CST mesh calculations, showing a high density of calculations near the vias and the connector pin.

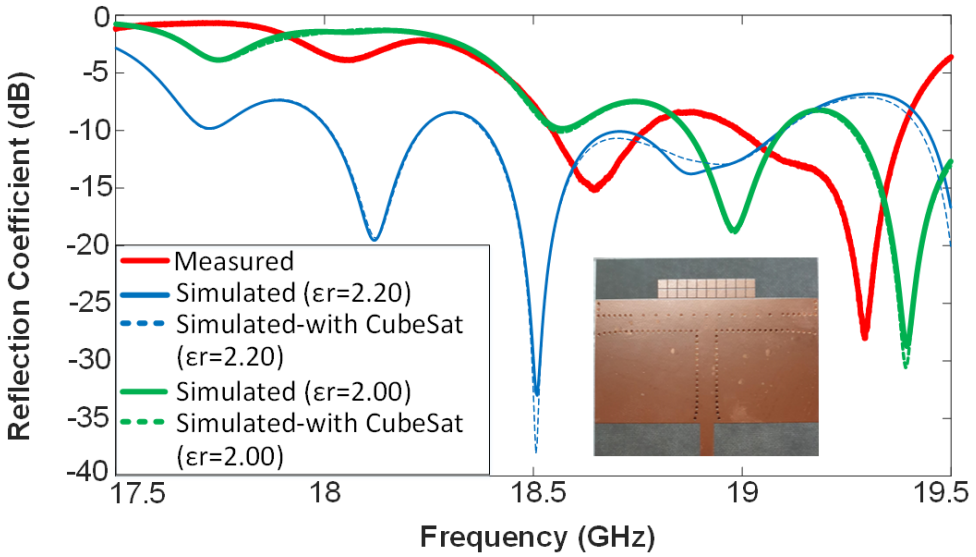

Figure 3.8: *Reflection coefficient versus frequency for the designed SWA (see inset). It should be pointed out that initial simulations were completed considering $\epsilon_r = 2.2$ (blue solid line) while the green lines consider practical permittivity tolerances. Simulations on the CubeSat body are also reported [From [110] ©2021 IEEE].*

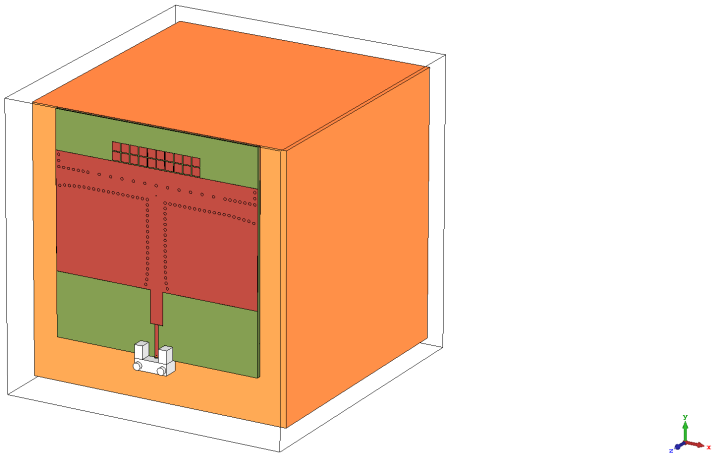

Figure 3.9: *Screenshot of CST simulation model of the proposed antenna with the CubeSat.*

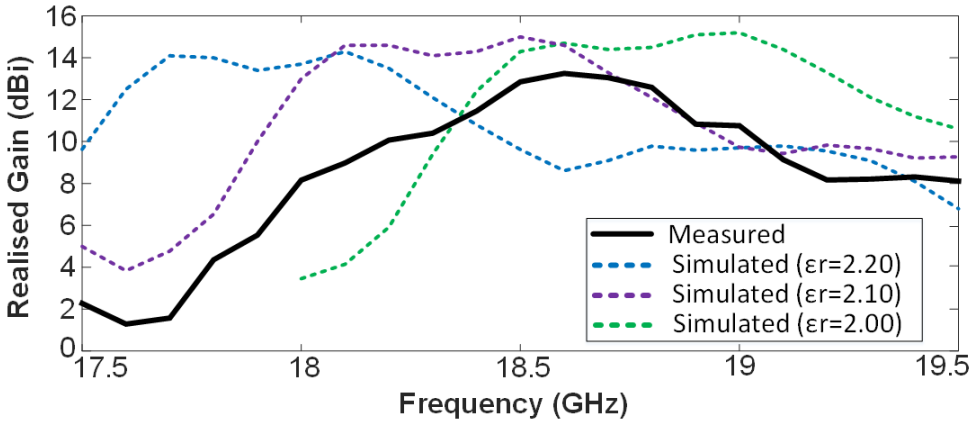

Figure 3.10: *Measured and simulated maximum RG in the yz plane [From [110] ©2021 IEEE].*

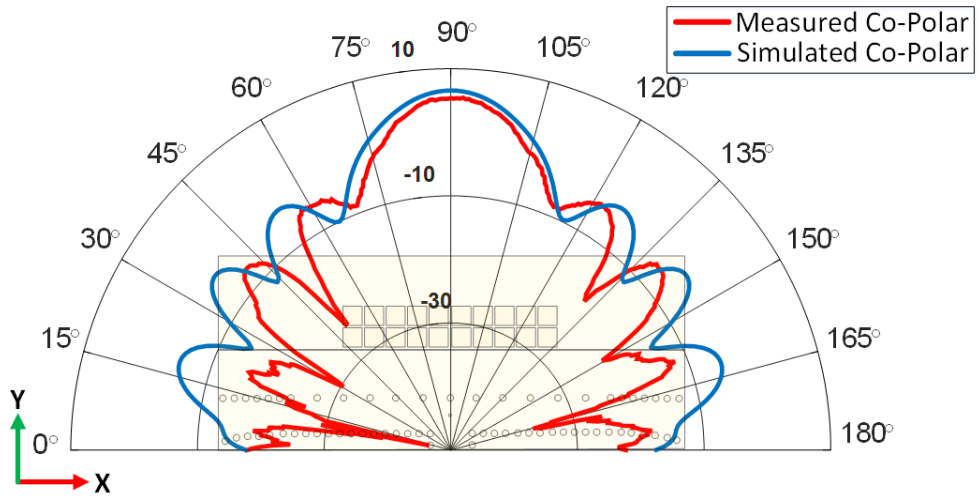

Figure 3.11: *Simulated and measured beam patterns in the xy plane ($\theta = 90°$) [From [110] ©2021 IEEE].*

Work	Frequency	Max Realised Gain	Technology	Radiation Efficiency	Structure Size
[138]	28 GHz	9.5 dBi	Microstrip	-	$11.2\lambda_0 \times 6.5\lambda_0$
[139]	14 GHz	18.0 dBi	Metasurface	-	$8.0\lambda_0 \times 7.0\lambda_0$
[140]	28 GHz	8.1 dBi	SIW	-	$2.8\lambda_0 \times 2.6\lambda_0$
[141]	30 GHz	15.9 dBi	SIW	79%	$5.5\lambda_0 \times 5.0\lambda_0$
[142]	34 GHz	11.4 dBi	Microstrip	85%	$1.7\lambda_0 \times 0.6\lambda_0$
[143]	28 GHz	10.0 dBi	Coplanar	90%	$13.2\lambda_0 \times 6.6\lambda_0$
[144]	17 GHz	16.2 dBi	Dielectric Rod	-	$5.6\lambda_0 \times 0.6\lambda_0$
Proposed Work	18 GHz	14.0 dBi	SIW	94%	$5.0\lambda_0 \times 4.8\lambda_0$

Table 3.2: *Endfire Antenna Comparisons (Optimized Results)*

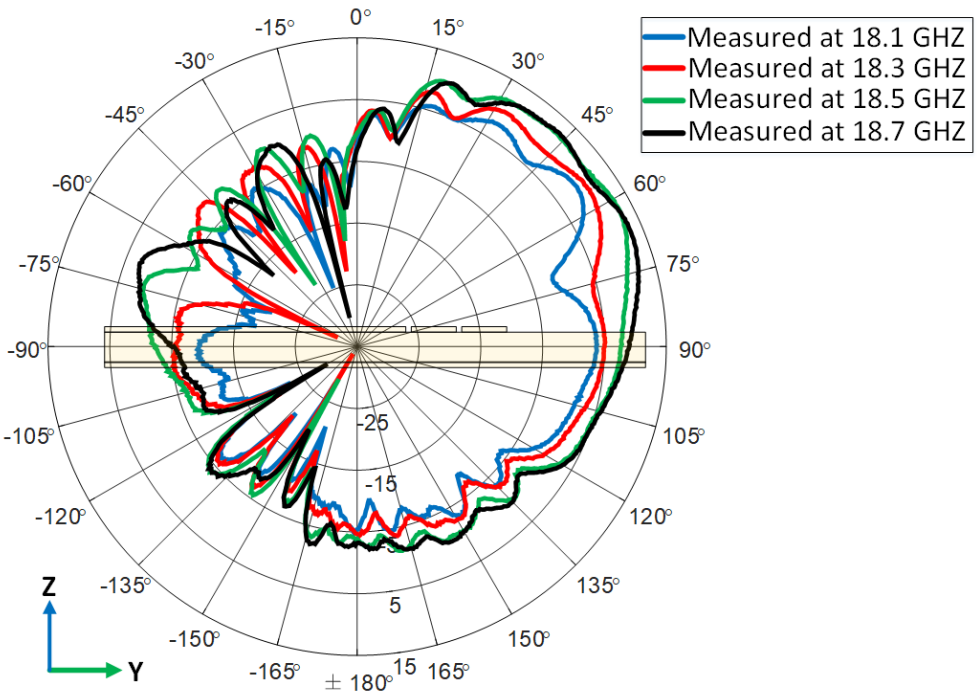

Figure 3.12: *Measured beam patterns for different frequencies from 18.1 to 18.7 GHz in the yz plane ($\phi = 90°$) [From [110] ©2021 IEEE].*

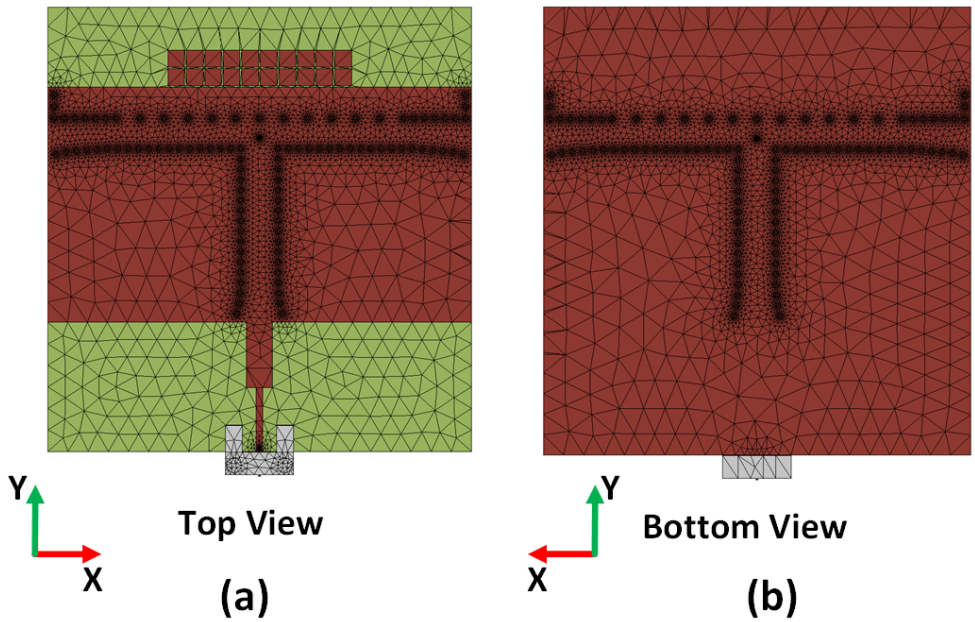

Figure 3.13: *Top and bottom views of the CST mesh calculation screenshot for the proposed antenna structure.*

3.6 Summary

A planar quasi-endfire SWA has been introduced in this chapter for endfire operation at K-band. The structure has been designed using SIW technology for integration on CubeSats and other small satellites. This quasi-endfire performance has been achieved by edge radiation of the fundamental TM_0 SW mode from a GDS. This mode was efficiently excited by a leaky SIW T-junction, which created a uniform wavefront that propagates through a truncated PPW. A matching section was also included which was based on an array of subwavelength patches placed at the interface between the PPW and the GDS for a smooth transition and reduced structure reflections. The fabricated SWA obtained a RG of 13.3 dBi, demonstrating also good agreement between the simulated and measured beam patterns. The next chapter extends and enhances this design, such that radiation is directly at endfire.

Chapter 4
Planar Surface Wave Antenna with Directive Radiation Exactly at Endfire

4.1 Introduction

In Chapter 3, the focus was to design a quasi-endfire surface wave antenna (SWA) by radiation of the fundamental TM_0 surface wave (SW) mode at the edge of a grounded dielectric slab (GDS). The structure is excited by a leaky substrate integrated waveguide (SIW) T-junction that creates a uniform wavefront which propagates through a truncated parallel-plate waveguide (PPW). A sub-wavelength matching section (SMS) was added between the PPW and GDS as an interface to smooth the transition and improve the antenna radiation performance. In this chapter, the new focus is to achieve a competitive and truly endfire, high gain antenna by introducing an air via (AV) section. A distributed aperture principal is also newly proposed for the structure, and the transverse equivalent network (TEN) approach is developed using the theory and closed-form equations, mainly in an effort to fully model the structure.

4.2 Background Literature

SWAs are a class of travelling-wave antenna with generally an endfire-like beam pattern in the far-field, offering high gain and vertical polarisation. These antennas are widely implemented on various platforms because they are low profile, lightweight, and structurally compatible with various surfaces [87]. Moreover, SWAs can be metallic-based or implemented using PCB technology, with or without metal backing, where the excited SWs are radiated at discontinuities, e.g., at corrugations or at structure truncation.

Some recent studies on SWAs were reported in [145] - [149] using perhaps conventional guided-wave structures and transmission line implementations. For example, a tapered-width SWA based on SIW technology was recently proposed in [145] for K-band operation. This design has the benefits of being planar with simple fabrication and results demonstrated realised antenna

gain up to about 18 dBi. The use of metasurfaces to design low-profile endfire antennas was also examined in [146]. In that work, the propagation characteristics were analysed by the magnetic field integral equation technique and measurements showed near-endfire beam patterns with gain ranging from 12.3 to 15.3 dBi over a broad bandwidth (BW) from 9.6 to 13.6 GHz. A low-profile SWA implementation [149] was also recently studied achieving a wide operational BW from 6 to 18 GHz with quasi-endfire radiation. In addition, a SW phased array with tapering and high gain, and broadband characteristics was also proposed in [147] covering the X-band. Also in [148], a microstrip-fed SWA was reported using an air gap region and a top dielectric cuboid. This non-conventional structure, defined a half-mode dielectric waveguide with radiation due to SWs and a maximum endfire gain of 13.3 dBi at 4.75 GHz.

One challenge with SWAs, as outlined in [145] - [149], is achieving directive beams over a broad frequency range, and, exactly at endfire. This is due to their inherent frequency dependence and limited control over radiation patterns, necessitating creative design approaches to overcome these limitations and optimise antenna performance. This complexity arises from the special propagation characteristics of SWs and the need to carefully control antenna parameters to achieve the desired radiation performances. This can also be observed in the recent trend for SWAs to be integrated within deployable solar panel arrays [150], [151] for CubeSats and other SmallSats, and on the satellite structure itself [110] for example. More specifically, in [151] quasi-endfire radiation was reported using a yagi-uda array of patches for operation at about 8 GHz with realised gain values above 0 dBi when implemented directly on a thin solar cell array whilst considering a silicon substrate. An impedance matching BW of 0.65% was observed. However, a compact structure offering endfire radiation was demonstrated in [150] which offered a BW of 6.25%. In that work, meandering and artificial dielectric concepts were implemented on an FR-4 substrate for operation at 2.4 GHz and peak gain values approached 5 dBi at full-endfire (i.e. 90°). The compact K-band design in [110] also demonstrated quasi-endfire radiation where the beam approached 70° with realised gain values over 13 dBi and high sidelobe levels (SLLs) whilst using leaky wave (LW) SIW feeding and SW radiation at truncation.

4.3 Chapter Overview

Following the previous developments outlined in Section 4.2, this chapter newly reports on a new K-band SWA with high gain, low SLLs, and directive radiation exactly at endfire. SW

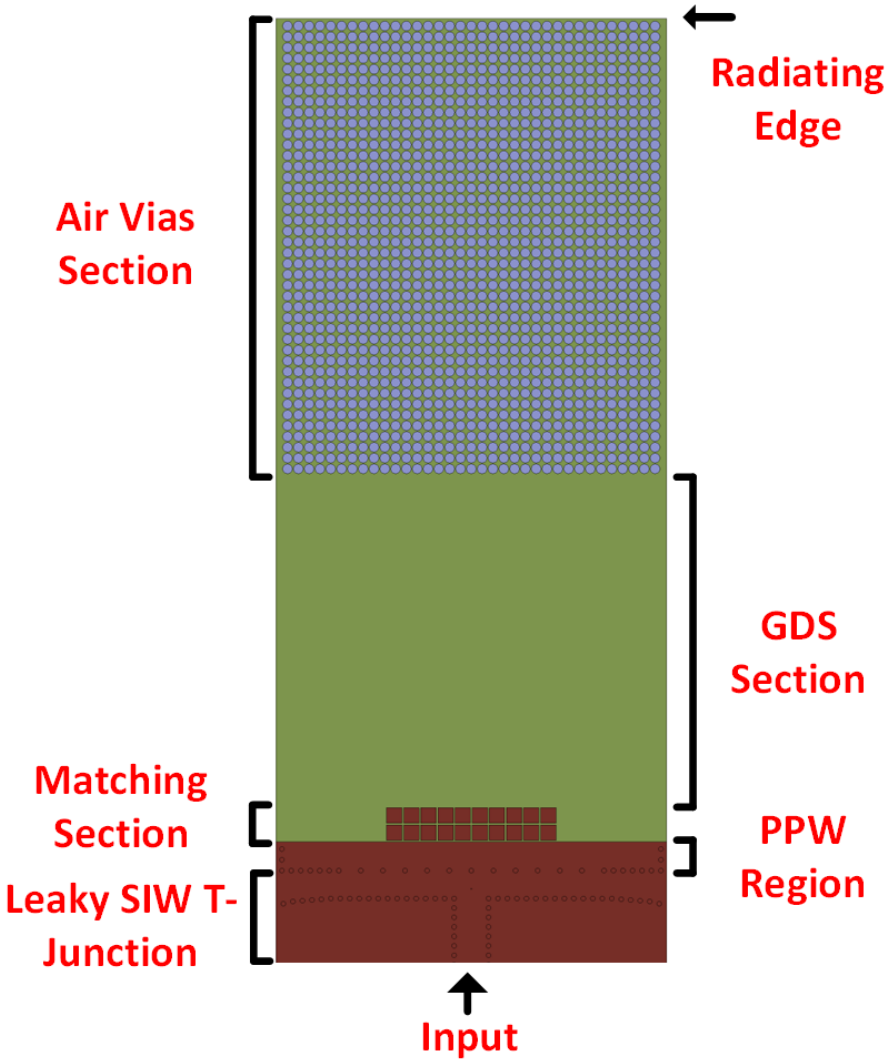

Figure 4.1: *Top and bottom view of the proposed SWA were the different sections for the structure are defined. Note: both sides of the SWA are analogous.*

radiation is achieved by using a cascade of different SW guiding sections defined by PPW, sub-wavelength patches, a GDS region, and an air-hole via section (see Figures 4.1 and 4.2). These effective matching sections ensure a gradual transition for the travelling SWs from the feeder into the GDS and AV regions to be radiated into air at the truncated edge with minimal reflections. This structure arrangement offers efficient radiation which is more than 90%.

To achieve directive radiation at endfire, a two-layer structure is proposed herein with a common ground plane (see the cross-section in Figure 4.2(a)). This implementation exploits differential feeding and basically duplicates or mirrors the planar SWA for both the top and bottom layers allowing for simple and more flexible assembly. Moreover, this two-antenna design effectively

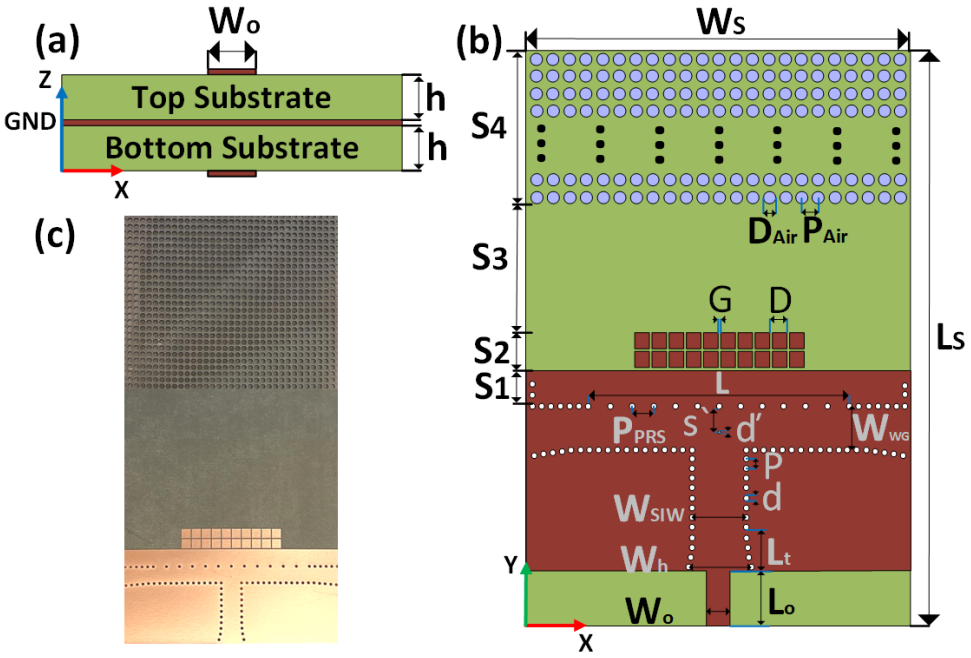

Figure 4.2: *(a): Cross-section view for the SWA where the two dielectric layers are illustrated as well as the ground plane and input microstrip lines (top and bottom). This basically defines two stacked SWAs with a common ground plane. (b): Top or bottom view for the SWA where the optimised dimensions are outlined (see Table 4.1). (c): Photograph of the fabricated prototype.*

distributes the launched SWs at the edge of the guiding structure for in-phase radiation and this defines a shared radiating aperture (see Figures 4.1 and 4.2) or a distributed SW aperture which is common for both planar SWAs. A comparison is also made in the chapter to a single-layer implementation, which is more conventional achieving quasi-endfire radiation only, as well as, the aforementioned dual-layer version.

Applications for the antenna include endfire radiation and where low-profile and low-cost designs are required. The SWA can also be suitable for small satellite integration, similar to the scenarios reported in [110], [150], [151], whilst providing a solution to achieve directive gain exactly at endfire and with low SLLs. With these motivations in mind and given that air holes are used within guiding structure, the SWA becomes semi-transparent and this allows for solar panels to be located underneath the AV regions (as illustrated in Figure 4.3). In addition, solar panels can also be placed on top of the metallic guidance sections within the SWA. To the best knowledge of the authors, no similar low-profile antenna structure for SWs and solar cell co-location have been reported previously.

Design motivations, detailed numerical analysis, simulations, and measurements investigating the performance of a fabricated prototype are reported in the chapter. More specifically, an overview of the antenna design guidelines are provided in Section 4.4. Details of the employed TEN approach to model the SIW feeder and SWA are also reported therein. Discussions on the simulation approach for the single- and dual-layer structures and an examination of the AV section is documented in Section 4.5. Simulations and measured results are reported in Section 4.6, while Section 4.7, summarises these findings.

4.4 Motivations, Analysis & Design

CubeSats and other small satellites are typically sized in multiples of one cubic unit $10 \times 10 \times 10\,\text{cm}^3$, (i.e. 1U). Thus, it is essential that the electronics, especially the antennas be economical, as small as possible, and, low-profile to meet these volume constraints [1], [3], [7]. Any size and weight restrictions must be considered throughout the antenna design stages whilst also adhering to this CubeSat standard.

Given these crucial factors, non-deployable antenna systems might be the option to guarantee reliable satellite operation [2], [3]. One interesting advantage of these non-deployable systems is that satellite elements, such as the solar panels, can also be used as the antenna surface, as investigated in [21] - [24]. As a result, more room is made available on the satellite itself for communication equipment, additional sensor technologies, more solar cells, etc. and this approach to the satellite design can foster more advanced mission capabilities. Also, with more solar cells, battery charging capacities can improve. Applications for the SWA include high data rate downlink satellite communications, for example, Earth and planetary observations or intersatellite links.

Figure 4.3 illustrates possible placement of the SWA on a 3U CubeSat; i.e. different ways in which the solar cells can be integrated underneath the AV section and on top of the GDS and metallic parts of the SWA. Possible stationary and deployable implementations of the solar panels integrated with the SWA are also shown. This defines suitable dual-functionality, in that the proposed antenna can also act as structure were solar cells can be co-located with the planar antenna. Similar concepts were also reported in [21], [110] and [152] (see also ref. therein). Depending on the power budget and design and mission requirements of the CubeSat itself, a deployable or non-deployable setup might be preferred. In particular, a deployable design might

W_s	L_s	S_1	S_2	S_3	S_4	D_{Air}	P_{Air}	G	D	L	P_{PRS}
79.5	212.3	5.3	7.0	68.0	92.7	2.0	2.2	0.3	3.5	54.0	4.5
S'	d'	W_{WG}	P	d	W_{SIW}	W_h	L_t	W_o	L_o	h	ϵ_r
3.2	0.2	5.7	1.9	1.0	7.0	8.6	8.9	4.9	12.2	1.6	2.2

Table 4.1: *SWA Dimension for the Structure as Illustrated in Figure 4.2 (Dimensions in Millimetres)*

be needed to allow more space for other sensors on the CubeSat platform or a non-deployable might be required for simplicity and robustness.

It should also be mentioned that the feeder for the SWA utilises an updated version of the PPW launcher, reported in [82] and [110]. Motivations for those works were for feeding PPW-based slotted antenna arrays and compact SWAs. In particular, the major aperture size of the design in [110] was about $3\lambda_0$ and achieved quasi-endfire radiation only. Also, the efficiency for both structures was more than 90%, and this encouraged the modification and adaption of this SIW feed system when realising the proposed two-layer SWA.

4.4.1 Radiation Principles by Cascaded Matching & Guidance

The proposed SWA is based on LW feeding and SW radiation principles for operation at 18 GHz whilst employing microstrip and SIW technology [117], [118]. The new antenna structure can be divided into five-parts (see Figure 4.1). Optimised dimensions for the fabricated K-band design are outlined in Table 4.1. The leaky SIW T-junction feeds the SWA, which is basically designed to excite a uniform and guided, plane-wave inside the PPW region. Next a matching section using an array of sub-wavelength patches was employed [110] and this was included to minimise reflections into the GDS region whilst maintaining the noted uniform phase front. Further details on this leaky SIW T-junction feeder and SMS can be found in [82] and [110].

For directive endfire radiation, an extended GDS for SW radiation and an AV section was also included between the GDS and the radiating edge. This made the length and width of the SWA to be about $10\lambda_0$ by $3\lambda_0$, respectively. This ensured that the travelling SWs from the SIW feeder experienced a more gradual transition when radiating into air (as compared to [110] which was shorter in structure length; i.e. only $5\lambda_0$ and did not employ AVs and an extended GDS region). The new design approach reported in this chapter also fosters more standard travelling-wave features to achieve high gain. Basically, this is due to the fact that the proposed SWA is electrically longer than the compact version reported in [110] and this supports a larger

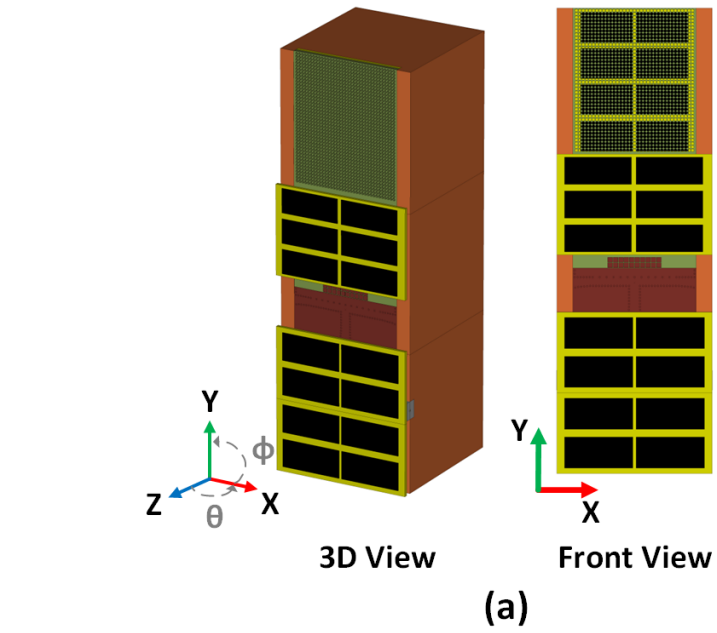

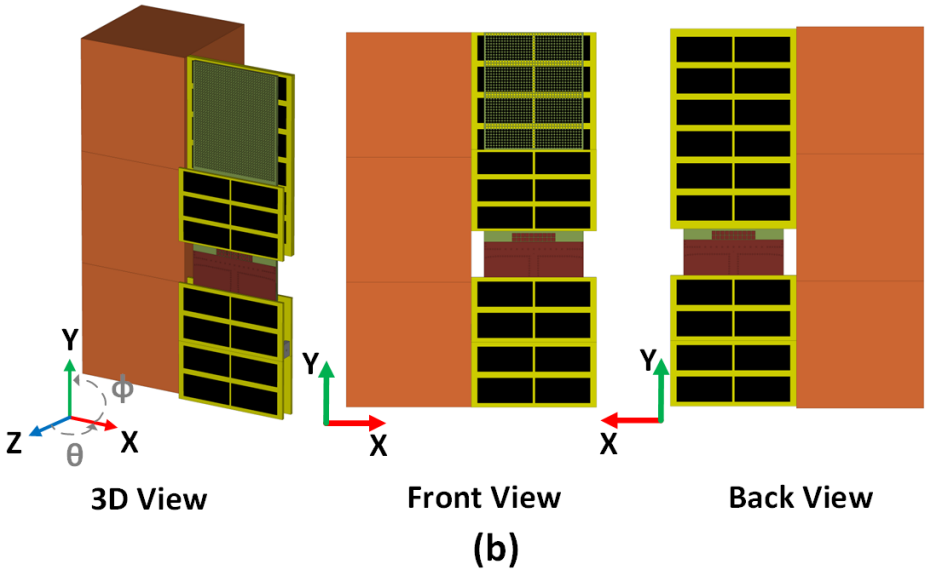

Figure 4.3: *Examples of possible placement for the proposed SWA on a 3U CubeSat: (a) 3D and front view where the SWA is placed on one side of CubeSat with the solar cells integrated underneath the AV section and on top of the GDS region, (b) 3D, front, and back views where the SWA and solar cells are deployed (similar to [150]). The structure that is mechanically more stable is the non-deployable one, denoted as (a).*

effective aperture.

This more lengthy structure and cascaded matching section design approach generally follows conventional $\lambda_g/4$ transformer concepts where $\lambda_g = 2\pi/\beta_g$ (here λ_g is the guided wavelength in the relevant region and β_g is the associated phase constant). The same matching section design approach also applies to the AV section which was included to prevent an abrupt transition into the air region (where $\beta_0/k_0 = 1$). Similarly, from the TEM mode inside the PPW ($\beta_g/k_0 = \sqrt{\epsilon_r}$) to the TM_0 SW mode of the GDS ($\beta_g/k_0 < \sqrt{\epsilon_r}$). Also, by this design flexibility β_g in the AV section can be tailored by the spacing and size of the drill holes such that the phase constant in this region is greater than air but less than the GDS section; i.e. $1 < \beta_g < \sqrt{\epsilon_r}$.

Given this cascaded matching approach when designing this SWA, guided-waves from the feeder are slowly transitioned into the different regions and eventually air. Also, as further examined in the next few sections of the chapter, the lengths of these regions are selected to reduce the SLLs and increase the realised antenna gain while also maintaining compact dimensions to reduce structure losses. In addition, these GDS and AV sections, which are not selected to be as short as possible (i.e. $\lambda_g/4$), but suitably longer to support the travelling-wave principles required for SW radiation. In particular, section lengths were chosen to be $n\lambda_g/4$, where $n >> 1$ and n is a positive integer. These design choices made the major dimension of the structure to be about $10\lambda_0$ in length to support travelling-waves for edge radiation.

4.4.2 Transverse Equivalent Network for the Proposed SWA

To further describe the design and analysis of the proposed SWA, a TEN model [8] will be developed in this section. This will help to characterise the dispersive features for the relevant LW fields within the SIW T-junction as the employed matching sections and air region (at the end of the structure), act as a combined load to the feeder. As a result, the complex LW propagation constant ($\gamma_{LW} = \alpha_{LW} + j\beta_{LW} = jk_x$) can be calculated using the transverse resonance technique (TRT) [8].

Figure 4.4 illustrates the equivalent structure and schematic of the TEN model. The non-leaky perfect electric conductor (PEC) via wall is symbolised by a short circuit on the left side. Moving toward the right on the schematic, a transmission line of length W_{WG} is defined. This is the space between the PEC vias and the sparse via wall, which is defined as a partially reflective screen (PRS), for leakage into the PPW region [82], [110]. After that, a T-network characterises

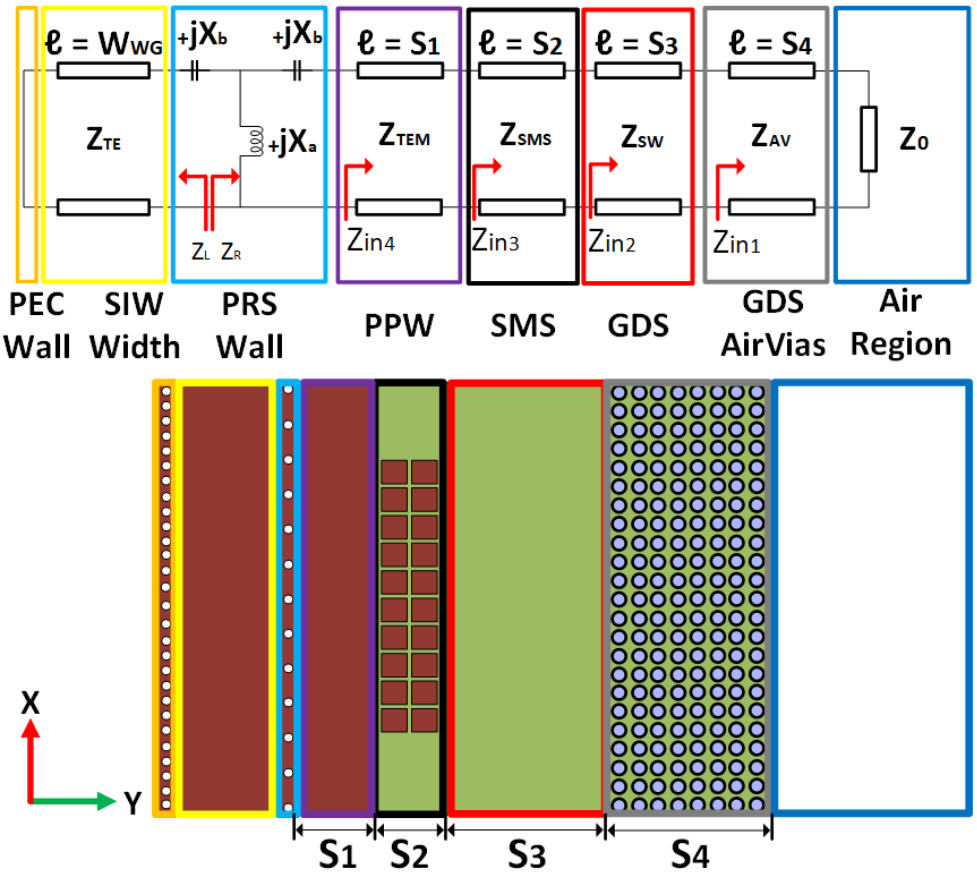

Figure 4.4: *TEN circuit model and the corresponding SWA. Note the common colours for each part of the SWA within the TEN circuit and highlighted for the representative section.*

these PRS vias. More specifically, this is modelled with two series capacitors and one centre inductor in parallel [153], which are effectively inductive posts in the PPW.

Four transmission line sections follow this T-network afterwards and have a loading effect on the feeder. The first transmission line, with a length of S_1, is the distance between the edge of the PPW and the PRS via wall. Second, with a length of S_2, is the space between the PPW edge and the second edge of the sub-wavelength patches. Third, with a length of S_3, is the distance between the SMS and the first row of the AV section; i.e. the GDS length. The fourth transmission line, with a length S_4 corresponds to the length of the GDS with additional AVs. The termination impedance of air is the final component for this model.

The transverse resonance equation (TRE) at the reference point (see Figure 4.4) is enforced to determine the dispersive behaviour of the leaky SIW T-junction. This equation is [8]:

$$Z_L(k_y) + Z_R(k_y) = 0 \tag{4.1}$$

where $Z_L(k_y)$ and $Z_R(k_y)$ are the input impedances on the left and right of the reference plane and are defined as

$$Z_L(k_y) = jZ_{TE}(k_y)\tan(W_{WG}k_y) - jX_b(k_y) \tag{4.2}$$

$$Z_R(k_y) = \frac{jX_a(k_y)(Z_{in_4}(k_y) - jX_b(k_y))}{jX_a(k_y) + Z_{in_4}(k_y) - jX_b(k_y)}\,. \tag{4.3}$$

The transverse wavenumber k_y and the characteristic impedance for the TE_{10} mode inside the SIW, Z_{TE}, are explained in the following:

$$k_y = \sqrt{k_0^2\epsilon_r - k_x^2} \tag{4.4}$$

$$Z_{TE}(k_y) = \frac{\omega\mu_o}{k_y}\,. \tag{4.5}$$

Moreover, X_a and X_b are the capacitances and inductance for the T-network as defined in [153]:

$$\begin{aligned} X_a(k_y) = Z_{TE}(k_y)\Bigg(\frac{P_{PRS}\cos\phi(k_y)}{\lambda}\Bigg(\ln\frac{P_{PRS}}{2\pi\frac{d}{2}} + \\ +0.601(3-2\cos^2\phi(k_y))\Big(\frac{P_{PRS}}{\lambda}\Big)^2\Bigg)\Bigg) \end{aligned} \tag{4.6}$$

$$X_b(k_y) = Z_{TE}(k_y)\left(\frac{P_{PRS}\cos\phi(k_y)}{\lambda}\Big(\frac{2\pi\frac{d}{2}}{P_{PRS}}\Big)^2\right) \tag{4.7}$$

where

$$\cos\phi(k_y) = \frac{k_y}{k_o\epsilon_r}\,. \tag{4.8}$$

In addition, the input impedances Z_{in_4}, Z_{in_3}, Z_{in_2} and Z_{in_1} can be determined as

$$Z_{in_4}(k_y) = Z_{TEM}\left(\frac{Z_{in_3}(k_y) + jZ_{TEM}\tan(S_1k_y)}{Z_{TEM} + jZ_{in_3}(k_y)\tan(S_1k_y)}\right) \tag{4.9}$$

$$Z_{in_3}(k_y) = Z_{SMS}\left(\frac{Z_{in_2}(k_y) + jZ_{SMS}\tan(S_2k_y)}{Z_{SMS} + jZ_{in_2}(k_y)\tan(S_2k_y)}\right) \tag{4.10}$$

$$Z_{in_2}(k_y) = Z_{SW}\left(\frac{Z_{in_1}(k_y) + jZ_{SW}\tan(S_3k_y)}{Z_{SW} + jZ_{in_1}(k_y)\tan(S_3k_y)}\right) \tag{4.11}$$

$$Z_{in_1}(k_y) = Z_{AV}\left(\frac{Z_0 + jZ_{AV}\tan(S_4k_y)}{Z_{AV} + jZ_0\tan(S_4k_y)}\right) \tag{4.12}$$

where Z_{TEM} (= $\eta h/S_1$) is the characteristic impedance for the TEM mode inside the PPW [8], Z_{SMS} (= $\beta_{SMS}/\omega\epsilon_r\epsilon_o$) is the impedance of the SMS (calculated by using the code in Appendix B.1), Z_{SW} (= $\beta_{SW}/\omega\epsilon_r\epsilon_o$) is the impedance of the GDS (calculated by using the code in Appendix B.2), Z_{AV} (= $\beta_{AV}/\omega\epsilon_{r_{eff}}\epsilon_o$) is the impedance of the AV region (calculated by using the code in Appendix B.3), and Z_0 (= $\beta_0/\omega\epsilon_o$) is the impedance of the air region. Additionally, h is the thickness of the substrate, β_{SMS} is the phase propagation constant for the SMS, β_{SW} is the phase propagation constant for the GDS, β_{AV} is the phase propagation constant for the AV section, β_0 is the phase propagation constant for the air region, and $\epsilon_{r_{eff}}$ is the relative effective permittivity for the AV section and defined by [154]:

$$\epsilon_{r_{eff}} = \frac{\epsilon_r\left(P_{Air}^2 - \pi\dfrac{D_{Air}^2}{4}\right) + \pi\dfrac{D_{Air}^2}{4}}{P_{Air}^2} \tag{4.13}$$

where P_{Air} is the AV post separation and D_{Air} is the diameter for the AVs.

Figure 4.5 depicts the results for the TEN analysis (which has been calculated using the codes in Appendix B) considering that there are no dielectric and conductor losses, while also fol-

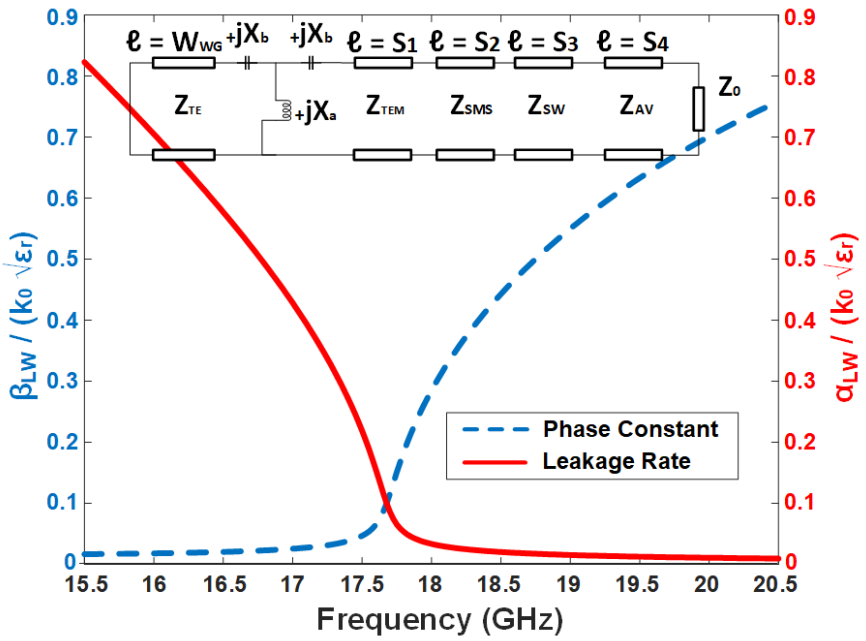

Figure 4.5: *Numerically determined attenuation and phase constants, α_{LW} and β_{LW}, respectively, for the leaky SIW T-junction feeder representing the complex solution for the TRE (with k_0 normalisation). Results show that the SWA is designed to work at about 18 GHz.*

lowing the dimensions in Table 4.1. It can be observed that $\beta_{LW} \approx \alpha_{LW}$ at about 18 GHz which is the desired frequency of operation for the optimised, prototyped and fabricated SWA. This LW mode dispersion analysis for the SIW feeder can be used to initially determine the dimensions of this feed system while including the aforementioned matching sections. This will identify the ideal structure parameters to test its performance using CST Microwave Studio, and then simulations will determine the more realistic representation of the parameters. This approach is further investigated in Appendix C for analogous designs which show operation at millimeter-wave frequencies; i.e. 55 GHz, 77 GHz, and 110 GHz. This is documented for further validation and to report on a basic parametric study for the developed TEN model as well as the scalability of the structure itself. The next section further reports on the investigated K-band SWA using a commercial full-wave solver.

4.5 Design, Simulation Results, & Discussions

This section will further outline our design process by comparing the single-layer structure with the two-layer design as well as the benefits of the AV section and the other cascaded sections.

Also, the differential feeding of 180° for the two-layer SWA is studied and its practical feeding implementation.

4.5.1 Single-layer Design & Operation

Starting from the earlier SWA in [110] which operated at 18 GHz and achieved quasi-endfire radiation, this section will investigate the impact of the extended antenna length and the added AV section. Moreover, an assessment on different dimensions for the PPW and GDS sections is also reported. Firstly, introducing the AV section in the design of the SWA provides an additional degree of freedom, and this will allow for a less abrupt transition for the travelling SWs from the feeder. The effective dielectric constant $\epsilon_{r_{eff}}$ for the AV section can be calculated using Equation 4.13. Using this information whilst maintaining lengths of $n\lambda_g/4$ for the various cascaded regions, the SWA performance for different lengths of the PPW, GDS, and AV sections and the resulting beam patterns were studied.

Table 4.2 compares the realised gain (RG) and the SLL for the ϕ and θ planes at 18 GHz for different lengths S_1 of the PPW region. Also, the main lobe direction (MLD) has been studied. Moreover, for this study, the GDS length was held constant at 8 mm (as in [110]) and the AV section was also fixed at 12 rows with $D_{Air} = 2$ mm and $P_{Air} = 2.2$ mm. See Table 4.1 for all other relevant structure dimensions. It can be noticed that there is an inverse relationship between the PPW dimension and the MLD; i.e. when the PPW length increases the MLD moves away from endfire or 90°. This is undesired. It should also be noted that the RG increases for the ϕ and θ cuts when the PPW dimension increases for the following lengths: $\lambda_g/2$, λ_g, and $3\lambda_g/2$. Given that a finite sized structure is required for the aforementioned CubeSat requirements, a PPW length of $\lambda_g/2$ (or 5.3 mm) was adopted, mainly, to achieve high gain and a MLD which approaches 90°.

Table 4.3 studies the GDS section length at 18 GHz whilst fixing the PPW region to be 5.3 mm, also, having 12 rows for the AV section with $D_{Air} = 2$ mm and $P_{Air} = 2.2$ mm. As observed in Table 4.3, the MLD increases toward the endfire direction when the GDS section length increases, and at the same time, the RG slightly increases also. Table 4.4 further explores the peak directity and the MLD for increasing row numbers of the AV section while keeping all other parameters in Table 4.1 constant. Basically, it can be observed that with an increase in the number of AV holes in the substrate at the end of the SWA, the beam direction also approaches endfire. For example, with 10 rows the directivity increases to 15 dBi and with a MLD of 66°.

PPW Length S_1	**18 GHz**				
	yz **plane** ($\phi = 90°$)			xy **plane** ($\theta = 90°$)	
	RG (dBi)	**SLL (dB)**	**MLD**	**RG (dBi)**	**SLL (dB)**
$(1/4)\lambda_g$	10.3	-0.8	74°	7.4	-11.2
$(2/4)\lambda_g$	14.5	-1.8	72°	10.9	-11.9
$(3/4)\lambda_g$	11.7	-2.5	63°	6.5	-12.2
$(4/4)\lambda_g$	14.9	-2.1	62°	10.1	-11.0
$(5/4)\lambda_g$	11.4	-1.0	65°	6.6	-11.7
$(6/4)\lambda_g$	15.4	-2.2	66°	9.6	-11.1
$(7/4)\lambda_g$	11.7	-1.9	64°	5.7	-10.4

Table 4.2: *Single-Layer SWA Performance for Different Lengths of the PPW Section*

GDS Length S_3	**18 GHz**				
	yz **plane** ($\phi = 90°$)			xy **plane** ($\theta = 90°$)	
	RG (dBi)	**SLL (dB)**	**MLD**	**RG (dBi)**	**SLL (dB)**
$(2/4)\lambda_g$	14.5	-2.3	66°	10.4	-16.4
$(3/4)\lambda_g$	14.4	-1.7	72°	10.9	-12.1
$(4/4)\lambda_g$	14.8	-1.3	70°	11.1	-17.8
$(6/4)\lambda_g$	14.8	-1.4	74°	11.6	-12.3
$(7/4)\lambda_g$	15.1	-1.5	73°	11.7	-17.5
$(9/4)\lambda_g$	14.9	-1.4	75°	12.1	-12.7
$(10/4)\lambda_g$	15.1	-1.8	75°	12.1	-16.8
$(14/4)\lambda_g$	15.0	-1.6	78°	12.7	-12.0

Table 4.3: *Single-Layer SWA Performance for Different Lengths of the GDS Section*

With the findings from Tables 4.2, 4.3, and 4.4, it is clear that to achieve a main beam close to endfire, the GDS and the AV regions should be made of typical lengths for a travelling-wave antenna (i.e. more than $7\lambda_0$) while the PPW section should be as short as possible, for example, on the length of $\lambda_g/2$ as selected herein.

It is also useful to compare the SWA with and without the AV section as shown in Figure 4.6. This full-wave simulation illustrates the benefit added by the AV section. For example, it can be observed that the MLD for the SWA with a continuous GDS section is about 63° and that the endfire beam is actually reduced in magnitude, and, defines the first sidelobe maximum. This is related to the mismatch in the SW phase constant for the GDS region and air. Basically, the guided SWs experience an abrupt transition at the edge of structure. On the other hand, the SWA

Number of Rows	18.0 GHz		18.3 GHz	
	Directivity (dBi)	Main Lobe Direction	Directivity (dBi)	Main Lobe Direction
2 Rows	14.4	53°	14.3	53°
4 Rows	14.7	57°	14.7	57°
6 Rows	14.8	61°	14.8	60°
8 Rows	14.9	63°	15.0	63°
10 Rows	15.0	66°	15.0	65°

Table 4.4: *Single-Layer Directivity & MLD for Different Number of Rows for the AV Section*

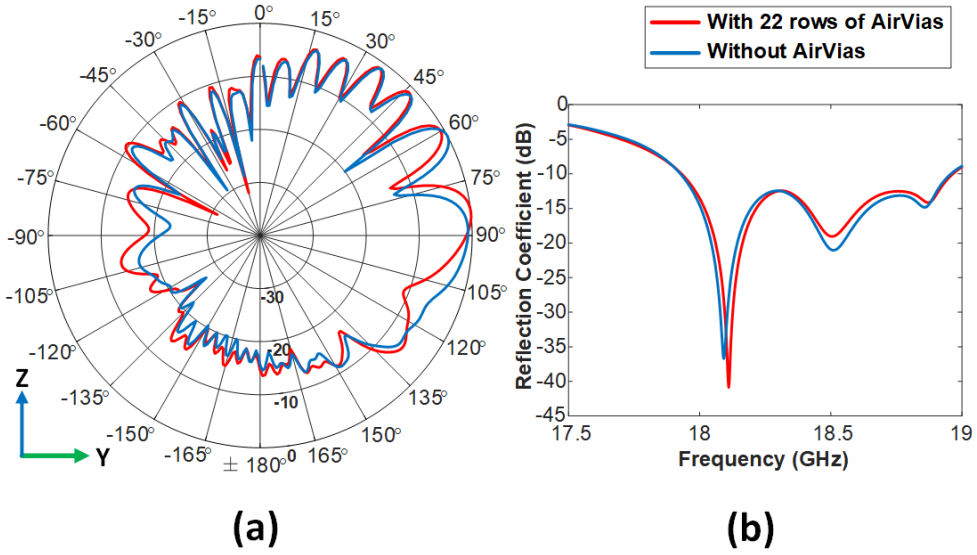

Figure 4.6: *Single-layer SWA simulations: (a) normalised beam patterns in the yz plane ($\phi = 90°$), and (b), the reflection coefficient versus frequency. A comparison is made with 22 rows for the AV section and without the AVs.*

design with the AV section, achieved a MLD of 83°, being only 7° away from endfire. Both structures offered similar reflection coefficient values over frequency (see Figure 4.6(b)), albeit a 4 dB reduction in the minimum for the reflection coefficient for the single-layer structure with AVs.

Using the results and findings from Tables 4.2, 4.3, and 4.4, further optimisations were completed, but a design with low SLLs and a main beam directly at endfire was not possible. Figure 4.7 displays the beam pattern in the yz- and xy-planes for the SWA using only a single layer. This design was defined by an AV section with 42 rows, the GDS was 68 mm and the PPW region was 5.3 mm in length. In addition, the MLD in the yz-plane was $84°$. However, there is a significant problem in that the SLL, which is -0.7 dB, could not be improved after significant

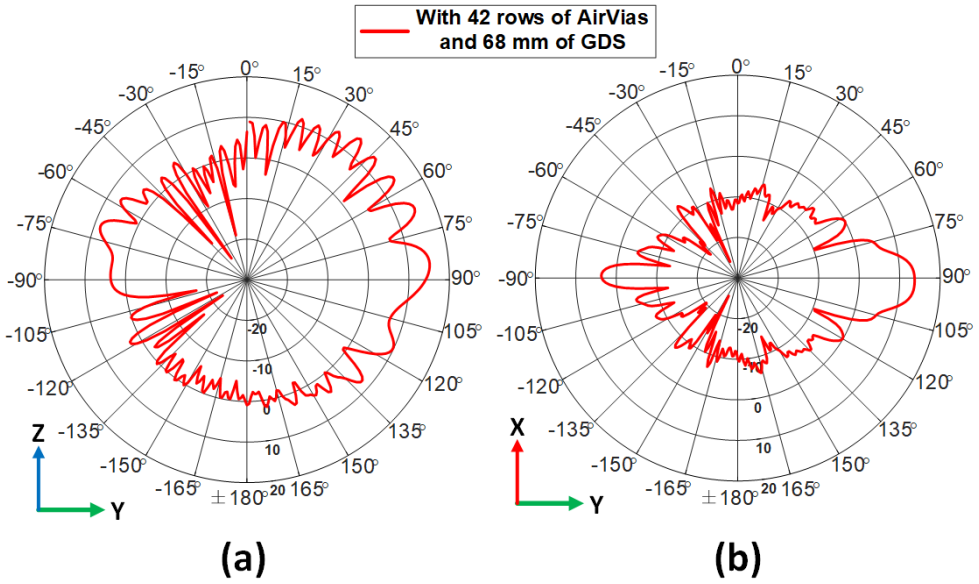

Figure 4.7: *Single-layer SWA simulations (42 rows of AVs and a GDS length of 68 mm or $24\lambda_g/4$): RG pattern in (a) the yz plane ($\phi = 90°$) and (b) the xy plane ($\theta = 90°$). The design was optimised (and compared against a variety of single-layer structure dimensions), however, a beam maximum directly at endfire with low SLLs was not achieved. This problem was overcome with the proposed two-layer SWA (see patterns in Figure 4.9).*

iterations of all possible structure features. This is a substantial loss in the radiated power for the SWA and when directive endfire radiation is required. Basically, the main beam position and the SLL should be improved upon to minimise (unwanted) radiation into undesired directions. This problem has been mitigated using the aforementioned dual-layer SWA topology, as further explored in the next section.

4.5.2 Operation of the Dual-layer Design

Following the previous studies of the single-layer SWA structure, the dual-layer design is now examined. Basically a distributed SW aperture is proposed to improve the SLL and correct the beam pointing position (which is now directly at endfire; i.e. $90°$). The structure is simply realised by two identical single-layer SWAs, but sharing a common ground plane. The allows for simple fabrication and low-cost assembly, in that the top and bottom layers (see Figures 4.1 and 4.2) can be made identical albeit a $180°$ phase shift between the distinct feeding ports. This differential feeding can be practically achieved with a conventional hybrid coupler, delay lines, and other related antenna feeding circuits.

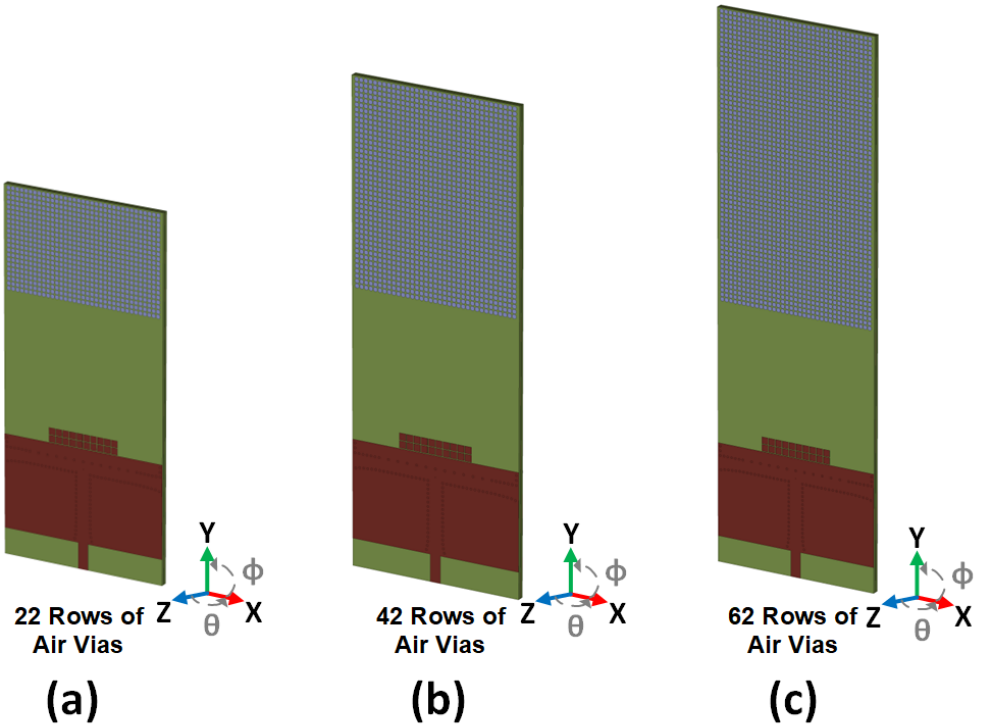

Figure 4.8: *Examined double-layer SWAs with a different number of rows for the AV section defining S_4: (a) 22, (b) 42, and (c) 62. All other dimensions as defined in Table 4.1.*

To further examine the travelling-wave performance for the proposed two-layer design, Figure 4.8 shows three simulated SWAs designs where the AV sections lengths are varied (22, 42, and 62 rows of AVs) and all with a common GDS length of 60 mm whilst keeping all other design features consistent (see Table 4.1). Figure 4.9 reports the simulated beam patterns in the yz- and xy-planes for the three SWAs and Table 4.5 compares the RG and the SLL.

As it can be observed, the SLL is significantly reduced when compared to the single-layer design and for a longer AV section. More specifically, the SLL improved to -7.5 dB for the structure with 22 rows of AVs in the yz plane ($\phi = 90°$), -8.7 dB with 42 rows of AVs, and -9.6 dB with 62 rows of AVs (see Table 4.5). This is because the SW radiating aperture is effectively longer making the main beam more directive while also lowering the SLL. This performance improvement is typical with travelling-wave structures. More importantly, in all cases, the beam points directly at endfire (when compared to the single-layer SWA). This distinctive change in the main beam position is related to the fact the distributive aperture effectively acts as like two distinct travelling-wave antennas, phased appropriately and with complimentary edge radiation. This makes the far-fields radiated by both the top and bottom SWA structures to constructively

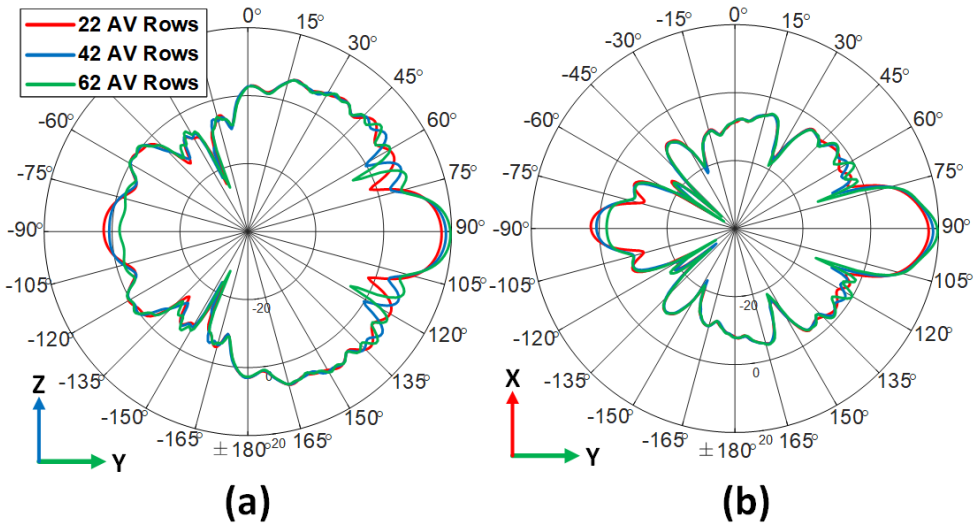

Figure 4.9: *Simulated RG in the (a) yz plane ($\phi = 90°$), and, (b) the xy plane ($\theta = 90°$) for the different number of AV rows (see Figure 4.8).*

Number of Air Via Rows	yz **plane** ($\phi = 90°$)		xy **plane** ($\theta = 90°$)	
	RG (dBi)	**SLL (dB)**	**RG (dBi)**	**SLL (dB)**
22 Rows	17.1	-7.5	17.1	-14.6
42 Rows	18.4	-8.7	18.4	-17.6
62 Rows	19.7	-9.6	19.7	-19.8

Table 4.5: *Double-Layer SWA Performance for Different Number of Rows for the AV Section*

add in the desired endfire region while also having a cancelling-effect for the sidelobes.

4.5.3 Comparison of the Single-Layer and Dual-Layer Designs

To further illustrate the radiation mechanisms for the two SWA structures, Figure 4.10 depicts the simulated electric field for 8 different antenna structures: without AVs and the SMS, without AVs and with the SMS, with AVs and without the SMS, and with rows of AVs and with the SMS. By this comparison, it can be observed that a mismatch in the fields is present without the SMS, causing unwanted back radiation and reducing the front-to-back ratio of the SWAs. Also, there is an unwanted change in the SW fields when the AV section is not present. Basically, it can be observed that the fields are more contained to the substrate (and at the end of the structure) when no AVs are present (see Figure 4.10, the double-layer SWA structures without AVs and with the SMS, and with AVs and with the SMS). This is important to ensure efficient

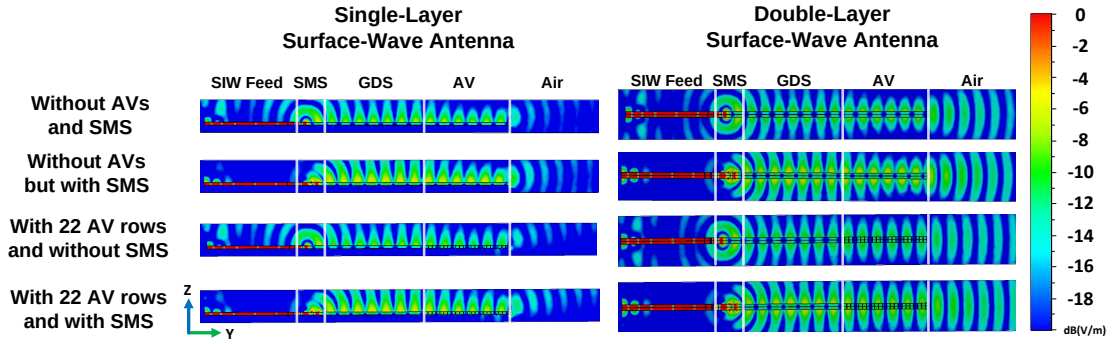

Figure 4.10: *Comparison of the single-layer and double-layer SWA for various cases. In particular, the electric field is shown for the longitudinal cross-section view within the structure and the air region (for the near-field, and in the yz plane): without the AVs and no SMS, without the AVs and with the SMS, with 22 rows of AVs and without the SMS, and, with 22 rows of AVs and with the SMS.*

radiation into the air region, as the motivation for the design process is to achieve a gradual transition or matching of the input power for radiation. It can also be noticed from Figure 4.10 that the main direction of the fields in the air region are radiated at angles above endfire for the single-layer SWA, and this is not observed for the dual-layer design.

To compare in more detail the single- and dual-layer SWAs, the structures have been analysed in terms of maximum RG, MLD, SLL, and efficiency for different number of rows for the AV section whilst adhering to all other dimensions as in Table 4.1. Figure 4.11 shows the simulated RG versus frequency, and as it can be observed the peak gain increases with a high number of AV rows, and also, with the two-layer structure. It is also interesting to note that the gain increases by about 3 dB for all cases when the single- and two-layers are compared.

Figure 4.12(a) also reports the simulated MLD versus frequency for the single and distributed aperture SWAs with 22, 42, and 62 rows of AV in the yz plane ($\phi = 90°$). It can be noticed that the MLD for the yz plane (ϕ cut) for the distributed structures is always $90°$ and for the frequency range of study; i.e. 17.5 GHz to 19 GHz. Figure 4.12(b) shows the improvement in the simulated SLL for the dual-layer design. For example, the SLL in the yz plane (ϕ cut) is enhanced by about 6 dB (or more) for most of the studied frequency range.

Figure 4.13 also compares the simulated radiation and total antenna efficiencies for the two SWAs, where the radiation and total efficiencies are about 90% or above. Here the radiation efficiency is defined as the ratio of input power that is converted into radiated electromagnetic waves. It accounts for losses in the antenna structure and feed system, where total efficiency

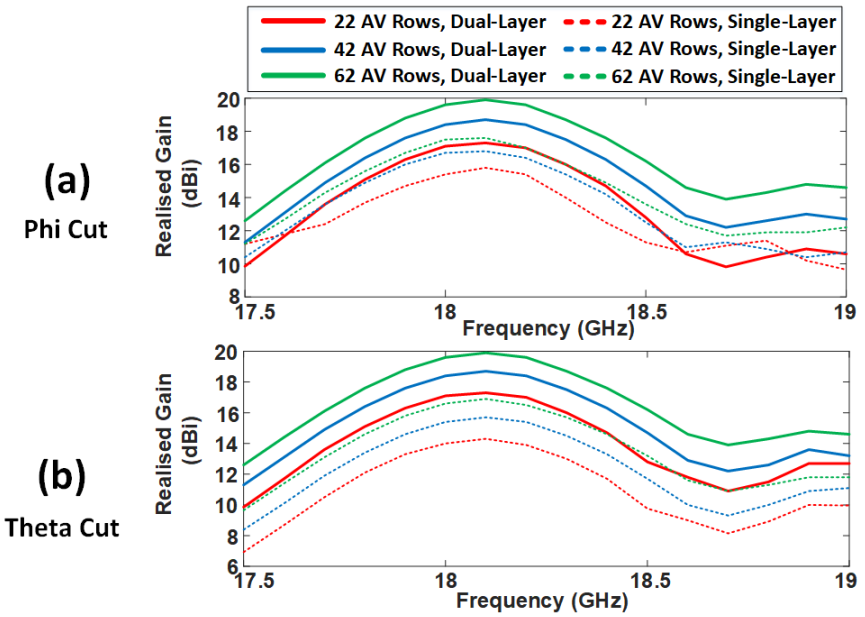

Figure 4.11: *Simulated maximum RG versus frequency for the single- and dual-layer SWA structures with 22, 42, and 62 rows for the AV section: (a) the yz plane ($\phi = 90°$) and (b) the xy plane ($\theta = 90°$).*

includes radiation efficiency as well as other losses, such as impedance mismatch losses and losses due to reflections from nearby objects. Total efficiency provides a comprehensive estimation of how effectively an antenna converts input power into radiated electromagnetic waves while considering all sources of loss. It is interesting that the efficiency can reach 95% at about 18 GHz for the two-layer design with 22 AV rows. This result is interesting and suggests antenna efficiency decreases slightly due to structure length, and thus efforts should be made to realise compact implementations while also keeping low SLLs and achieving maximum radiation directly at endfire. As discussed previously, this is possible by the two-layer SWA design, following the detailed design process of cascaded matching sections, and, utilising the SWA dimensions outlined in Table 4.1.

4.5.4 Feeding Considerations and Practical Implementation

Due to the required differential feeding of the dual-layer structure, practical connector placement is the next task in the design process. As reported in [110], the tapered microstrip line can be employed for the needed microstrip to SIW transition. This is important to enhance the matching from the 50-Ω microstrip line to the SIW input of the SWA and its T-junction feeding using LW principles. However, two distinct feed ports are required for the realised design (see

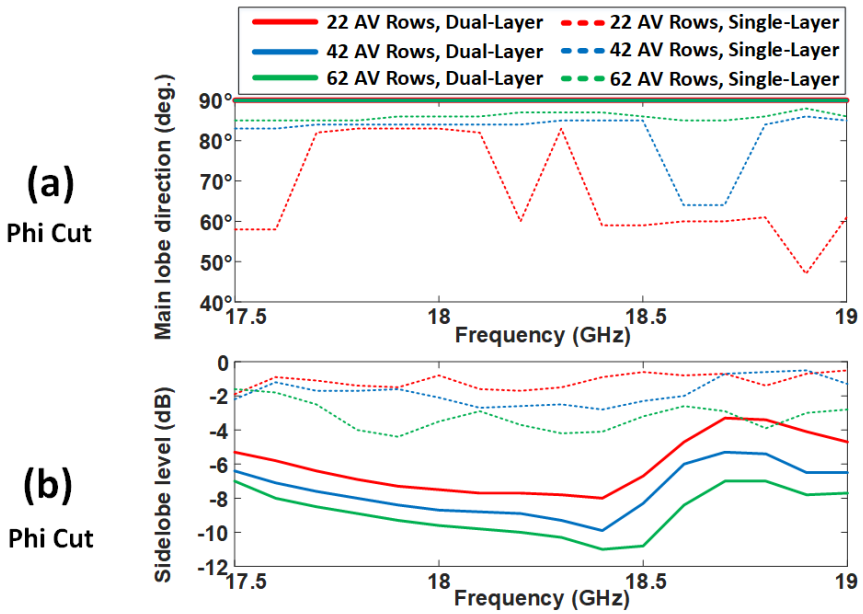

Figure 4.12: *(a): Simulated MLD versus frequency for single- and dual-layer SWA structures with 22, 42, and 62 rows for the AV section in the yz plane. (b): Sames as (a), but SLL.*

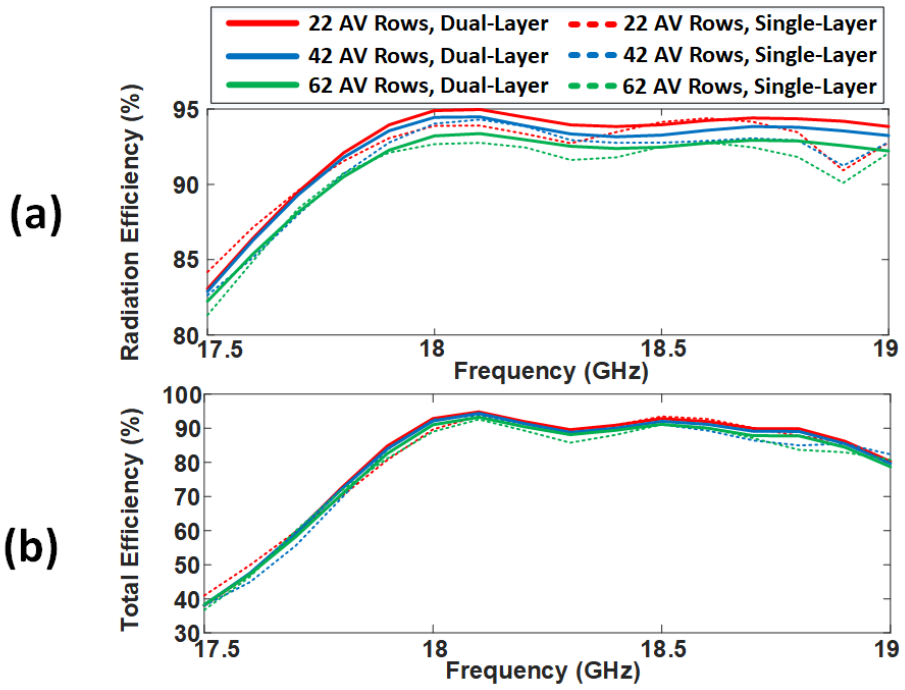

Figure 4.13: *Simulated efficiency: (a) radiation and (b) total antenna efficiency.*

Figures 4.14(a) and (b)). Basically, after designing the two-layer SWA as outlined in the previous sections, and, achieving directive radiation directly at endfire as shown in the simulations (see Figures 4.9 to 4.13), the next step is to design the practical two-port feeding arrangement for the SWA whilst making size considerations for the CubeSat standard.

Different microstrip feeding arrangements were initially considered (other than a standard end-launch connector positioning for the top and bottom layers as this would require co-located connector placement, which is not practical). In particular, they included different combinations of compact spline and 90° curved lines (see Appendix D.1 for more information). However, the full 90° microstrip line curve showed the best response when connectors (End Launch Super-SMA model 292-04A-6, by Southwest Microwave) were considered in the full-wave simulator and closely followed the previously studied results which employed a straight microstrip line feeder and a more ideal waveport excitation.

Regarding finalising the dimensions for SWA proof-of-concept whilst considering CubeSat size requirements, the T-Junction was made more compact in the Y-dimension when compared to the design in [110], and this shorted the length from about 267 mm to 255 mm. This was made possible by further optimising the T-junction feeder for compact implementation. Furthermore, the employed RF connector was taken into consideration at this design step, and after further optimisation in the full-wave simulator, a small transition was added between the RF connector and the two microstrip lines (More details about the impact of the RF connector on the beam pattern and reflection coefficient can be found in Appendix D.2). The length of this transition was 6.1 mm, and its width was 1.4 mm. Moreover, this needed transition extends the width of the structure in the X-axis to about 90 mm. Also, 42 AV rows were chosen for the fabricated design (see final design dimensions in Table 4.1), even though 62 rows would provide higher endfire gain and reduced SLL (see Figures 4.11 and 4.12(b), respectively). Basically, a 42 AV row structure was selected to ensure that the SWA can be suitable for 1U by 3U CubeSats, while also, ensuring high radiation efficiency and low SLL.

4.6 Experimental Validation & Discussions

This section will report on the final dual-layer SWA as well as its fabrication and measurement in terms of the practical PCB materials employed and external couplers for feeding (see Figure 4.14). A comparison and discussion of these findings is made. In addition, simulated and

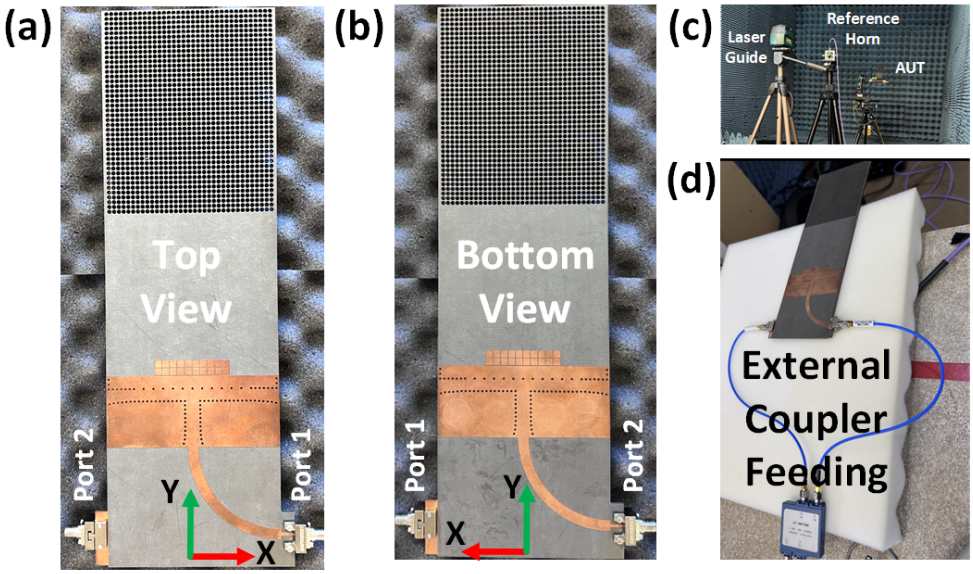

Figure 4.14: *Manufactured prototype: (a) top and (b) bottom views of the dual-layer SWA. Also shown in (c) is the far-field measurement setup, and (d) a photograph of the fabricated proof-of-concept structure with its external 180° coupler enabling differential feeding.*

measured data are in agreement.

As previously mentioned, the SWA being fabricated has 42 AV rows with a 68 mm length for the GDS region (all other dimensions for the optimised structure can be found in Table 4.1). The fabrication entailed manufacturing two identical antennas, and these were a fixed together using conductive epoxy (CW2400 from Chemtronics). This enabled the top and bottom layers to share a common ground plane, and alignment was made possible using a microscope. The substrate material used was Rogers RT5880 with a relative permittivity of $\epsilon_r = 2.2$ (rated) and a thickness of 1.575 mm. The employed end launch connector was SuperSMA 292-04A-6 from Southwest Microwave, while differential phase feeding for ports 1 and 2 were achieved using an external 180° hybrid coupler (KRYTAR 3, 4060265). Figure 4.14 shows the top and bottom views for the manufactured prototype. Moreover, this figure shows photos of the fabricated dual-layer SWA whilst being measured in the far-field.

The distributed aperture dual-layer SWA was measured in the calibrated anechoic chamber at Heriot-Watt University, Edinburgh Scotland. Results are reported in Figures 4.15 to 4.19. Generally, a reasonable agreement can be observed between the simulations and measurements. A minor frequency shift can be noticed for the reflection coefficient in Figure 4.15, which is likely related to possible manufacturing tolerances, including vias and AV drilling, metalliza-

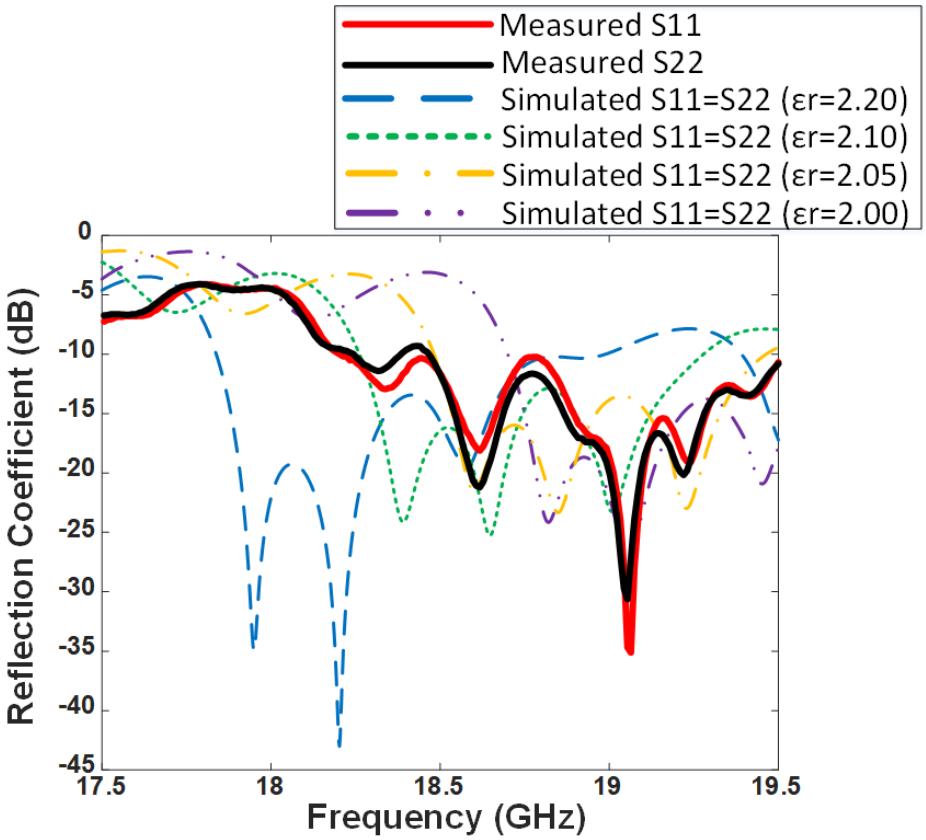

Figure 4.15: *Reflection coefficient versus frequency for the dual-layer SWA. It should be mentioned that simulations were initially completed considering ϵ_r = 2.2 (blue line), while the green, yellow, and purple lines consider a practical shift in the value of the relative dielectric constant and are within the tolerance for the PCB material. Similar findings were reported in [110]. Measurements also shown (red and black lines) for the top and bottom layers.*

tion, grounding, and practical variation of the relative dielectric constant for the substrate from the rated data sheet values (note: similar findings were reported in [110], [120], and [155]). To further understand this practical frequency shift for the PCB material, additional simulations were performed for different values of the relative permittivity. After this parametric investigation, findings suggest that a more representative permittivity is between $\epsilon_r = 2.1$ and $\epsilon_r = 2.05$ for the substrate at about 18 GHz instead of $\epsilon_r = 2.2$ as rated on the datasheet.

This frequency shift is also examined in Figure 4.16, where again there is a better agreement between the simulations for $\epsilon_r = 2.10$ and $\epsilon_r = 2.05$, as well as, the measured RGs versus frequency in the yz plane ($\phi = 90°$) and the xy plane ($\theta = 90°$). This notable frequency shift in $|S_{11}|$ and the RG are likely linked to possible anisotropy of the employed PCB material, where the relative dielectric constant in the vertical direction can be slighly different than the

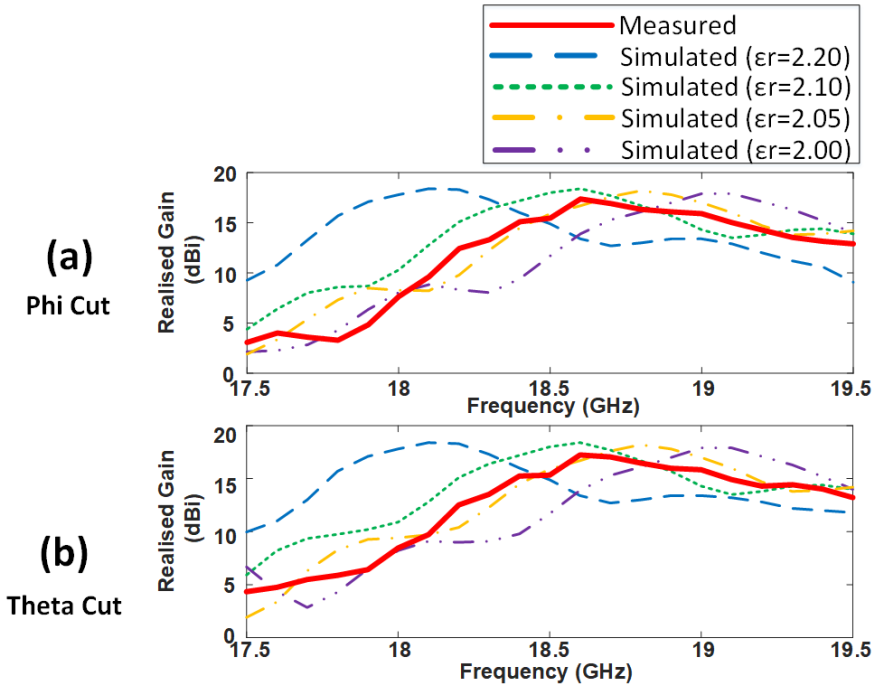

Figure 4.16: *Measured and simulated maximum RG versus frequency in: (a) the yz plane ($\phi = 90°$) and (b) the xy plane ($\theta = 90°$).*

horizontal direction at higher frequencies [135], [136], [137]. This anisotropy, which can be substantial for thick substrates, is a consequence of manufacturing and has some frequency dependence (see [135] pp. 758, Appendix A). As examined in [136], a better agreement between simulations and measurements can be observed after modifying the value for the dielectric constant. An analogous procedure was completed in [110], [155].

Simulation and measurement results for the far-field gain patterns are reported in Figures 4.17 and 4.18. The maximum measured RG is 17.5 dBi at 18.6 GHz in the yz plane ($\phi = 90°$) (see Figure 4.17) and this is because of the noted frequency shift from the original design frequency of 18 GHz. Also, this peak measured value of the gain is slightly reduced when compared to the simulated peak value of 17.7 dBi at 18.0 GHz. Moreover, the measured RG in the xy plane ($\theta = 90°$) is 17.5 dBi, whereas the simulated RG is 17.7 dBi. These minor reductions in gain are likely related to the noted practical change in the ϵ_r value. Regardless of these practicalities, a good agreement between the simulated and measured RG patterns can be observed.

Figure 4.19 also presents the measured beam patterns in the yz ($\phi = 90°$) and the xy planes ($\theta = 90°$) over a range of frequencies from 18.0 GHz up to 18.6 GHz. It can be seen that the pointing angles and SLLs are very similar through these investigated frequencies, and findings

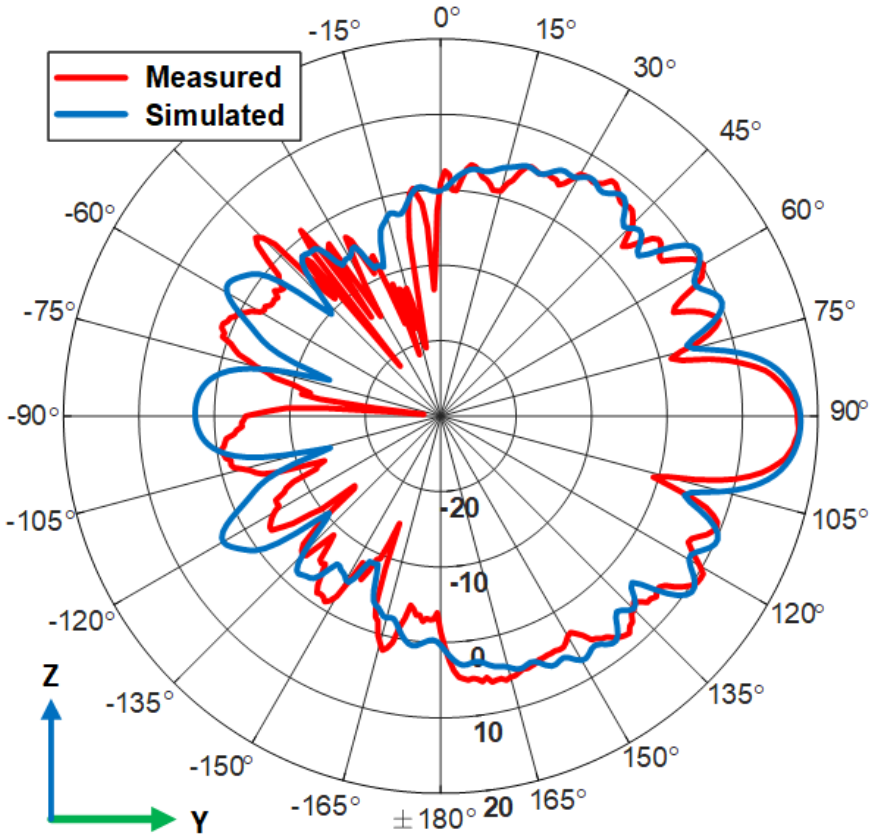

Figure 4.17: *Gain patterns in the yz plane ($\phi = 90°$). Results are 17.7 dBi and 17.5 dBi for the simulated and measured peak gain, respectively.*

are consistent with simulated data. In particular, the SLL is more than 7 dB below the main beam peak and the MLD is consistently at endfire demonstrating maximum radiation for the desired beam angle. In addition, cross-polarisation levels are well below 20 dB from the main beam maximum (all results not reported for brevity, and this is because the SWA is only defined by the PCB material thickness 1.575 mm). These cross-polarisation values are consistent with the earlier reported single-layer SWA design, which demonstrated quasi-endfire radiation only [110]. Additionally, the BW for this antenna is 5.0%, and this band limitation is attributed to the feeding system, which consists of a T-junction, as well as the matching techniques employed between the antenna sections. However, the BW is acceptable for more narrow-band applications, but can still support high data rates mainly due to the high carrier frequencies adopted. Figure 4.20 illustrates the CST mesh calculation for the proposed dual-layer SWA. It can be observed that the density of calculations increased between sections, such as between the GDS and air vias sections. Moreover, the highest density of calculations occurred in the AV section.

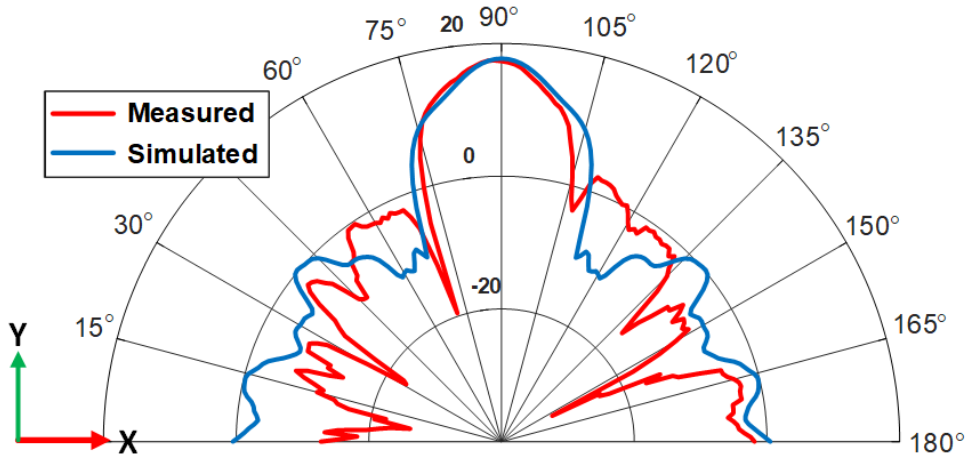

Figure 4.18: *Gain patterns in the xy plane ($\theta = 90°$). Results are 17.7 dBi and 17.4 dBi for the simulated and measured peak gain, respectively.*

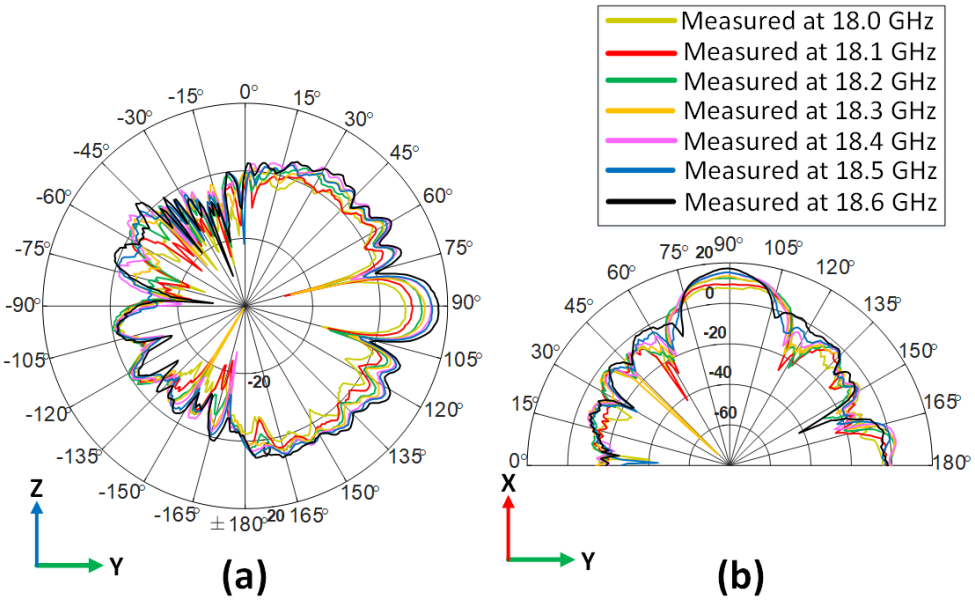

Figure 4.19: *Measured beam patterns for different frequencies from 18.0 to 18.6 GHz in the yz plane ($\phi = 90°$) and the xy plane ($\theta = 90°$).*

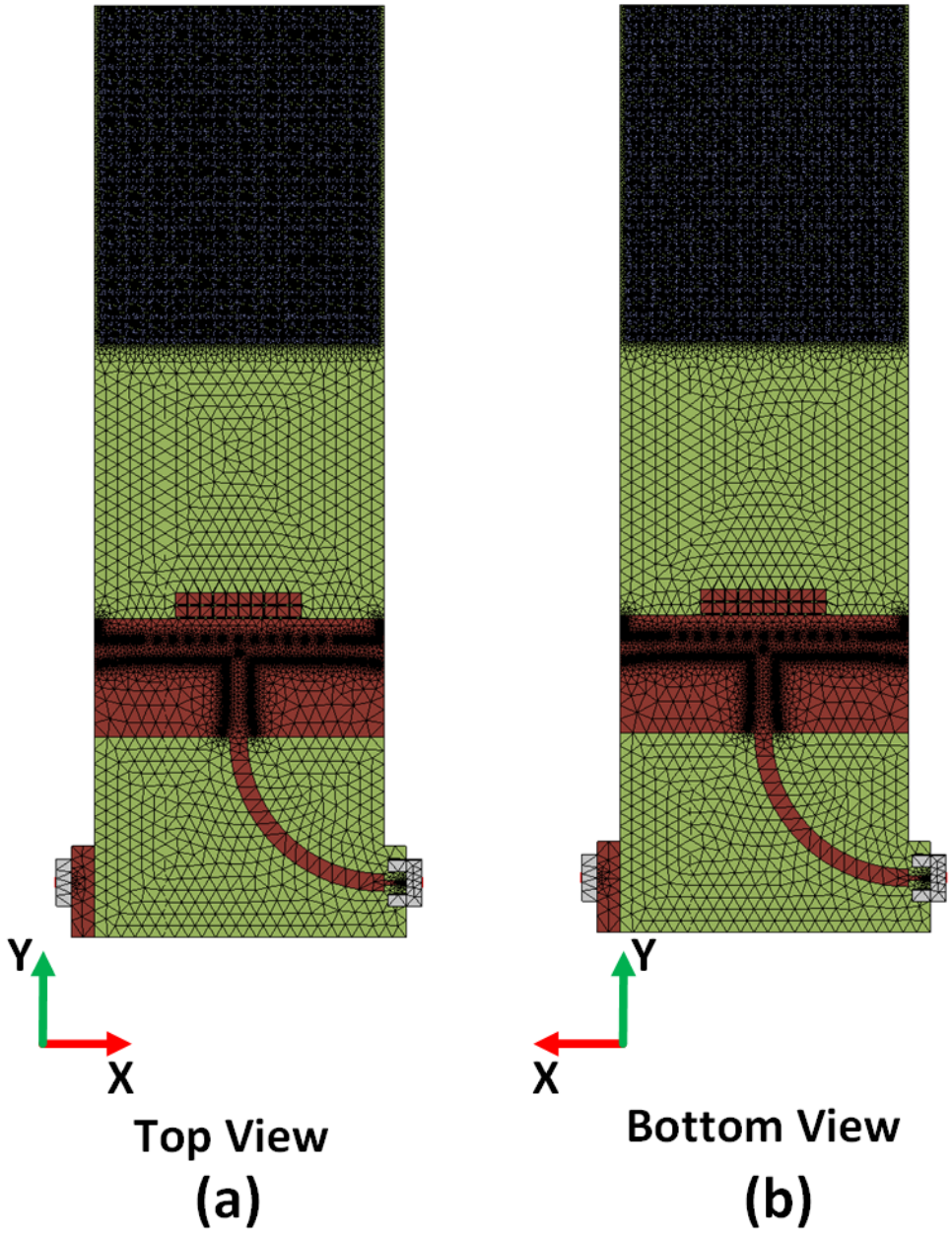

Figure 4.20: *Top and bottom views of the CST mesh calculation screenshot for the proposed dual-layer SWA structure.*

4.7 Summary

The experimentally validated SWA has been designed using SWs for radiation as well as LW principles and SIW technology for feeding. In particular, the developed two-layer distributed aperture SWA achieves edge radiation at structure truncation from the dominant TM_0 SW mode. This field configuration was efficiently excited by a leaky SIW T-junction feeder, which created a uniform and guided wavefront that propagated through the PPW section and is phase constant matched to the GDS and AV region by the compact matching section. This matching section was included, which is based on an array of printed sub-wavelength patches placed at the interface between the PPW and the GDS, and ensures a smooth transition and reduced structure reflections for the travelling-wave structure. The fabricated dual-layer SWA obtained a RG of more than 17 dBi, establishing also good agreement between the simulated and measured beam patterns. The dual-layer design offers low SLLs, high efficiency (which is more than 90%), and directive beam patterns, which are positioned directly at endfire.

Numerical modelling was provided by using the TRT as applied to an equivalent network, mainly to determine the operating frequency for the SWA whilst extracting the LW phase and attenuation constant, which defines the feeder. Basically, the different regions act as a load for the SIW feeder, and section lengths need to be taken into consideration when designing the SWA. In addition, an Appendix C is provided, which extends the modelling approach to higher millimetre-wave frequencies of operation. This demonstrates that the adopted numerical model can be useful when up-scaling the design.

In summary, the proposed K-band SWA can be suitable for CubeSats or other small satellite commercial missions, for example, Earth and planetary observations or inter-satellite links and where other low profile designs are required with directive radiation exactly at endfire. Moreover, the planar antenna was designed considering solar panel integration onto the antenna surface being positioned above and/or below the PCB. Also, the air hole via section makes the structure semi-transparent to optical frequencies enhancing solar power collection capabilities. Regarding manufacturing, the time and cost for fabrication of the PCB antennas can be roughly defined in terms of time units; i.e. the number of processes needed for SWA fabrication. For example, to make a purely SIW-based antenna, which is generally considered low cost, it is roughly defined into three steps: photolithography (metallic etching), hole drilling (defining air holes or AVs), and then hole plating to make metallised vias. The proposed SWAs only have metallised vias (and thus three steps) for the feed, and mainly only two steps for the majority

of the radiating part of the aperture. Future work can include further SWA optimisation and co-design with solar cells and CubeSat placement as well as further experimental testing to assess radiation and solar power harvesting performances. The next chapter expands upon this structure by reporting on a new design which does not include a ground plane. This improves the potential applications for solar panel integration.

Chapter 5
Optically Semi-Transparent Planar Endfire Antenna

5.1 Introduction

In Chapter 4, the focus was to achieve a competitive, truly endfire high-gain antenna for 3 CubeSat units. This was accomplished by introducing the air vias (AV) section and the distributed aperture principal describing the dual-layer structure. This antenna is fed by two leaky substrate integrated waveguide (SIW) T-junctions with a 180° phase shift between them. These T-junctions create a uniform wavefront that propagates via a truncated parallel-plate waveguide (PPW). A sub-wavelength matching section (SMS) is included between the PPW and the grounded dielectric slab (GDS) to facilitate a smooth transition for the phase constants and reduced reflections. Additionally, a grounded AV section with a fixed diameter was added to modify the relative permittivity and simplify the field transition from the GDS to the air region with endfire radiation.

In this chapter, the objective is to design a more compact endfire high-gain antenna with solar cell integration suitable for 1U CubeSats. To accomplish this, an ungrounded substrate with AV sections of different diameters is used, which gradually changes the permittivity for a smoother transition and minimises reflections to the air region while maintaining an endfire radiation pattern. Additionally, the design frequency for this structure is set at 24 GHz, differing from the previous chapters, where it was 18 GHz, aiming to shorten the wavelength and better align with the objectives of this chapter. This makes the 1U CubeSat structure more compact than the design reported in the previous chapter. To feed this ungrounded substrate with AV sections, a series of SIW horn arrays working in phase were adopted. This configuration can provide high data rate capabilities for downlink communications for CubeSats.

Moreover, CubeSats can benefit from combining antennas with solar cells, resulting in increased efficiency, reduced weight, and simplified design [5], [23], [24]. However, it is important to keep in mind that this technology is still relatively new and developing. While there

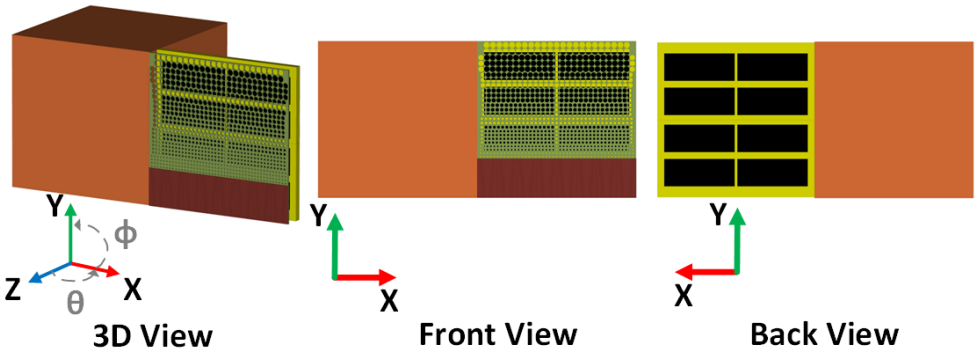

Figure 5.1: *Example of the possible placement for the proposed SWA array on a 1U CubeSat is depicted, showing 3D, front, and back views with the integration of solar cells underneath the AV section. Here the solar cell is shown to be deployable as in [150], but non-deployable configurations are also possible.*

are advantages to integrating solar cells with CubeSat antennas, there are also challenges to address, such as optimising antenna performance while maintaining solar cell efficiency and minimising potential blockages of the antenna inhibiting solar power collection. Regardless, this integration has great potential for future CubeSat missions, as it allows for more compact designs and opens up new possibilities for further integration with other sensor technologies to enhance mission capabilities. Figure 5.1 presents the possible placement for the proposed SWA array on a 1U CubeSat, and this type of deployable solar panel antenna integration setup has been tested in the Alba Orbital CubeSat mission; i.e. Unicorn-2 [150]. Next, Section 5.2 will illustrate the necessary background information relating to other antenna structures which employ AVs, while Section 5.3 further outlines the proposed SWA design.

5.2 Background Literature

The utilisation of drill holes in a PCB or AVs, which are basically air filled holes, have been exploited to control aperture fields in various works whilst designing antennas [156], [157]. The specific application and context may vary depending on factors such as the desired beam direction, frequency range, and performance characteristics. For example, in [156], efforts focused on a SIW horn antenna by realising a sparsely perforated dielectric slab. That design demonstrated a significant improvement in bandwidth (BW) when compared to a more conventional SIW horn, and operated from 16 to 24 GHz with an average gain of 9 dBi. In that work, the AVs in the perforated dielectric slabs enhanced the antenna performance across frequencies

by improving impedance matching and reducing sidelobes. In another work, [157], some AVs within a dielectric slab and in conjunction with an H-plane horn antenna, achieved a wide BW from 17.4 to 24 GHz whilst maintaining a compact form factor.

More recent studies on AV antennas have been reported in [154], [158] and [159]. For instance, [154] proposed a compact SIW horn antenna with partially detached broad walls and AV perforations. This design achieved a compact size and exhibited a BW performance ranging from 17.7 to 26.7 GHz, with a gain varying between 8 and 9 dBi. The inclusion of the AV perforations and partially detached broad walls leads to improved impedance matching and radiation, thereby enhancing the overall performance of the antenna. In another study, [158] presented a low-profile and wideband SIW horn antenna that is surface-mountable and contains AVs. This structure operates from 19.1 to 27.4 GHz, and this antenna achieved a wide BW. Furthermore, [159] introduced a novel and unique configuration of a SIW horn antenna without a broad wall. Instead, AVs were arranged in an intricate pattern. This design operated within a BW from 17.8 to 28.2 GHz and exhibited characteristics of higher than 5 dBi gain and directive patterns.

Two other studies, based on Luneburg lens antennas, also used AV units and were reported in [160] and [161]. More specifically, in [160], a novel planar-integrated Luneburg lens antenna exploited AVs and metamaterial inclusions. Broadband performance was achieved through the integration of the AV metamaterial inclusions at the edge of the SIW horn aperture. Moreover, to achieve good wave-focusing effects, the AV unit cells were designed and arranged in an array with equivalent gradient refractive indexes by changing the diameters. The design operated from 18 to 27 GHz with a gain ranging from 12.5 to 17 dBi. In [161] also, an innovative multibeam Luneburg lens antenna was proposed and defined by a unique triple-layer configuration for efficient beamforming and wide angle coverage. In that work, moreover, seven feed antennas were placed on the edge of the middle layer to perform multibeam radiation, achieving a peak gain of 18.2 dBi at 28 GHz.

The previous works in the literature primarily emphasised expanding BW rather than gain; it is notable that all the antennas achieved gains of 10 dBi or below, except for those referenced in [160] and [161], which achieved approximately 18 dBi. However, these two designs encountered issues related to the dimensions and stability of integrating the antenna with solar cells in a1U CubeSats. The primary objective here is to develop a compact, high-gain endfire antenna integrated with solar cells suitable for 1U CubeSats.

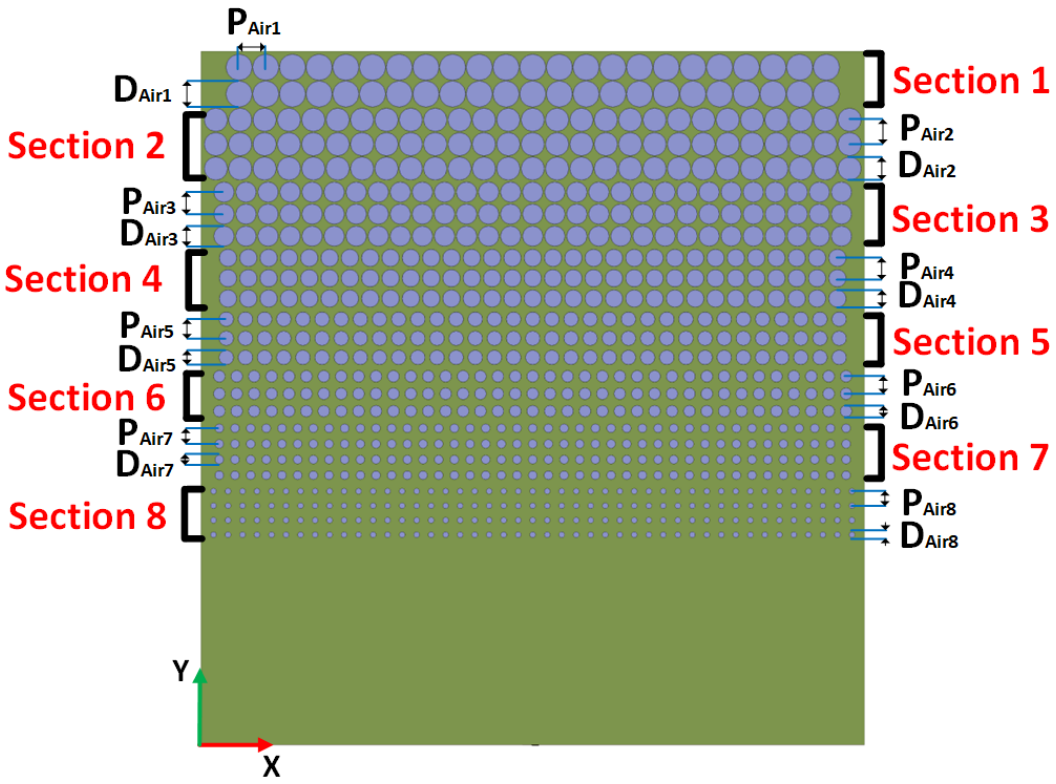

Figure 5.2: *Top view for the AV sections where the optimised dimensions and where different AV sections are outlined.*

5.3 Overview of the Proposed Design

In this chapter, the researcher proposes an endfire high-gain surface wave antenna (SWA) with an ungrounded substrate featuring AV sections of varying diameters, gradually changing the permittivity for a smooth transition of the guided-waves and reduced reflection in the air region. The advancement from the above mentioned previous structures [154] - [161] is that the proposed structure has been designed for the inclusion of solar cells underneath the SWA, following Chapter 4. Figure 5.1 presents the 3D, front, and back views for the possible placement of the proposed SWA on a 1U CubeSat, showing the solar cells integrated underneath the AV section. Figure 5.2 illustrates the top view for the antenna, displaying the eight AV sections, where the optimised dimensions and different AV sections are outlined (see Table 5.1).

Detailed simulations and numerical analysis examining the performance of the SWA array are reported in this chapter. An overview of the theoretical approach and the calculation for the effective relative dielectric constant, $\epsilon_{r_{eff}}$ and the diameters for the AVs are provided in Sec-

tion 5.4. Simulation results with the ideal feeding for the proposed SWA and a comparison between the structure with and without AVs and ground are reported in Section 5.5. Introduction of the practical feeding, which is a planar SIW horn arrangement, to the three different ungrounded substrates, is discussed and compared in Section 5.6. Section 5.7 will further discuss the simulation results and provide an analysis for the proposed SIW horn array feeding for this ungrounded substrate. Finally, Section 5.8 concludes this chapter and highlights some possible future work.

5.4 Approach to Designing the SWA

Firstly, it is essential to note that the variation in permittivity between a dielectric slab with and without a ground plane is mainly caused by changes in the electric field distribution due to the existence or absence of the ground [8], [87], [162]. The specific values of permittivity are determined by the material properties of the dielectric slab, thickness, and surrounding environment. In the case of a dielectric slab with a ground plane, the electric field distribution (TM_0 SW mode) generated by this slab is affected within the antenna system. The ground plane acts as a mirror image of the electric field (TM_0 SW mode) generated by the dielectric slab, altering the relative effective permittivity ($\epsilon_{r_{eff}}$). Essentially, the fundamental TM_0 mode on a dielectric slab with a ground is the same as the mode found on a dielectric slab with twice the thickness of an ungrounded slab [8], [87]. Consequently, the $\epsilon_{r_{eff}}$ of the ungrounded dielectric slab is typically higher than its relative permittivity for a grounded slab. This is illustrated in Figure 5.3 where a grounded and an ungrounded dielectric slab are compared, following [8], [87].

On the other hand, in the case of a dielectric slab without a ground plane, the electric field (TM_0) distribution remains unaffected by any reflective surfaces, such as a ground plane [8], [87], [162]. Consequently, the $\epsilon_{r_{eff}}$ of the dielectric slab stays close to its ϵ_r. Without the presence of a ground plane, the electric field propagates freely without significant interaction or alteration [87], [162]. Moreover, the dielectric constant defines the extent to which an electric field is immersed in the dielectric versus air region, and without a ground plane to control the electric field distribution, the ϵ_r becomes the dominant factor in determining the behaviour of electromagnetic waves passing through this dielectric slab [87], [162]. Also, the higher the ϵ_r, the more the fields will be confined to the dielectric slab region.

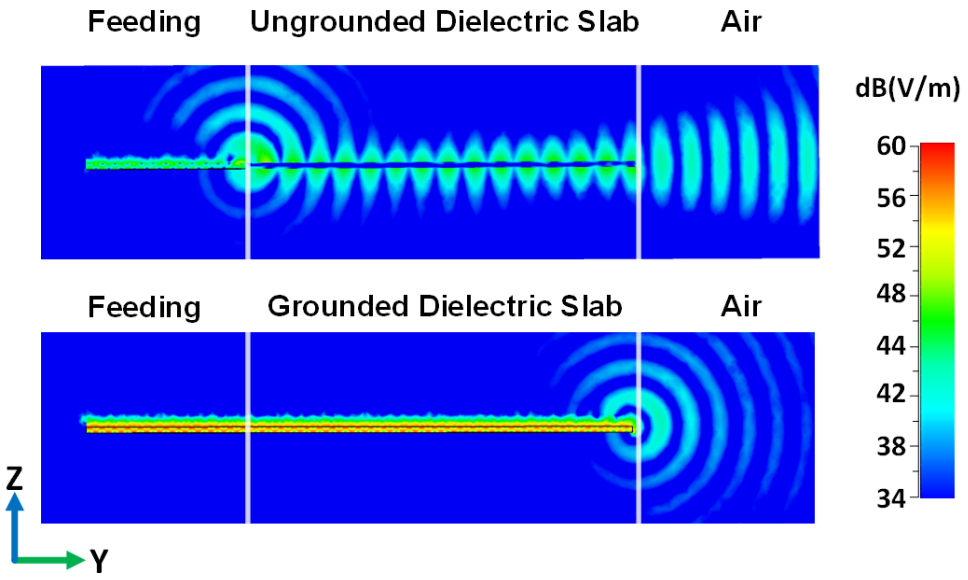

Figure 5.3: *Comparison of the ungrounded and grounded dielectric slab antenna structures. The electric field is shown for the longitudinal cross-section view within the structure and the air region (for the near-field, and in the yz plane). For the ungrounded case, the fields are clearly shown to be radiated in a more directive orientation at the end of the substrate, and this can lead to a more directive far-field beam pattern.*

Since the ϵ_r primarily controls the behaviour of SWs in a dielectric slab without a ground plane, this chapter introduces a novel concept of an ungrounded dielectric slab with AV sections (see Figure 5.2). The purpose is to guide the waves toward the edge of the structure, and this supports propagation to the end of the SWA, generating an endfire pattern in the far-field. In addition, the AV sections increase the vertical effective aperture of the antenna structure, and this increases pattern directivity. The ungrounded dielectric slab comprises eight sections, each with varying AV diameters, post-separation, and the number of AV rows. By incorporating these different sections, a gradual change in the $\epsilon_{r_{eff}}$ occurs, resulting in a smooth transition and minimal reflection from the feeding through the ungrounded dielectric slab to the air region. Section 5.4.1 will provide detailed calculations for determining the parameters of these AV sections.

5.4.1 Determination of the Effective Relative Dielectric Constant with the Air Via (AV) Sections

As has been briefly explained above, ϵ_r and the substrate thickness are the dominant factors controlling the behaviour of SWs in a dielectric slab without a ground plane. A ungrounded dielectric slab with eight AV sections is designed in this chapter (see Figure 5.2), and the $\epsilon_{r_{eff}}$

is calculated for each section using the equation provided in [154]:

$$\epsilon_{r_{eff}} = \frac{\epsilon_r \left(P_{Air}^2 - \pi \frac{D_{Air}^2}{4} \right) + \pi \frac{D_{Air}^2}{4}}{P_{Air}^2} \tag{5.1}$$

where P_{Air} represents the AVs post separation and D_{Air} is the diameter for the AVs. This equation helps to characterise the propagation of the fields in the endfire direction, leading to a gradual decrease in the $\epsilon_{r_{eff}}$ along the structure. Basically, with a larger AV diameter and more dense AVs, and further towards the end of the structure, the propagation constant approaches that of air; i.e. $\beta = k_0$. In the proposed design, the $\epsilon_{r_{eff}}$ for the structure varies from ϵ_r = 10.2 in the substrate without AVs to 3.3 in the last AV section before the air region. It is crucial that section lengths are about equal to a multiple of $\lambda_g/4$ to ensure gradual transition for the phase constants and minimised reflection, thus achieving the desired endfire pattern. Here λ_g ($= \epsilon_{r_{eff}} \lambda_0 = \frac{2\pi}{\beta}$) refers to the wavelength for the guided wave and is related to the phase propagation constant β.

Table 5.1 presents the parameter values for the proposed antenna, which comprises eight AV sections (see Figure 5.2). The diameters are set to range from 4.5 mm to 1 mm, while the post-separation varies from 4.6 mm to 2.5 mm. The $\epsilon_{r_{eff}}$ is gradually reduced in each section, starting from approximately 10.2 in the initial material and decreasing by 1 in every subsequent section until reaching 3.3 in the last section before the air region. This approach guides the SWs to be excited toward the end of the antenna design. The length of each section and the number of rows are determined based on the values of P_{Air} and D_{Air} to ensure that each section is approximately equal to a multiple of $\lambda_g/4$. This design choice aims to minimise any reflected power between sections and achieves a smooth transition for the phase constant and minimal reflections throughout the antenna structure, and follows the design approach also developed (and shown successful with a practical prototype) in the previous chapter.

Feeding the ungrounded dielectric slab with AV sections poses certain challenges. Therefore, the initial step in designing this proposed structure involves utilising ideal feeding, which entails employing a large waveguide port [163]. To achieve this, a GDS is incorporated into the ungrounded dielectric slab with AVs to facilitate the modeling of the ideal feeder and to assist in the optimisation of the overall structure. The simulation process using a commercial full-wave solver begins in Section 5.5, which outlines the starting point for the simulations. Additionally,

Diameter (mm)		Post Separation (mm)		Effective Permittivity		Section Length (mm)		Number of Rows
D_{Air1}	4.5	P_{Air1}	4.6	$\epsilon_{r_{eff1}}$	3.3	S_1	9.1	2
D_{Air2}	4.0	P_{Air2}	4.2	$\epsilon_{r_{eff2}}$	3.6	S_2	12.6	3
D_{Air3}	3.5	P_{Air3}	3.8	$\epsilon_{r_{eff3}}$	4.1	S_3	11.4	3
D_{Air4}	3.0	P_{Air4}	3.5	$\epsilon_{r_{eff4}}$	4.9	S_4	10.5	3
D_{Air5}	2.5	P_{Air5}	3.3	$\epsilon_{r_{eff5}}$	6.0	S_5	9.9	3
D_{Air6}	2.0	P_{Air6}	3.0	$\epsilon_{r_{eff6}}$	7.0	S_6	9.0	3
D_{Air7}	1.5	P_{Air7}	2.7	$\epsilon_{r_{eff7}}$	8.0	S_7	10.8	4
D_{Air8}	1.0	P_{Air8}	2.5	$\epsilon_{r_{eff8}}$	9.0	S_8	10.0	4

Table 5.1: *Parameters values for the proposed antenna with eight AV sections (see Figure 5.2).*

Section 5.5 explores and highlights the distinctions between the proposed design with AVs, the design without AVs, and a regular GDS configuration.

5.5 Ideal Feeding for the SWA

After calculating the parameters for the ungrounded dielectric slab with AV sections in the previous section and tuning the section length and number of rows, this section will proceed to the simulation stage. Feeding this antenna is not easy; thus, the simulation will commence with an ideal feeding approach, utilising a large waveguide port. This large waveguide port will be connected to a GDS to generate a uniform SW phase front to the ungrounded dielectric slab for endfire radiation [163]. Figure 5.4 illustrates the top and bottom views for the three structures with large waveguide ports: ungrounded dielectric slab with and without AVs, and without AVs but with a full ground plane.

Figures 5.5 and 5.6 present the far-field results for the three structures at 24 GHz in the 3D view and 1D cuts, which are the yz plane ($\phi = 90°$) and the xy plane ($\theta = 90°$). The achieved directivities are 21.3 dBi for the design with an ungrounded dielectric slab and AV sections, 20.5 dBi for the structure with an ungrounded dielectric slab but without AVs, and 16.1 dBi for the design with a full ground and without AVs. The proposed structure with an ungrounded dielectric slab and AV sections exhibits the best SLL in both cuts, which are -13.8 dB in the xy plane and -6 dB in the yz plane, compared to the other designs. The structure with an ungrounded dielectric slab but without AVs and the structure with a full ground have -10.9 dB and -8.2 dB SLL in the xy plane and -3.2 dB and -3.2 dB in the yz plane, respectively. These

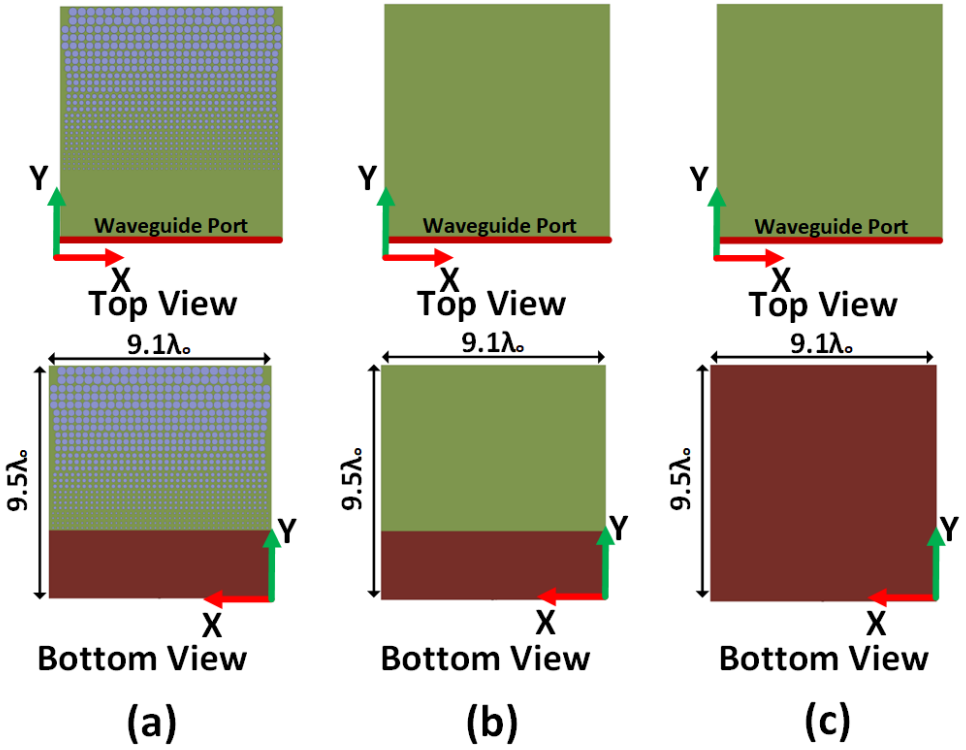

Figure 5.4: *Top and bottom views of the proposed antennas with large wave ports are shown: (a) with AV sections and a short GDS, (b) without AV sections and with a short GDS, and (c) without AV sections and with a full ground.*

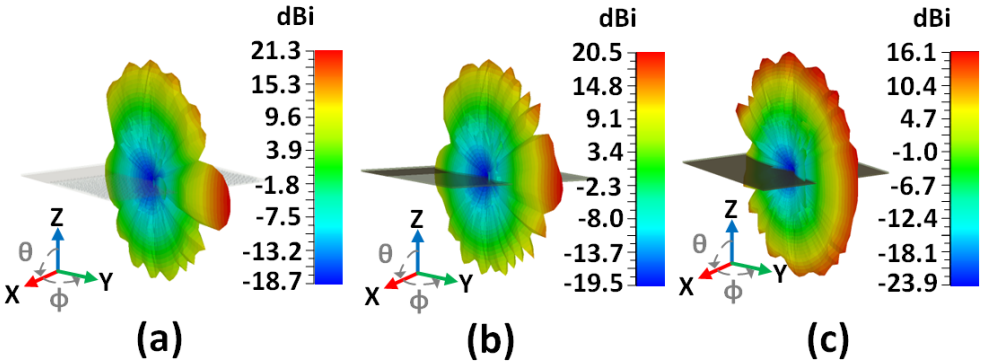

Figure 5.5: *Simulated 3D patterns for the proposed antennas with large wave ports are shown: (a) with the AV sections and a short GDS, (b) without AV sections and with a short GDS, and (c) without AV sections and with a full ground.*

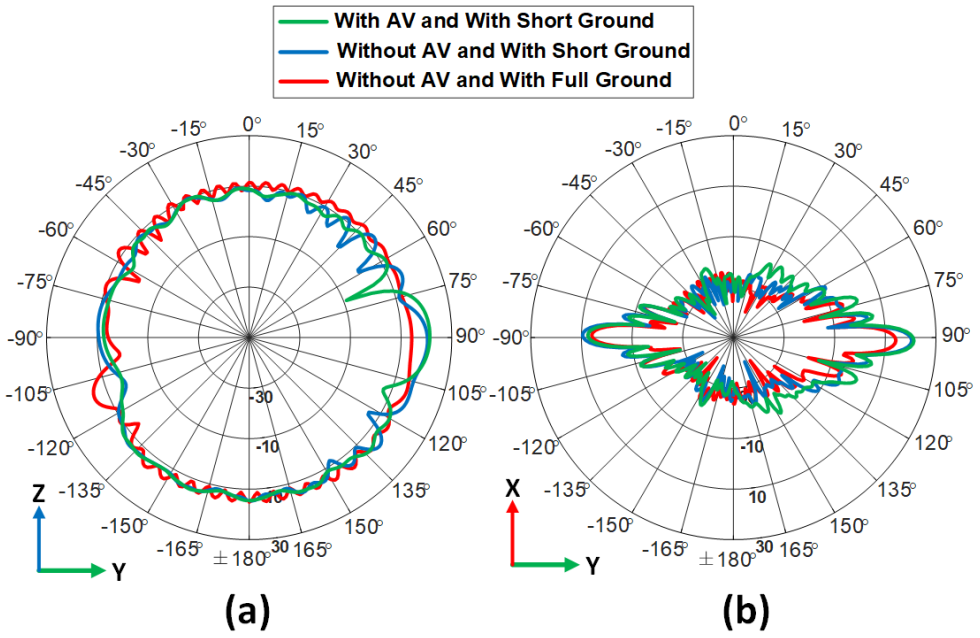

Figure 5.6: *Simulated beam pattern in (a) the yz plane ($\phi = 90°$) and (b) the xy plane ($\theta = 90°$) for the studied antennas with large wave ports.*

findings emphasise the importance of having the AV sections in the proposed structure and exciting the fields with an endfire direction. In particular, the directivity increases and the SLL generally decreases.

5.6 Practical Feeding Approaches For the SWA

This section further investigates a practical feed for the SWA, utilising a single SIW horn that will be attached to the ungrounded dielectric slab with the AV sections. The detailed design of this horn SIW feed is described in Section 5.6.1. the researcher proposes three different structures for the ungrounded dielectric slab with AV sections: straight rows (Design A), curved rows (Design B), and straight-curved rows (Design C) of AVs. Figure 5.7 illustrates these three proposed designs and presents the top and bottom views for each structure. These configurations are designed to manipulate the cylindrical field for radiation, which is generated by the SIW horn. Different structures were also initially examined, but these three configurations offered the best results and provided an interesting comparison. Sections 5.6.2 and 5.6.3 examine the far-field simulation results for Designs A and B at different frequencies, while Section 5.6.4 provides a comparison of the three designs in terms of far-field results.

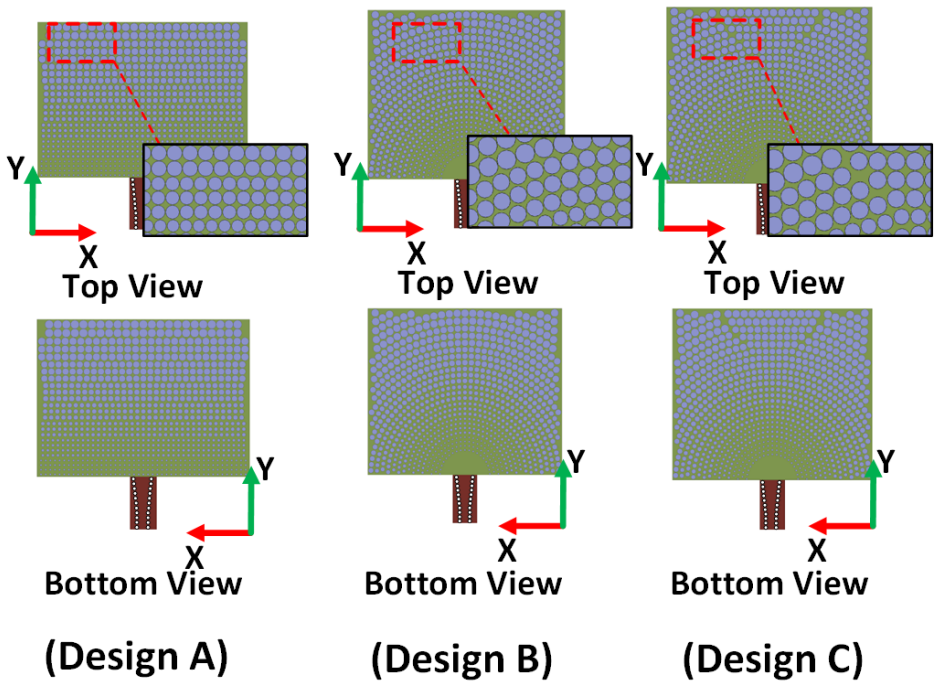

Figure 5.7: *Top and bottom views of the proposed antennas with a single SIW horn are shown: Design A: with straight rows of AV sections, Design B: with curved rows of AV sections, and Design C: with curved rows on the sides and straight rows in the middle of the AV sections.*

5.6.1 SIW Horn Feeding

This SIW horn feed has been used for various designs. It has been introduced as a planar horn antenna for the proposed structure, and as a type of surface wave launcher (SWL) by following [164]. This SIW horn from [164] exhibits a range of potential applications, for instance, feeding leaky wave antennas (LWAs) and SW-based designs. In [165], a width-modulated microstrip line LWA was reported using this SIW horn as a feeding point. The LWA system comprises a SIW horn and three rows of quasi-periodic width-modulated microstrip lines, which are identical to excite leaky wave (LW) fields. A fan beam pattern was obtained in the far-field, with a realised gain (RG) greater than 10 dBi. A third approach for this SIW horn was an end-to-end guide with a simple match technique to control the SWs in [166]. This design used a finite metasurface matching section based on a sub-wavelength array of patches to control and guide the SWs on the GDS. This matching section improved the transmission coefficient from -9 to -3.5 dB and the reflection coefficient from -6 to -12 dB at 23.7 GHz.

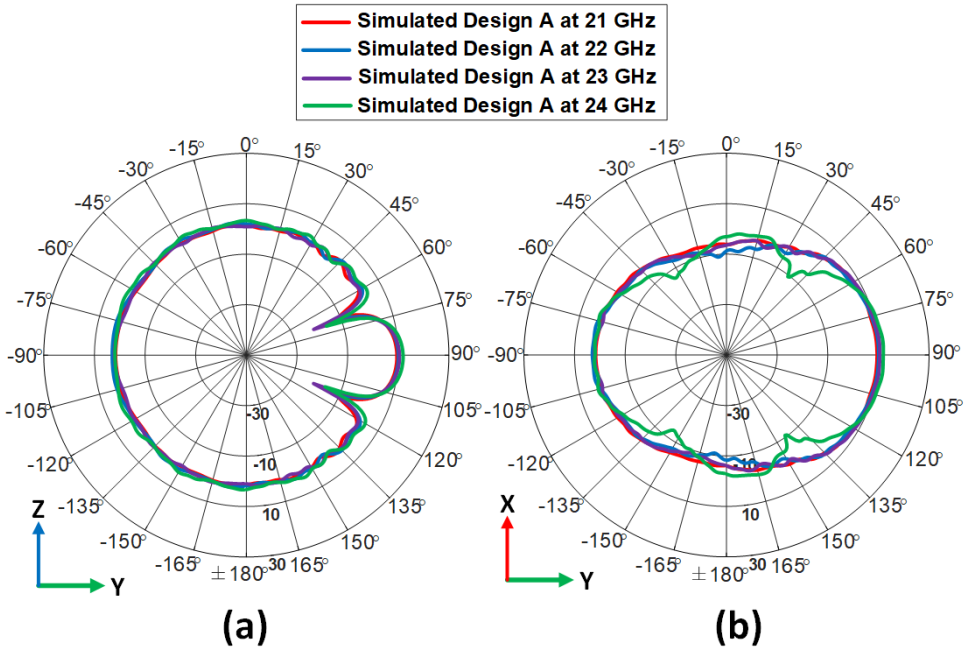

Figure 5.8: *Simulated beam pattern for different frequencies from 21 to 24 GHz in (a) the yz plane ($\phi = 90°$) and (b) the xy plane ($\theta = 90°$) for the proposed Design A antenna (see Figure 5.7).*

5.6.2 Design A

This section examines the simulated far-field results of the proposed Design A with a single SIW horn (see Figure 5.7). Figure 5.8 illustrates the simulated beam pattern for the proposed Design A antenna in the yz and xy planes for diverse frequencies from 21 to 24 GHz. The antenna achieves a truly endfire pattern, with a maximum directivity of 12 dBi at 24 GHz and a minimum directivity of 9.5 dBi at 21 GHz. In the yz plane ($\phi = 90°$), the SLL varies approximately from -7 to -8 dB, while in the xy plane ($\theta = 90°$), it ranges roughly between -5 to -10 dB. Generally, Figure 5.8 shows a good agreement in the beam pattern among the frequencies in the yz and xy planes.

5.6.3 Design B

In this section, the focus will be on the proposed structure Design B with a single SIW horn (see Figure 5.7) in terms of the far-field outcomes. Figure 5.9 illustrates the simulated beam pattern for frequencies from 21 to 24 GHz in the yz and xy planes for Design B. The directivity starts at 10.7 dBi at 21 GHz, increases to 11.3 dBi at 22 GHz, further rises to 11.5 dBi at 23 GHz, and

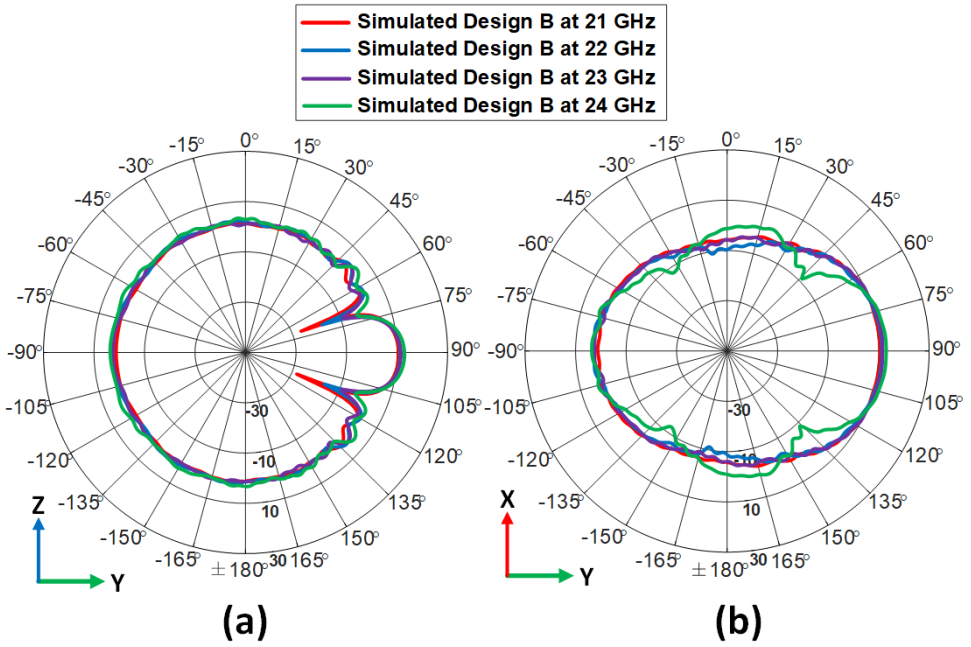

Figure 5.9: *Simulated beam pattern for different frequencies from 21 to 24 GHz in (a) the yz plane ($\phi = 90°$) and (b) the xy plane ($\theta = 90°$) for the proposed Design B antenna (see Figure 5.7).*

reaches 13 dBi at 24 GHz, with an endfire pattern. The SLL in the yz plane reaches around -8 dB while achieving almost -9.5 dB in the xy plane. Generally, Figure 5.9 demonstrates an acceptable agreement in the beam pattern among the frequencies in the yz ($\phi = 90°$) and xy ($\theta = 90°$) planes. A comparison between the three designs will be presented in the next section (Section 5.6.4) and will address the potential issues with the single SIW horn.

5.6.4 Comparison Between Designs A, B, and C

This section will examine in detail the far-field results for the three proposed structures: Design A, Design B, and Design C (see Figure 5.7). Figure 5.10 presents the simulated 3D beam pattern at 24 GHz for the three designs with the ungrounded AVs slab, while Figure 5.11 depicts the same simulated beam patterns in 1D cuts: the yz plane ($\phi = 90°$) and the xy plane ($\theta = 90°$). Both figures verify that the designs have similar beam patterns at 24 GHz, with minimal differences in directivity and SLL, approximately 1 dB and 0.6 dB, respectively.

Table 5.2 illustrates and evaluates the differences between the three proposed designs in terms of far-field results for four frequencies: 21, 22, 23, and 24 GHz, in the yz ($\phi = 90°$) and xy

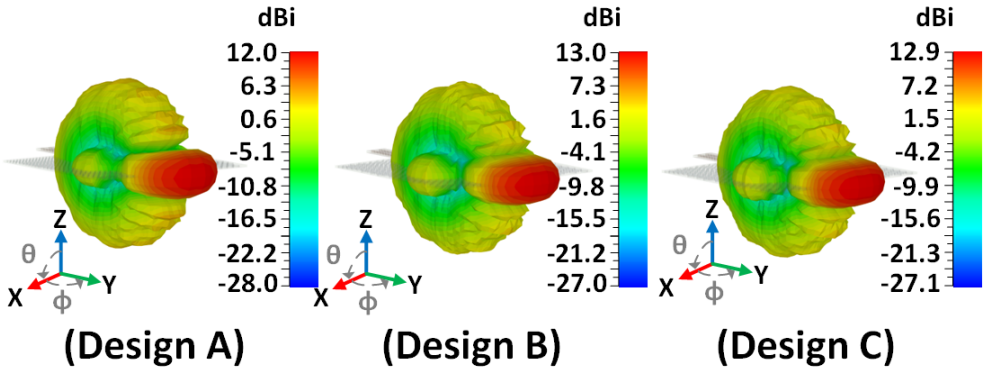

Figure 5.10: *Simulated 3D patterns at 24 GHz for the proposed antennas with a single SIW horn (see Figure 5.7) are shown: Design A: with straight rows of the AV sections, Design B: with curved rows of AV sections, and Design C: with curved rows on the sides and straight rows in the middle of AV sections.*

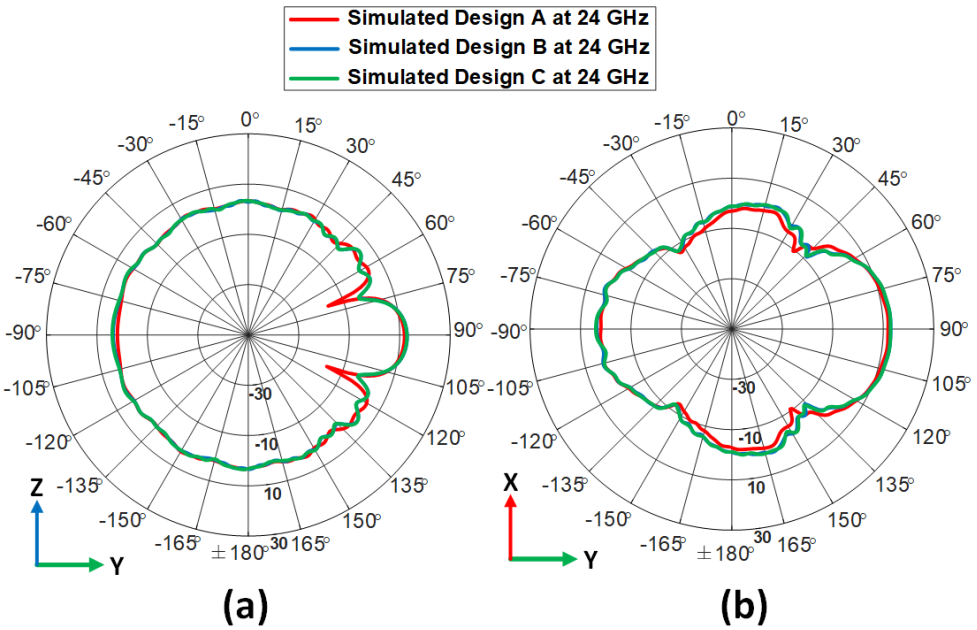

Figure 5.11: *Simulated beam pattern in (a) the yz plane ($\phi = 90°$) and (b) the xy plane ($\theta = 90°$) for the proposed antennas Designs A, B, and C with a single SIW horn at 24 GHz (see Figure 5.7).*

Design			Design A	Design B	Design C
21 GHz	yz **plane** ($\phi = 90°$)	**Directivity (dBi)**	9.5	10.7	10.6
		SLL (dB)	-6.9	-7.9	-7.7
	xy **plane** ($\theta = 90°$)	**Directivity (dBi)**	9.5	10.7	10.6
		SLL (dB)	-7.8	-8.6	-8.7
22 GHz	yz **plane** ($\phi = 90°$)	**Directivity (dBi)**	10.1	11.3	11.3
		SLL (dB)	-6.7	-7.2	-7.1
	xy **plane** ($\theta = 90°$)	**Directivity (dBi)**	10.1	11.3	11.3
		SLL (dB)	-5.0	-4.4	-4.5
23 GHz	yz **plane** ($\phi = 90°$)	**Directivity (dBi)**	10.5	11.5	11.5
		SLL (dB)	-7.9	-7.7	-7.5
	xy **plane** ($\theta = 90°$)	**Directivity (dBi)**	10.6	11.7	11.7
		SLL (dB)	-7.9	-5.9	-5.8
24 GHz	yz **plane** ($\phi = 90°$)	**Directivity (dBi)**	12.0	13.0	12.9
		SLL (dB)	-7.6	-7.8	-7.6
	xy **plane** ($\theta = 90°$)	**Directivity (dBi)**	12.0	13.0	12.9
		SLL (dB)	-9.6	-9.4	-9.0

Table 5.2: *Directivity and SLL for the three design structures (see Figure 5.7) in the yz plane ($\phi = 90°$) and the xy plane ($\theta = 90°$) for four frequencies: 21, 22, 23, and 24 GHz.*

($\theta = 90°$) cuts, in terms of directivity and SLL. Among the three designs, the best frequency response is observed at 24 GHz in terms of directivity and SLL. Moreover, the directivity for the three designs ranged from 9.5 to 13.0 dBi, and the SLL ranged from around -4.5 to -9.5 dB. Designs B and C exhibit slightly higher directivity than Design A, by about 0.5 to 1 dB. However, regarding the SLL, it can be observed that Design A is slightly better than Designs B and C, with a difference of approximately 0.8 dB. It can be noticed from Table 5.2 that the differences between the three structures are not significant, and to reduce complexity in the structure, Design A has been chosen for further study. To address the issue of other modes propagating from the SIW horn to the ungrounded dielectric slab, which is a common problem in these kinds of SWLs, Section 5.7 proposes an array structure with eight SIW horns to feed this ungrounded dielectric slab with straight AV rows.

5.7 SIW Horn Array Feeding

To mitigate the presence of other modes observed in the single SIW horn and other SIW horns, a series of eight SIW horn arrays were used to feed the ungrounded dielectric slab. As described in the previous section, Designs B and C, which feature curved and curved straight AVs rows,

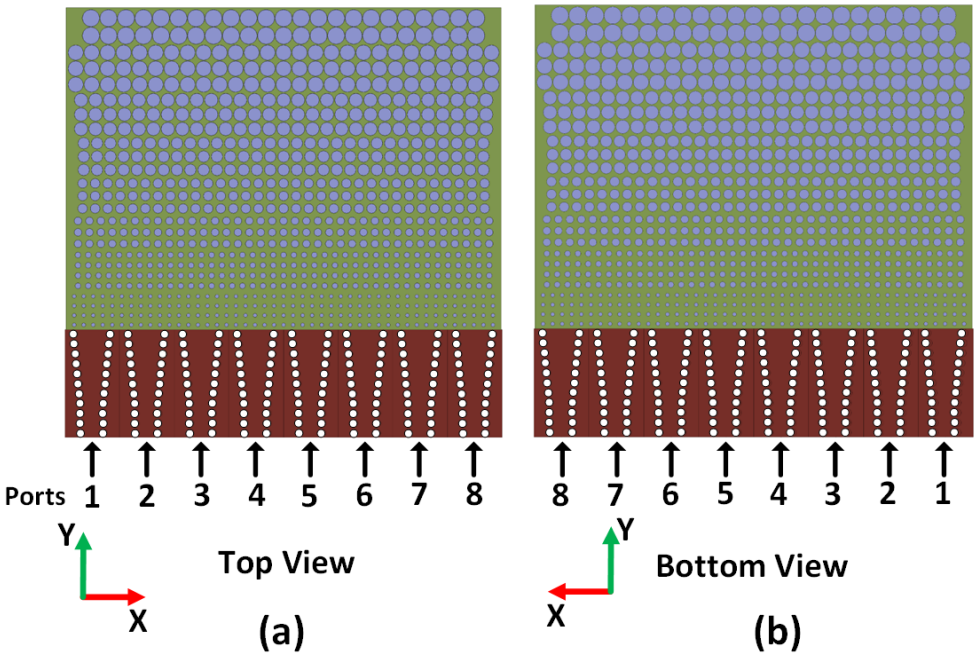

Figure 5.12: *(a) Top and (b) bottom views for the proposed antennas with an array of eight SIW horns with AV sections.*

respectively (see Figure 5.7), did not show significant differences, and this is related to the fact that AVs are sub-wavelength so the different configurations did not alter the antenna radiation responses significantly. This section will present the proposed design featuring straight AV rows of the ungrounded substrate with eight SIW horns. These SIW horns will work in the same phase to generate a uniform phase front SWs at the end of the structure, producing an endfire beam pattern in the far-field and this results with higher directivity and low SLL. Figure 5.12 shows the top and bottom views of the proposed endfire antenna with eight SIW horns and an ungrounded substrate with eight straight sections of AV rows. As previously stated, the $\epsilon_{r_{eff}}$ steadily decreases from 10.2 in the SWLs to 3.3 before reaching the air region for a smooth transition and low reflections.

Regarding far-field results, Figure 5.13 illustrates the simulated beam pattern for the proposed design with a dense SIW horn array for a range of frequencies from 21 to 24 GHz in the yz plane ($\phi = 90°$) and the xy plane ($\theta = 90°$). In general, the response exhibits good pattern agreement among the frequencies in both planes. The directivity increases from 18.6 dBi at 21 GHz to a maximum of 21.3 dBi at 24 GHz. At 22 and 23 GHz, the directivity ranges between approximately 19.4 and 19.8 dBi, respectively. It can be seen that the directivity significantly

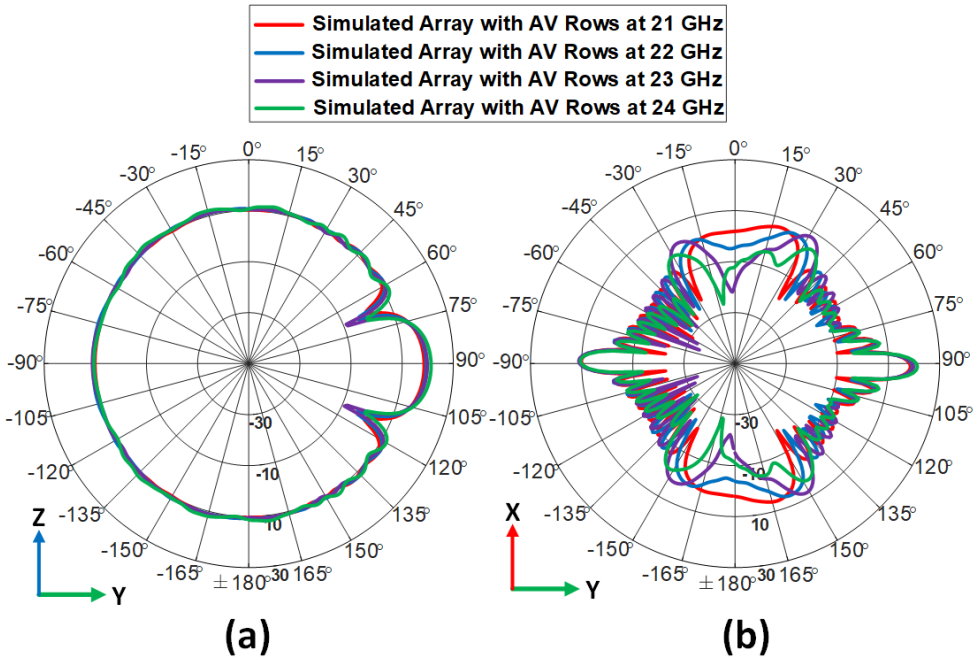

Figure 5.13: *Simulated beam pattern for different frequencies from 21 to 24 GHz in (a) the yz plane ($\phi = 90°$) and (b) the xy plane ($\theta = 90°$) for the proposed antenna with an array of eight SIW horns with AV sections.*

increases compared to the single SIW horn with Designs A, B, and C (see Figure 5.7), as explained in the previous section. Compared to the single design, the SLL was enhanced by around 2 dB in both planes, the yz and the xy. The SLL varies from -7 to -9.2 dB in the ϕ cut, whereas in the θ cut, the SLL goes from -8.5 to -10.8 dB.

Figures 5.14 and 5.15 show the simulated beam pattern for the proposed structure with SIW horns arrays with ungrounded substrate with and without AV rows at 24 GHz. These figures demonstrate that the design with AV sections reduces reflections and achieves a smoother transition for the fields, resulting in the generation of an endfire far-field pattern. The directivity decreases from 21.3 dBi in the design with AVs to 20.2 dBi in the design without AVs. The SLL exhibits a significant improvement in the yz plane ($\phi = 90°$), decreasing from -4.7 dB in the design without AVs to -9.2 dB in the structure with AVs rows. Moreover, in the xy plane ($\theta = 90°$), both designs exhibit nearly the same response with an SLL of approximately -11 dB. Naturally, it can be seen that the proposed design with ungrounded substrate and AV rows achieves the same directivity and better SLL in the yz plane compared to the first proposed structure with the ideal feeding using a large waveguide port (see Figures 5.4 (a), 5.5 (a), and 5.6).

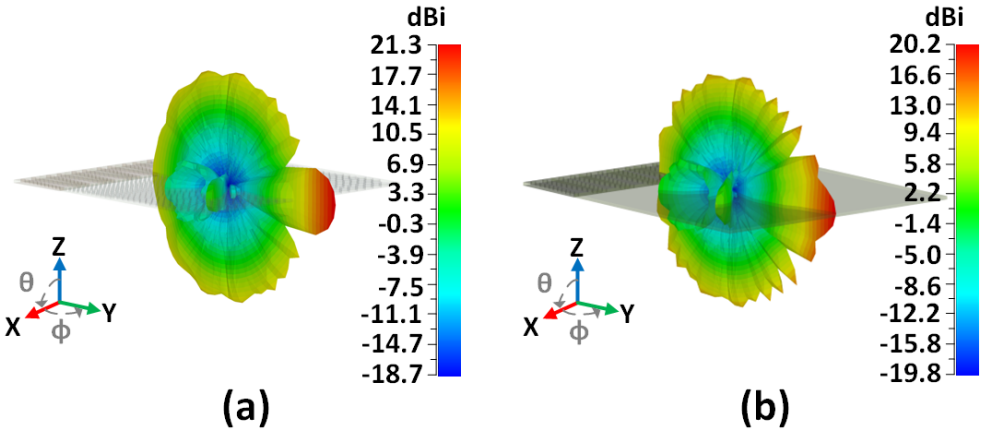

Figure 5.14: *Simulated 3D patterns for the proposed antennas with an array of eight SIW horns: (a) with AV sections, (b) without AV sections.*

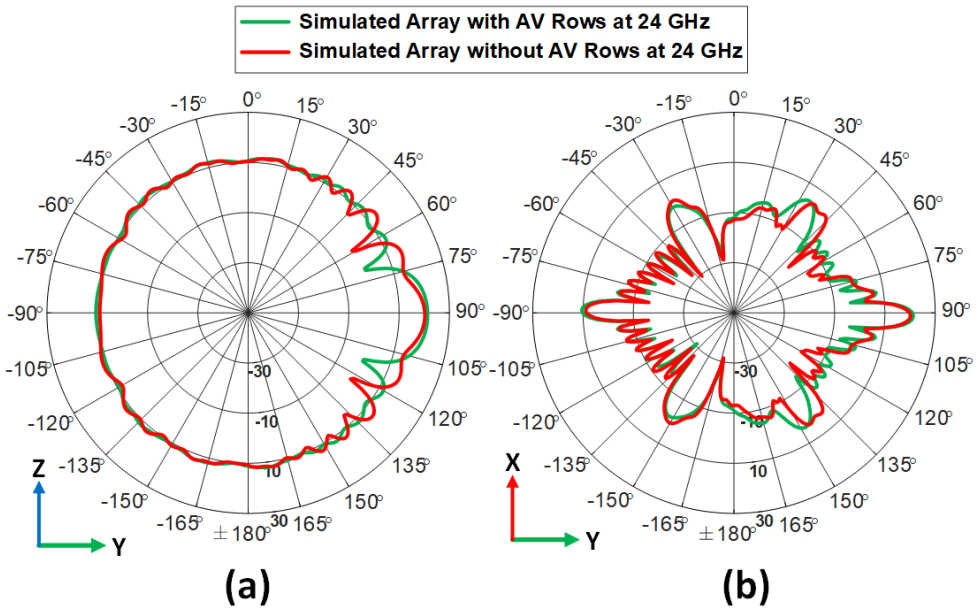

Figure 5.15: *Simulated beam pattern in (a) the yz plane ($\phi = 90°$) and (b) the xy plane ($\theta = 90°$) for the proposed antenna with an array of eight SIW horns at 24 GHz with and without AV sections. In the yz plane, the SLL are at -9.2 dB and -4.7 dB for the structures with and without AV sections, respectively. Additionally, in the xy plane, the SLL for both structures is -11 dB.*

Design	24 GHz			
	yz **plane** ($\phi = 90°$)		xy **plane** ($\theta = 90°$)	
	Directivity (dBi)	**SLL (dB)**	**Directivity (dBi)**	**SLL (dB)**
Large waveguide port Design A (see Figure 5.4 (a))	21.3	-6.0	21.3	-13.8
Single SIW horn Design A (see Figure 5.7)	12.0	-7.6	12.0	-9.6
Single SIW horn Design B (see Figure 5.7)	13.0	-7.8	13.0	-9.4
Single SIW horn Design C (see Figure 5.7)	12.9	-7.6	12.9	-9.0
Array SIW horn Desgin A (see Figure 5.12)	21.3	-9.2	21.3	-11.0

Table 5.3: *Directivity and SLL for the designs structures with single and array SIW horn in the yz plane ($\phi = 90°$) and the xy plane ($\theta = 90°$) for the wanted frequency 24 GHz.*

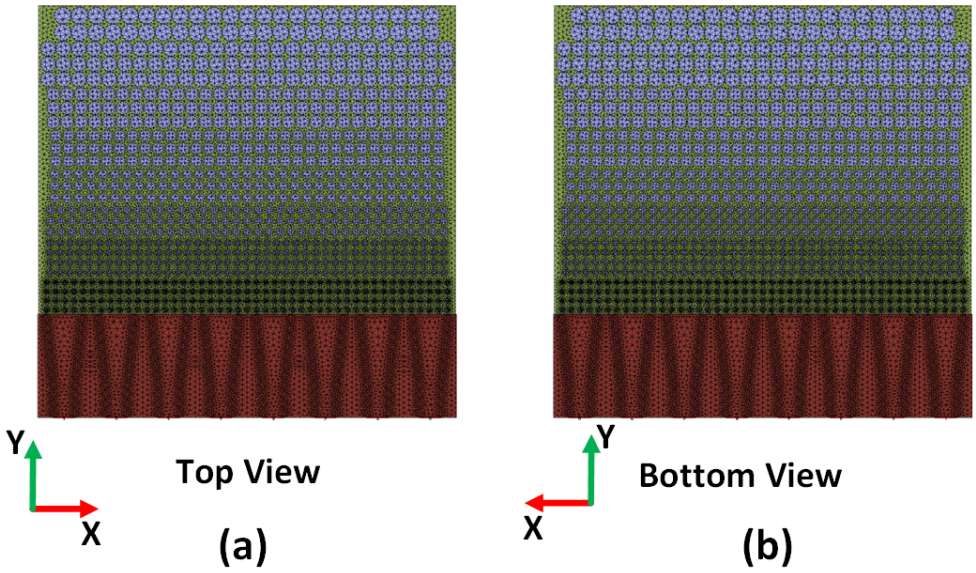

Figure 5.16: *Top and bottom views of the CST mesh calculation screenshot for the proposed semi-transparent SWA structure.*

Table 5.3 provides a comprehensive overview of different proposed antenna designs that had been presented through the chapter at a frequency of 24 GHz, focusing on their directivity and SLL characteristics in both the yz plane ($\phi = 90°$) and the xy plane ($\theta = 90°$). The designs consist of different variations that feature large waveguide port feeding (with Design A using AV rows (see Figure 5.4 (a))), single SIW horn feeding (with Designs A, B, and C using AV rows (see Figure 5.7)), and an array of SIW horns feeding (with Design A using AV rows (see Figure 5.12)). Generally, it can be noticed that the single SIW horn designs yield lower directivity values yet provides reasonable SLL. This table shows that the large waveguide port and the array of SIW horns (Design A) exhibit the highest directivity values of 21.3 dBi. However, the large waveguide port experiences relatively higher SLL by 3 dB in the xy plane but lower by 3.2 dB in the yz plane compared to the array of SIW horn. Therefore, it is clear that the SIW horn array design is an improvement compared to the other examined structures. Figure 5.16 displays the CST mesh calculation for the proposed SWA. It is evident that the density of calculations increased in sections with smaller air vias diameters and decreased as the diameter increased.

5.8 Summary

In this chapter, a planar optically semi-transparent endfire antenna operating at 24 GHz has been presented. The design of the antenna is based on SIW technology, utilising efficient methods for exciting the TM_0 SW mode. By employing an ungrounded dielectric slab with eight AV sections, the endfire beam pattern has been achieved, ensuring smooth transitions and minimal reflection in the air region. The process of feeding for this antenna involves multiple steps, ranging from the theoretical ideal feeding to the practical implementation with both single SIW horns as well as an array of SIW horns. In this chapter, three designs (Design A, B, and C) with distinct feature arrangements for the AVs have been proposed for the ungrounded dielectric slab.

The ungrounded dielectric slab has been fed by eight SIW horns, for the final SWA, which resulted in a directivity of 21.3 dBi and a SLL of -9.2 dB in the yz plane, with the xy plane reaching -11 dB. Additionally, all designs were compared based on their directivity and SLL to highlight this successful design. Furthermore, to the researcher's knowledge, no similar design has been examined previously. Future work involves creating a microstrip line for the SIW horns and implementing a feeding network for this array. The researcher also intends to

manufacture the SWA and compare its actual performance with the simulation results.

Chapter 6
Conclusion and Future Work

6.1 Conclusions

This thesis introduced innovative surface wave antennas (SWAs) specifically designed for CubeSat and other small satellites. These antennas were engineered using concepts such as substrate-integrated waveguide (SIW) technology, surface waves (SWs), and leaky wave (LW) principles. The resulting antennas exhibited both quasi and full endfire beam patterns, providing a simple approach for solar cell integration alongside high-gain performance. These configurations represent a significant advancement in the field of non-deployable CubeSat antennas by enabling integration with the solar panel aperture while offering high gain and endfire radiation capabilities, particularly at higher frequencies. The designs were supported by thorough theoretical analysis, comprehensive full-wave simulations, and experimental measurements to validate the SWA structures.

A comprehensive review of the literature and theoretical background was presented, exploring the research landscape in the domain of small satellite antennas. Critical parameters such as gains, sizes, and various antenna types were examined, along with the challenges inherent in antenna design. These challenges include achieving high gain, expanding bandwidth (BW), ensuring multiband capability, managing size and mass considerations, and achieving circular polarization. These obstacles underscore the limitations in designing antennas for such applications. Moreover, important theoretical background information necessary for understanding the developed designs was reviewed. This includes concepts like SIW technology and leaky and surface-wave theories, which form the foundation of the antenna systems and set the presented limitations. Additionally, complex theories such as the behaviour of SWs and LWs on planar guiding surfaces are introduced, alongside the discussion of the transverse resonance technique (TRT) applied to a grounded dielectric slab (GDS).

Table 6.1 presents a comparison of the three proposed designs with state-of-the-art endfire SWAs. The table evaluates CubeSat unit size, operational frequency, maximum gain, solar panel integration, and beam pattern position. The proposed antennas demonstrated in this thesis

Ref.	Size	Frequency (GHz)	Peak Gain (dBi)	Solar Panel Compatibility	Beam Position
[145]	2U	22.0	17.0	No	Quasi-endfire (83°)
[146]	3U	11.6	15.3	No	Quasi-endfire (72°)
[147]	9U	9.0	19.1	No	Quasi-endfire (70°)
[148]	10U	4.7	13.3	No	Quasi-endfire (77°)
[149]	1U	12.0	9.0	No	Quasi-endfire (60°)
[150]	1U	2.4	5.0	Yes	Full-endfire (90°)
[167]	28U	5.0	10.2 (directivity)	No	Full-endfire (90°)
[168]	4U	11.4	19.8	No	Full-endfire (90°)
Design 1 (Chapter 3)	1U	18.0	12.1	No	Quasi-endfire (70°)
Design 2 (Chapter 4)	3U	18.0	17.5	Yes	Full-endfire (90°)
Design 3 (Chapter 5)	1U	24.0	21.3 (directivity)	Yes	Full-endfire (90°)

Table 6.1: *Endfire Surface Wave Antennas Comparisons*

offer competitive size, operate at high frequencies, and achieve competitive gains, with solar cells integrated via the AV section in Designs 2 and 3. Notably, Designs 1 and 3 (reported in Chapters 3 and 5) are compatible with 1U CubeSats, similar to the antennas in [149] and [150], but they operate at lower frequencies and offer lower gains. In contrast, other designs in the table target larger sizes. Design 2, newly reported in Chapter 4, stands out for its comparatively high gain, smaller size, and solar cell integration feature compared to other SWAs in the table. Regarding beam position, which is a challenge for SWAs, Designs 2 and 3 achieve full endfire radiation, a feat matched only by three other structures in the table: [150], [167], and [168]. Next, Section 6.2 will describe the key contributions of this research, while Section 6.3 will outline future directions.

6.2 Key Contributions

This section briefly summarises the novelty of the work in terms of the three main contributions achieved:

- Design, fabrication and measurement of a planar quasi-endfire SWA for operation at K-band utilising SIW technology. This antenna is tailored for CubeSat and other small satellite commercial missions, such as Earth and planetary observations or intersatel-

lite links. This antenna provides high data rate capabilities for downlink communications. The fabricated SWA demonstrated a realised gain (RG) of 13.3 dBi at 18.6 GHz, exhibiting excellent agreement between simulated and measured beam patterns, with a simulated total radiation efficiency of 93.4%. Additionally, determining the normalised LW phase and attenuation constants by using results from CST and the Bloch analysis method. Furthermore, the TRT was applied to the TEN circuit model to also extract LW alpha and beta values.

- Design, fabrication, and measurement of a truly endfire high-gain antenna tailored for 3U CubeSats. This advancement involved introducing an AV section, describing a new dual-layer structure through the distributed aperture principle, and employing TEN methodologies. Basically the antenna is fed by two leaky SIW T-junctions with a 180° phase shift between them. To further optimise the endfire SWA, a series of matching sections were introduced. Numerical modeling employed the TRT applied to a TEN, primarily to ascertain the operating frequency of the SWA and extract the LW phase and attenuation constants, with respect to the feeder. The series of matching sections serve as loads for the SIW feeder, necessitating careful consideration of section lengths during the design of the SWA. Additionally, Appendix C validates and extends the modeling approach to higher millimeter-wave frequencies of operation, illustrating the versatility of the adopted numerical model for upscaling the design. The structure becomes semi-transparent upon the addition of the AV section, which can be positioned either above or below solar panels, enhancing solar power harvesting capabilities. The measured prototype exhibited a peak RG of 17.5 dBi at 18.6 GHz, demonstrating excellent agreement between the simulated and measured beam patterns, along with high radiation efficiency exceeding 90% and low SLLs and directive beam patterns oriented directly at the endfire position. This design also supports high data rate capabilities for downlink communications, other small satellite missions, or any scenario requiring a low-profile, non-deployable antenna design with direct endfire radiation.

- Designing a planar optically semi-transparent endfire antenna operating at 24 GHz. Based on SIW technology, the design employed efficient methods to excite the TM_0 SW mode. Utilising an ungrounded dielectric slab with eight AV sections, the antenna achieved an endfire beam pattern, ensuring minimal reflections for radiation into the air region. The feeding technique was also explored considering a single SIW horn as well as an array of SIW horns. The proposed antenna with arrays of SIW horns demonstrated an impressive

directivity of 21.3 dBi and exhibited a SLL of -9.2 dB in the yz plane, while in the xy plane, the SLL reached -11 dB.

6.3 Future Work

The proposed implementations offer numerous advantages but also hold potential for future improvements and perhaps new CubeSat antenna missions. The following is a list of potential future work for each system:

- In Chapter 3, this SIW T-junction planar launcher can be redesigned using substrates with different permittivity, especially when considering operation at higher millimetre-wave frequencies. This redesign could potentially achieve a truly endfire pattern, thereby reducing side and back-lobe radiation and enhancing the forward directivity of the pattern. Another method to enhance directivity, applicable in environments where space industry constraints are not a concern, involves adding a reflector plate above the antenna structure. This plate, with specific dimensions and distance from the antenna, would concentrate the SW fields toward the end of the structure. This configuration could result in reduced side and back-lobe radiation and more efficient radiation in the endfire direction.
- In Chapter 4, further optimisation and co-design possibilities exist for this SWA, involving integration with solar cells and considering CubeSat placement. Additionally, other designs could be pursued to assess both radiation and solar power harvesting performances. Moreover, a potential enhancement of this structure includes the introduction of CP in the CubeSat application. This can be achieved by integrating four single-layer antennas, resulting in CP with high gain and solar cell integration. Addressing the feeding issues and integrating circuit feeding for the millimetre-wave structures is also a vital area for future research, preparing them for fabrication.
- In Chapter 5, the initial step involved designing a microstrip line feeding for the SIW horns and establishing a feeding network for the array. Subsequently, the SWA needs to be manufactured, and its actual performance should be compared with the simulation results. Additionally, experimental tests need to be conducted on the antenna with solar panels to evaluate both its radiation and solar power harvesting performance. Another viable approach is to change the feeding from the SIW horns to directive SWLs, for example [26]. This modification can enhance the compactness of the antenna, aligning

further with CubeSat requirements. Moreover, achieving CP with this structure will add more value and should that be needed, given the preferences in space communications.

Appendix A
List of Publications

Conference Papers

- **K. Alrushud**, V. G. -G. Buendía and S. K. Podilchak, "Planar Quasi-End-Fire Antenna Design using SIW Technology for CubeSats and Other Small Satellites," 2021 15th European Conference on Antennas and Propagation (EuCAP).
- B. Alshammari, **K. Alrushud**, M. Kuznetcov, Y. Li and S. K. Podilchak, "Dual-Band Dually-Polarized Compact Folded-Shorted Patch Array for Small Satellites," 2021 IEEE International Symposium on Antennas and Propagation and USNC-URSI Radio Science Meeting (APS/URSI).
- M. Kuznetcov, V. G. -G. Buendía, **K. Alrushud** and S. K. Podilchak, "Simple Matching Technique using Finite Metasurface to Control Surface Waves," 2022 16th European Conference on Antennas and Propagation (EuCAP).
- V. G. -G. Buendía, A. A. Rodríguez, **K. Alrushud** and S. K. Podilchak, "Efficient Surface-wave Excitation by Parallel-Plate Waveguide for Substrate Integrated Image Guides," 2022 16th European Conference on Antennas and Propagation (EuCAP).
- **K. Alrushud**, B. Alshammari and S. K. Podilchak, "Towards Optically Semi-Transparent Planar Endfire Antennas for CubeSats and Other Small Satellites," 2023 IEEE Conference on Antenna Measurements and Applications (CAMA).

Journal Papers

- **K. M. Alrushud**, V. G. -G. Buendía and S. K. Podilchak, "Compact Substrate Integrated Waveguide Quasi-Endfire Antenna for CubeSat Integration," in IEEE Antennas and Wireless Propagation Letters, vol. 20, no. 11, pp. 2120-2124, Nov. 2021.

- B. Alshammari, **K. Alrushud**, Y. Li and S. K. Podilchak, "Compact Folded-Shorted Patch Array Offering Dual-Band Operation and Dual-Circularly Polarised Radiation for Picosatellites and Other Small Satellites." in Electronics Letters, 2023.
- **K. M. Alrushud**, V. G. -G. Buendía and S. K. Podilchak, "Planar Surface-Wave Antenna for CubeSats with Directive Radiation Exactly at Endfire," in IEEE Transactions on Antennas and Propagation, 2023, [Under Review].

Publications in Preparation

- **K. Alrushud**, B. Alshammari and S. K. Podilchak, "Optically Semi-Transparent Planar Endfire Circularly Polarised Antenna for CubeSats and Other Small Satellites," in IEEE Transactions on Antennas and Propagation, 2024.

Appendix B
Transverse Equivalent Network Codes

In this appendix, the Wolfram Mathematica codes are reported. They were used to design and assist in generating α_{LW} and β_{LW} values for the surface wave antenna (SWA) structure proposed in chapter 4. These codes are formulated based on the equations and visual representations detailed in Section 4.4.2.

Furthermore, Sections B.1, B.2, and B.3 encompass codes that provide guidance on computing the Z_{SMS}, Z_{SW}, and Z_{AV} impedances. These codes are integral components of the Transverse Equivalent Network (TEN) code, elaborated upon in Section B.4. This code can assist in calculating the dispersive features for the LW field within the SIW T-junction. The employed matching sections and air region act as a combined load to the feeder.

B.1 Calculating Z_{SMS} Code

In this section, the code will use the transverse resonance technique (TRT) to calculate the phase propagation constant (β_{SMS}) for the sub-wavelength matching section (SMS). This value will then be utilised in the code to determine the SMS impedance flowing ($Z_{SMS} = \beta_{MS}/\omega\epsilon_r\epsilon_o$). Here is an explanation of the Wolfram Mathematica code:

```
(*Comments and Variables*)
Eo = 8.854*10^-12;(*Permittivity of free space*)
muo = Pi*4*10^-7;(*Permeability of free space*)
eta = Sqrt[muo/Eo];(*Wave impedance of free space*)
Er = 2.2; (*Permittivity of the dielectric*)
c = 1/Sqrt[muo*Eo];  (*Speed of light*)
lambda = 1/(freq*Sqrt[muo*Eo*Er]);(*Wavelength*)
omega = 2*Pi*freq;  (*Angular Frequency*)
h = 1.575*10^-3;   (*The thickness of the dielectric*)
```

```
(*Dimensions of the Subwavelength patches*)
DMS = 3.485*10^-3;  (*The distance between patches*)
GMS = 0.335*10^-3;  (*The gap between  the patches*)
Eeff = (Er + 1)/2;  (*The relative effective permittivity*)
Etaeff = Sqrt[muo/(Eo*Eeff)]; (*The effective impedance*)

(*Wavenumber in the substrate*)
K1 = omega*Sqrt[muo*Eo*Er];(*Wavenumber in the substrate*)
Ko = omega*Sqrt[muo*Eo];    (*Wavenumber in the free space*)

(*Identifying the impedances for the regions*)
Z00[Kz_] := Kx0[Kz]/(omega*Eo);
Z01[Kz_] := Kx1[Kz]/(omega*Eo*Er);

Kx0[Kz_] := Sqrt[Ko^2 - Kz^2];
Kx1[Kz_] := Sqrt[K1^2 - Kz^2];

(*TRE*)
Zp[Kz_] := (Z00[Kz]*Zg)/(Z00[Kz] + Zg)

Zup[Kz_] :=
  Z01[Kz] ((Zp[Kz] + (I*Z01[Kz]*Tan[Kx1[Kz]*(h/2)]))/(Z01[
       Kz] + (I*Zp[Kz]*Tan[Kx1[Kz]*(h/2)])));
Zdown[Kz_] := (I*Z01[Kz]*Tan[Kx1[Kz]*(h/2)]);

(*to identify the equation equal to 0*)
eqDisp[Kz_] := Zup[Kz] + Zdown[Kz];

fIn = 18*10^9;
K0p = 2*Pi*fIn*Sqrt[muo*Eo];    (*Wavenumber in the free space*)
K1p = 2*Pi*fIn*Sqrt[muo*Eo*Er];(*Wavenumber in the substrate*)

(*Here to make the function search nearby the initial \
```

```
value, which needs to be identified with the proper mode TM0*)
Kzin = (1.23788 + (0.00000251457*I))*K0p;

(*Calculating the surface grid Impedance*)
GammaMS = ((K1p*DMS)/Pi)*Log[1/Sin[(Pi*GMS)/(2*DMS)]];
ZgC = -I (Etaeff/(2*GammaMS));      (*Surface grid impedance*)

N[s = FindRoot[(eqDisp[Kz]/.{freq -> fIn, Zg -> ZgC})==0, {Kz,
    Kzin}]]
kzprova = Replace[Kz, s];
kzprova_norm = kzprova/K0p
Zms = kzprova/(2*Pi*fIn*Er*Eo)    (*matching section impedance*)
```

B.2 Calculating Z_{SW} Code

This section utilises the TRT to compute the phase propagation constant (β_{SW}) for the grounded dielectric slab (GDS). This value was then used to calculate the impedance for the GDS using the formula ($Z_{SW} = \beta_{SW}/\omega\epsilon_r\epsilon_o$). Below is an explanation of the Wolfram Mathematica code:

```
(*Comments and Variables*)
Eo = 8.854*10^-12;  (*Permittivity of free space*)
muo = Pi*4*10^-7; (*Permeability of free space*)
eta = Sqrt[muo/Eo];  (*Wave impedance of free space*)
Er = 2.2;      (*Permittivity of the dielectric*)
lambda = 1/(freq*Sqrt[muo*Eo*Er]);     (*Wavelength*)
omega = 2*Pi*freq;    (*Angular Frequency*)
h = 1.575*10^-3;      (*The thickness of the dielectric*)

(*Wavenumber in the substrate*)
K1 = omega*Sqrt[muo*Eo*Er]; (*Wavenumber in the substrate*)
Ko = omega*Sqrt[muo*Eo];     (*Wavenumber in the free space*)

(*TRE*)
eqDisp[Kz_] :=Tan[Sqrt[K1^2 - Kz^2]*h]*Sqrt[K1^2- Kz^2]- Er*
```

```
            Sqrt[Kz^2  - Ko^2];

fIn = 18*10^9;
K0p = 2*Pi*fIn*Sqrt[muo*Eo];  (*Wavenumber in the free space*)

(*Here to make the function search nearby the initial \
value, which needs to be identified with the proper mode TM0*)
Kzin = 300;

N[s = FindRoot[(eqDisp[Kz] /. {freq -> fIn}) == 0, {Kz, Kzin}]]
kzprova = Replace[Kz, s];
kzprova_norm = kzprova/K0p
Zsw = kzprova/(2*Pi*fIn*Er*Eo)  (*The SW GDS impedance*)
```

B.3 Calculating Z_{AV} Code

To calculate Z_{AV}, the same code explained in Section B.2, with a modification can be used. Instead of using the relative permittivity of the substrate ϵ_r, replace it with the relative effective permittivity $\epsilon_{r_{eff}}$ obtained by using Equation 4.13 for the AV section. Once you have generated the phase propagation constant (β_{AV}) for the AV section, you can calculate the impedance using the formula ($Z_{AV} = \beta_{AV}/\omega\epsilon_{r_{eff}}\epsilon_o$).

B.4 Generating α_{LW} and β_{LW} using TEN Code

To calculate the dispersive feature α_{LW} and β_{LW}, use the TRT as described in Section 4.4.2. Prior to using the code below, ensure that the impedance values Z_{SMS}, Z_{SW} and Z_{AV} have been obtained from the codes in the previous sections, labelled as B.1, B.2, and B.3. Once the impedance values are available, the code can be used to generate α_{LW} and β_{LW}.

```
(*Comments and Variables*)
Eo = 8.854*10^-12;  (*Permittivity of free space*)
muo = Pi*4*10^-7;  (*Permeability of free space*)
eta = Sqrt[muo/Eo];  (*Wave impedance of free space*)
```

```
Er = 2.2;     (*Permittivity of the dielectric*)
mur = 1;
lambda = 1/(freq*Sqrt[muo*Eo*Er]);    (*Wavelength*)
omega = 2*Pi*freq;  (*Angular Frequency*)
S1 = 5.33*10^-3;  (*Length of the PPW section*)
S2 = 6.97*10^-3; (*Length of the SMS*)
S3 = 68*10^-3;  (*Length of the GDS section*)
S4 = 92.7*10^-3; (*Length of the AVs section*)
h = 1.575*^-3;    (*The thickness of the dielectric*)

(*Wavenumber in the substrate*)
Ke = omega*Sqrt[muo*Eo*Er]; (*Wavenumber in the substrate*)
Ko = omega*Sqrt[muo*Eo];    (*Wavenumber in the free space*)

(*Dimensions*)
a = 4.5*10^-3; (*PITCH for the PRS*)
d = 1*10^-3;    (*Diameter of the via*)
W = 5.67*10^-3; (*SIW Width*)

Z0TE[Kz_] := omega*muo/Kx[Kz];    (*TE wave impedance*)

eta0 = 376.73;
eta = eta0*Sqrt[mur/Er];
Z0TEM = eta*(h/S1);    (*TEM wave impedance*)

Cosphi[Kz_] := Kx[Kz]/Ke;

Kx[Kz_] := Sqrt[Ke^2 - Kz^2];
(*Enforcing improper solutions*)
Kx[Kz_] := Sqrt[(Ke^2 - Kz^2)] /; Im[(Ke^2 - Kz^2)] > 0
Kx[Kz_] := -Sqrt[(Ke^2 - Kz^2)] /; Im[(Ke^2 - Kz^2)] <= 0

(*TNetwork*)
```

```
Xa[Kz_] := (a*Cosphi[Kz]/lambda)*(Log[a/(2*Pi*d/2)] +
      0.601*(3 - 2*Cosphi[Kz]^2)*(a/lambda)^2);
Xb[Kz_] := (a*Cosphi[Kz]/lambda)*(2*Pi*(d/2)/a)^2;

XaUn[Kz_] := Xa[Kz]*Z0TE[Kz];
XbUn[Kz_] := Xb[Kz]*Z0TE[Kz];

(*Transverse Resonance Method for the proposed structure*)

ErAir = 1; (*The Permittivity of the Air*)
c = 1/Sqrt[muo*Eo]; (*Speed of light*)
Lambda0 = c/freq;
BetaA = 2 Pi/Lambda0;  (*Beta for air section*)
Z0TM := BetaA/(omega*Eo*ErAir);(*TM wave impedance for Air*)

(*The SMS impedances for the frequencies that we want, which\
have been calculated using SMS impedance code *)
ZmsData = Import[".csv"];
(*To get the Zms for the right frequency that we want\
after we calculate it using SMS impedance code*)
Zms := Transpose[{ZmsData[[ZF,2]]}]  )

(*The SW impedances for the frequencies that we want, which\
have been calculated using SW impedance code*)
ZswData = Import[".csv"];
(*To get the Zsw for the right frequency that we want\
after we calculate it using SW impedance code*)
Zsw := Transpose[{ZswData[[ZF,2]]}]

(*The AV impedances for the frequencies that we want, which\
have been calculated using AV impedance code*)
ZswavData = Import[".csv"];
(*To get the Zav for the right frequency that we want\
```

```
after we calculate it using AV impedance code*)
Zswav := Transpose[{ZswData[[ZF,2]]}]


Zin1[Kz_] :=
  Zswav*((Z0TM + (I*Zswav*Tan[Kx[Kz]*S4]))/(Zswav + (I*Z0TM*
        Tan[Kx[Kz]*S4])));

Zin2[Kz_] :=
  Zsw*((Zin1[
       Kz] + (I*Zsw*Tan[Kx[Kz]*S3]))/(Zsw + (I*Zin1[Kz]*
        Tan[Kx[Kz]*S3])));

Zin3[Kz_] :=
  Zms*((Zin2[
       Kz] + (I*Zms*Tan[Kx[Kz]*S2]))/(Zms + (I*Zin2[Kz]*
        Tan[Kx[Kz]*S2])));

Zin4[Kz_] :=
  Z0TEM*((Zin3[
       Kz] + (I*Z0TEM*Tan[Kx[Kz]*S1]))/(Z0TEM + (I*Zin3[Kz]*
        Tan[Kx[Kz]*S1])));


ZL[Kz_] := (I*Tan[Kx[Kz]*W]*Z0TE[Kz]) - I*XbUn[Kz];
ZR[Kz_] := (I*
     XaUn[Kz]*((Zin4[Kz]) - I*XbUn[Kz]))/(I*XaUn[Kz] + (Zin4[
     Kz]) - I*XbUn[Kz]);


(*to identify the equation that is equal to 0*)
eqDisp[Kz_] := ZL[Kz] + ZR[Kz];
```

```
fIn = 18*10^9;
KeCST = 2*Pi*fIn*Sqrt[muo*Eo*Er];
K0CST = 2*Pi*fIn*Sqrt[muo*Eo];
(*The value here has been calculated using Bloch Analysis*)
KzCST = (0.504 - I*0.01855)*KeCST;
KxCST = Sqrt[KeCST^2 - KzCST^2];
ZF = 1;

Kzin = KzCST;  (*Here to make the function search nearby the \
initial value, which Bloch Analysis calculated*)
N[s = FindRoot[(eqDisp[Kz] /. {freq -> fIn}) == 0, {Kz, Kzin}]]
kzprova = Replace[Kz, s];
kzprova_norm = kzprova/K0CST
```

Appendix C
Application to Millimetre-wave Structures

This Appendix will provide a parametric study by using the adopted transverse resonance technique (TRT) for higher millimetre-wave frequencies of operation (see Figure C.1 and Table C.1). Some brief full-wave simulations follow to demonstrate scalability of the dual-layer design using a commercial full-wave simulator (see Figures C.3 and C.2).

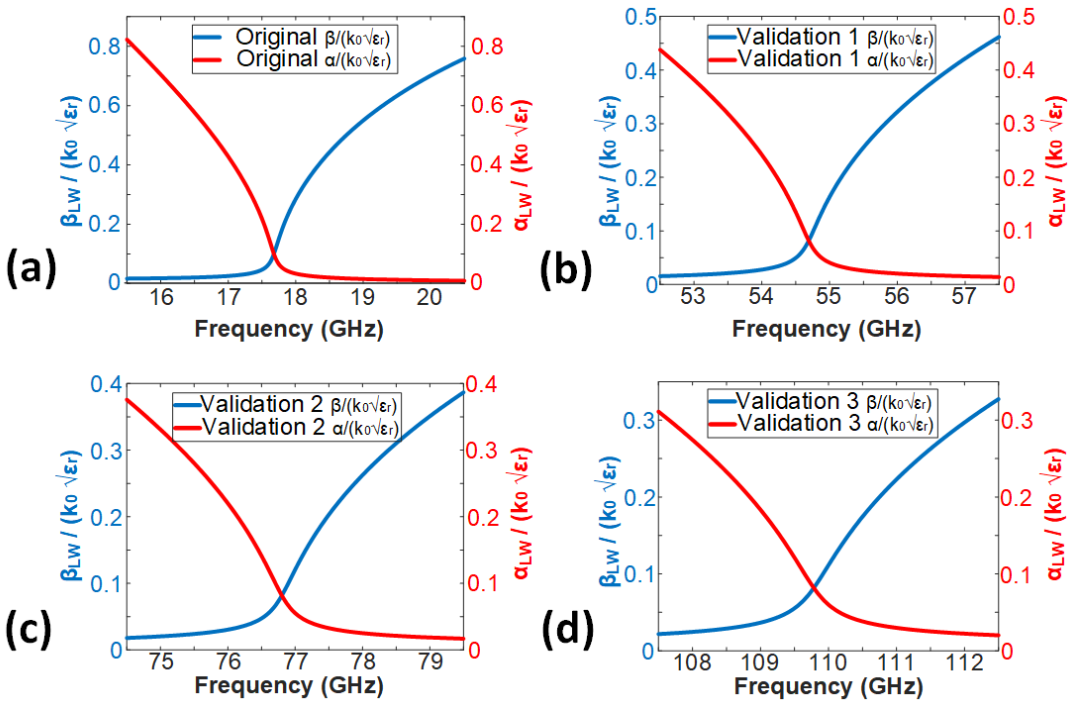

Figure C.1: *Numerical α and β calculations for the modelled SIW antenna feeder and loading defined by the different SW guiding sections (see Figure 4.1). In particular, the normalised LW phase constant β/k_0 is in blue and α/k_0 in red: (a) original 18 GHz design, (b) validation design 1 (55 GHz), (c) validation design 2 (77 GHz), and (d) validation design 3 (110 GHz). These results show the complex solution of the TRE (see Equation 4.1) defined by the proposed TEN as in Figure 4.4.*

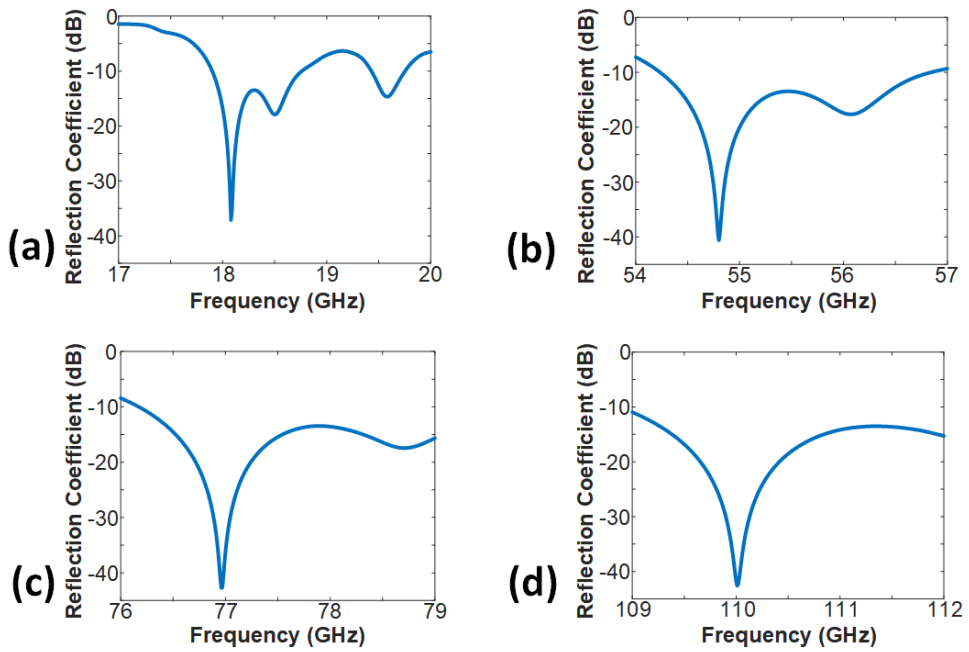

Figure C.2: *Simulated reflection coefficient versus frequency for the various microwave and millimetre-wave frequency designs*

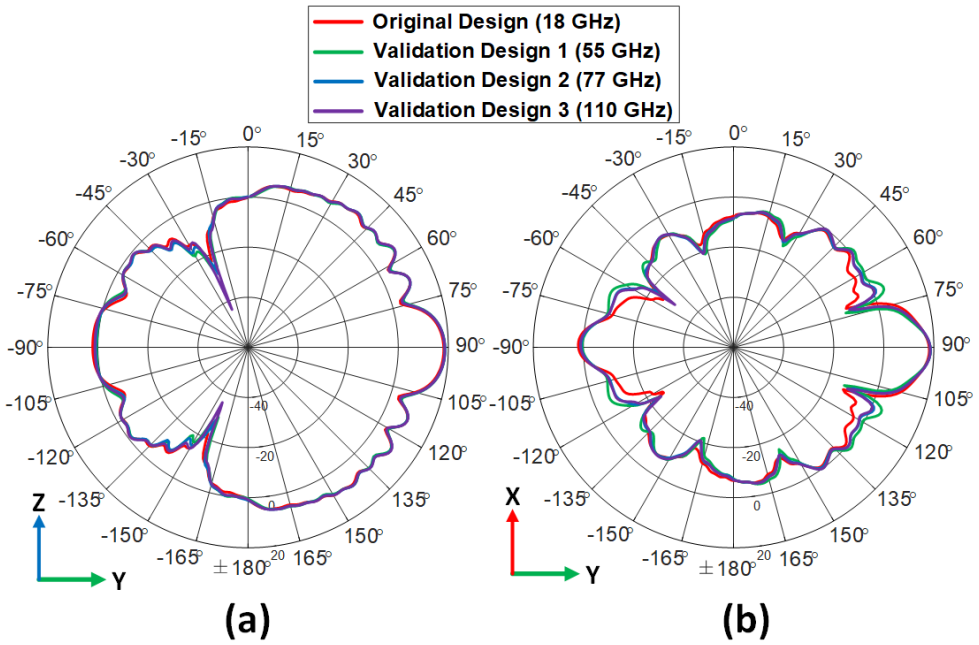

Figure C.3: *RG patterns in (a) the yz plane ($\phi = 90°$) and (b) the xy plane ($\theta = 90°$) for the various microwave and millimetre-wave frequency designs. Very consistent peak gain values and patterns are shown, and all with low SLLs and radiation exactly at endfire.*

Design	**Original (see Tab. 4.1)**	**Validation 1**	**Validation 2**	**Validation 3**
Frequency (GHz)	**18**	**55**	**77**	**110**
W_s **(mm)**	79.50	26.23	18.70	13.07
L_s**(mm)**	212.32	73.89	52.62	36.81
S_1**(mm)**	5.33	1.76	1.25	0.88
S_2**(mm)**	6.97	2.30	1.64	1.15
S_3**(mm)**	68.00	22.45	16.00	11.18
S_4**(mm)**	92.70	30.60	21.80	15.24
D_{Air}**(mm)**	2.00	0.66	0.47	0.33
P_{Air}**(mm)**	2.20	0.73	0.52	0.36
G**(mm)**	0.33	0.11	0.08	0.05
D**(mm)**	3.48	1.15	0.82	0.57
L**(mm)**	54.00	17.82	12.70	8.88
P_{PRS}**(mm)**	4.50	1.48	1.06	0.74
S'**(mm)**	3.17	1.05	0.74	0.52
d'**(mm)**	0.21	0.07	0.05	0.03
W_{WG}**(mm)**	5.67	1.90	1.33	0.93
P**(mm)**	1.93	0.64	0.45	0.32
d**(mm)**	1.00	0.33	0.23	0.16
W_{SIW}**(mm)**	6.99	2.31	1.64	1.15
W_h**(mm)**	8.56	2.82	2.01	1.41
L_t**(mm)**	8.85	2.92	2.08	1.45
W_o**(mm)**	4.85	1.60	1.40	0.80
L_o**(mm)**	12.20	4.03	2.87	2.00
h**(mm)**	1.57	0.52	0.37	0.26
ϵ_r**(mm)**	2.2	2.2	2.2	2.2

Table C.1: *Numerically Determined Dimensions for the SWA Considering the Original Design & Three Other Validation Frequencies: 55 GHz, 77 GHz, and 110 GHz*

Basically the design of three more SWA structures with different operational frequencies for validation of the adopted modelling approach is reported herein. In particular, designs at 55 GHz, 77 GHz, and 110 GHz. All structures include 42 rows for the AV section and all other

optimised structure dimensions are outlined in Table C.1. This parametric study is included to illustrate the usefulness of the developed numerical modelling approach (previously outlined in Sec. 4.4.2) which can speed up the design process. Basically, by applying the transverse equivalent network (TEN) and solving the transverse resonance equation (TRE), whilst having some baseline model information at 18 GHz which have been normalised to the guided wavelength λ_g (see Tables 4.2 to 4.5), the determination of the structure dimensions becomes significantly less time consuming in terms of characterising the section lengths required to achieve $\alpha \approx \beta$ at the desired frequency, and as compared to analogous full-wave optimisations in a commercial simulator.

The plot of the numerical calculations for α and β of the four structures are depicted in Figure C.1. It can be observed that $\alpha \approx \beta$ for the four SWA structures at about the desired frequencies: 18 GHz (i.e. the original design), 55 GHz (validation design 1), 77 GHz (validation design 2), and 110 GHz (validation design 3). Simulated reflection coefficient values also show consistent -30 dB impedance matching (or less) at these frequencies (see Figure C.2). Figure C.3 also reports the simulated beam patterns for the original 18 GHz design as well as the millimetre-wave structures. In particular, realised gain (RG) plots in the yz plane and the xy plane. The peak RG for the 18 GHz design is 18.2 dBi as well as 19.0 dBi, 18.8 dBi and 18.8 dBi for the 55 GHz, 77 GHz, and 110 GHz designs, respectively. Other operational frequencies are possible, but the motivation here is to show that the design and modelling approach for the SWA can be applied to other frequencies as desired.

Appendix D
Feeding Considerations and Practical Implementation

In this appendix, additional details about the feeding considerations for the fabricated structure (proposed SWA in Chapter 4) are discussed. Section D.1 presents various designs for microstrip lines that can solve the practical two-port feeding problem for this SWA while keeping the CubeSat standard size in mind. Moreover, Section D.2 shows the impact of the RF connector on the beam patterns and reflection coefficient results.

D.1 Microstrip Line Feeder

Four alternative microstrip feedline configurations, distinct from the straight configuration, were introduced to address the challenge posed by the dual-layer antenna arrangement when accommodating RF connectors. This is necessitated by the shared ground for the two-layer structure. Figure D.1 displays the straight microstrip line and the four other designs: the spline, 10 mm 90° curve line, 20 mm 90° curve line, and full 90° curve line. These designs added a length L_{MSL} to the structure, with the straight microstrip line adding 12.2 mm, the spline microstrip line adding 32.2 mm, the 10 mm 90° curve microstrip line adding 26.0 mm, the 20 mm 90° curve microstrip line adding 36.0 mm, and the full 90° curve microstrip line adding 54.7 mm.

The reflection coefficient versus frequency and electric field inside the substrate for different microstrip line designs are presented in Figures D.2 and D.3. Figure D.2 shows that the spline design has a shifted resonance at around 19 GHz and the worst response, while the full 90° curve microstrip line has the best response, similar to the straight line. Figure D.3 shows that the full 90° curve microstrip line has the best matching and most of the electric field transfers to the SIW, while the spline design has inefficient electric field transfer away from the SIW. In conclusion, based on these findings, it is recommend that the full 90° curve microstrip line be considered for the dual-layer distributed aperture antenna reported in Chapter 4.

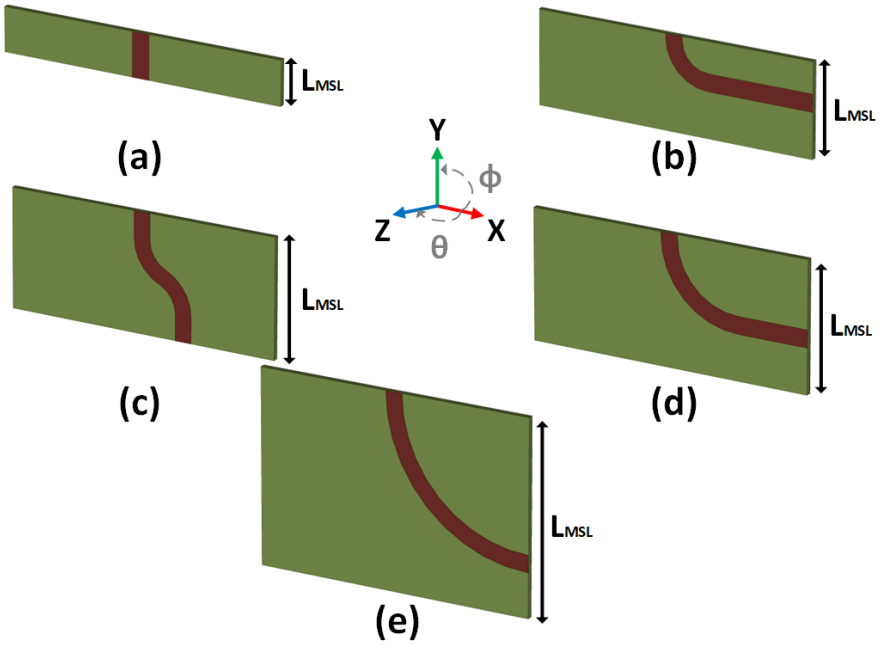

Figure D.1: *Possible microstrip line structures for the SWA, (a) straight microstrip line, (b) 10 mm 90° curve microstrip line, (c) spline microstrip line, (d) 20 mm 90° curve microstrip line, and (e) full 90° curve microstrip line.*

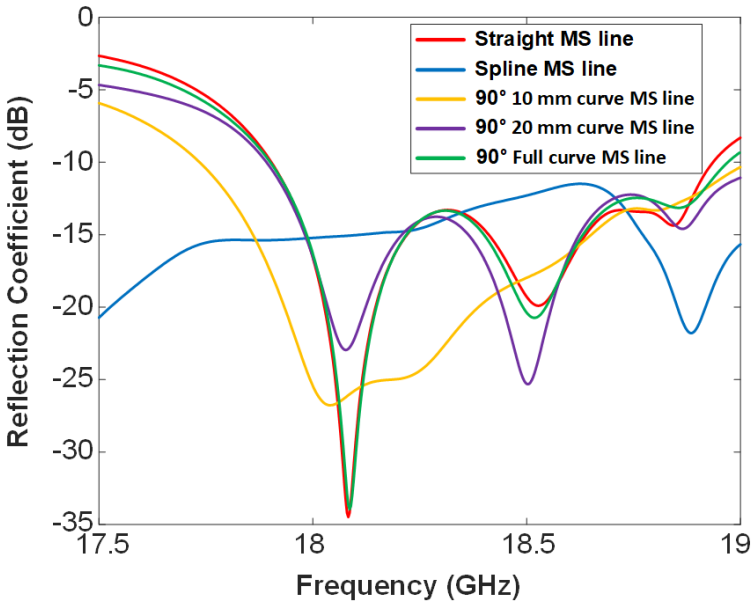

Figure D.2: *Simulated reflection coefficient versus frequency for the different proposed microstrip line structures for the SWA.*

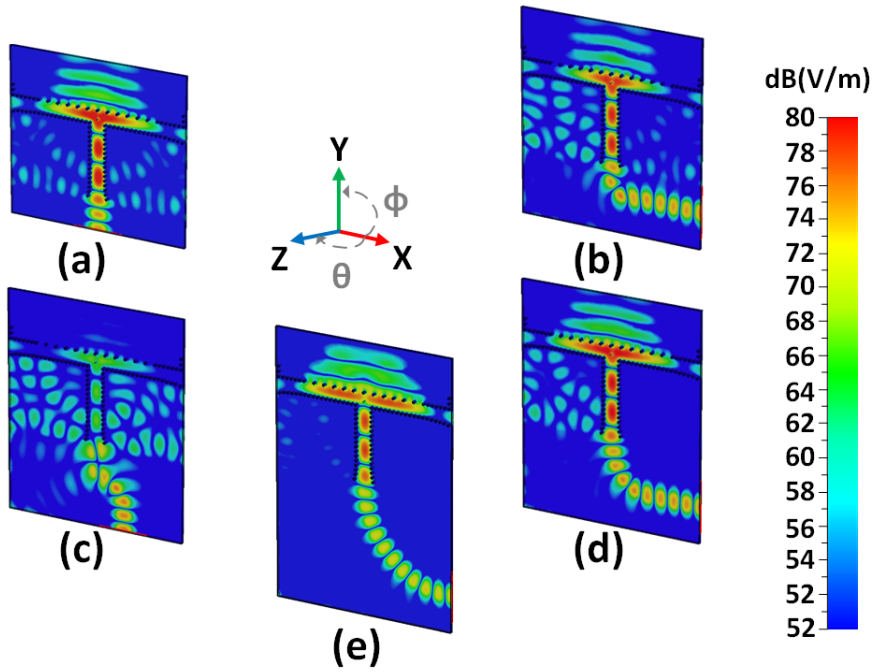

Figure D.3: *Simulated electric field inside the substrate for the different microstrip feeding considerations, (a) straight microstrip line, (b) 10 mm* 90° *curve microstrip line, (c) spline microstrip line, (d) 20 mm* 90° *curve microstrip line, and (e) full* 90° *curve microstrip line.*

D.2 RF Connector

This section will examine how the RF connector and the small transition between the RF connector and microstrip lines affect the performance of the system. Figure D.4 shows the simulated beam pattern for the dual-layer SWA design with 42 rows of AVs and 68 mm for the length of the GDS and with straight microstrip lines, full 90° curve microstrip lines with and without an RF connector in both the yz and xy planes. The results indicate that there is good agreement between the three designs in the yz plane, but in the xy plane, the antenna with the full 90° curve microstrip line with the RF connector experienced a rise in the SLL of 0.8 dB at 0° and 180° due to the added RF connector.

Figure D.5 displays the simulated reflection coefficient versus frequency for the dual-layer SWA design with straight microstrip lines, full 90° curve microstrip lines with and without an RF connector. The responses for each design are slightly different from one another. However, the figure shows that all three structures are matched for the desired frequency.

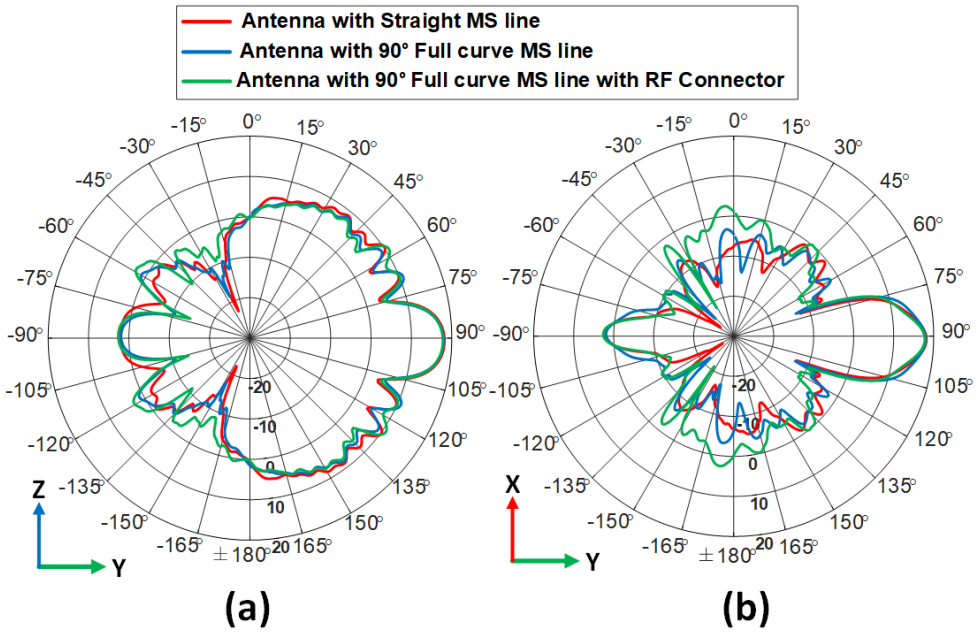

Figure D.4: *Simulated beam pattern in (a) the yz plane ($\phi = 90°$) and (b) the xy plane ($\theta = 90°$) for the dual-layer SWA with 42 rows of AVs and 68 mm GDS dimension with straight microstrip line, full $90°$ curve microstrip line with and without RF connector.*

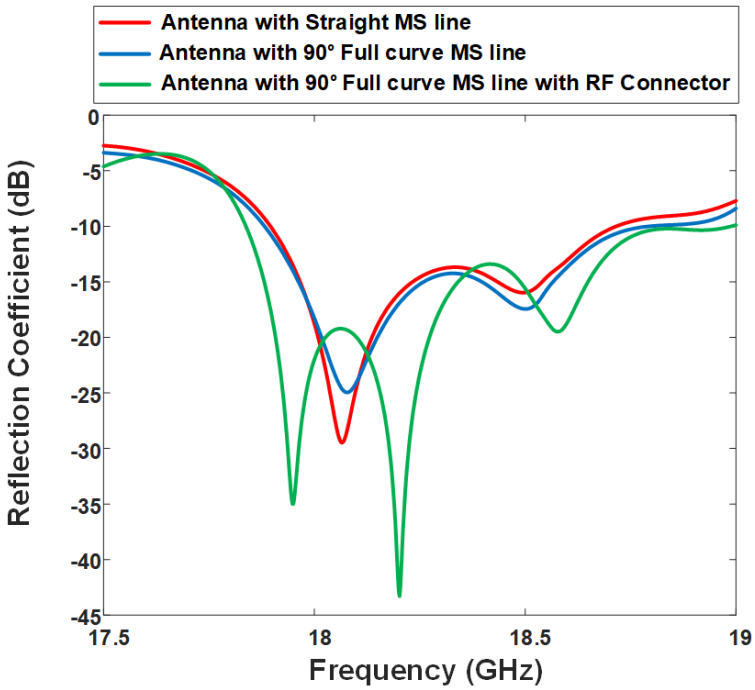

Figure D.5: *Simulated reflection coefficient versus frequency for the dual-layer SWA design.*

References

[1] Y. Rahmat-Samii, V. Manohar, and J. M. Kovitz, "For satellites, think small, dream big: A review of recent antenna developments for CubeSats.," *IEEE Antennas and Propagation Magazine*, vol. 59, no. 2, pp. 22–30, 2017.

[2] S. Gao, Y. Rahmat-Samii, R. E. Hodges, and X.-X. Yang, "Advanced antennas for small satellites," *Proceedings of the IEEE*, vol. 106, no. 3, pp. 391–403, 2018.

[3] N. E. Chahat, "A mighty antenna from a tiny CubeSat grows," *IEEE Spectrum*, vol. 55, no. 2, pp. 32–37, 2018.

[4] Y. Rahmat-Samii and A. C. Densmore, "Technology trends and challenges of antennas for satellite communication systems," *IEEE Transactions on Antennas and Propagation*, vol. 63, no. 4, pp. 1191–1204, 2015.

[5] S. Abulgasem, F. Tubbal, R. Raad, P. I. Theoharis, S. Lu, and S. Iranmanesh, "Antenna designs for CubeSats: A review," *IEEE Access*, vol. 9, pp. 45289–45324, 2021.

[6] R. De, M. P. Abegaonkar, and A. Basu, "Enabling science with CubeSats—trends and prospects," *IEEE Journal on Miniaturization for Air and Space Systems*, vol. 3, no. 4, pp. 221–231, 2022.

[7] E. Peral, E. Im, L. Wye, S. Lee, S. Tanelli, Y. Rahmat-Samii, S. Horst, J. Hoffman, S.-H. Yun, T. Imken, *et al.*, "Radar technologies for Earth remote sensing from CubeSat platforms," *Proceedings of the IEEE*, vol. 106, no. 3, pp. 404–418, 2018.

[8] D. Pozar, "Microwave Engineering, 4th Edition, John Wiley & Sons," 2012.

[9] The MathWorks Inc., "Matlab version: 9.13.0 (r2022b)," 2022.

[10] Wolfram Research Inc, "Mathematica version: 12.2," 2022.

[11] Dassault Systèmes, "CST Microwave Studio," 2020.

[12] Dassault Systèmes, "CST STUDIO SUITE." `https://www.3ds.com/products-services/simulia/products/cst-studio-suite/`, 2023. Accessed: 2024-04-16.

[13] Starlink, "High-Speed Internet." `https://www.starlink.com/`, 2023. Accessed: 2024-04-16.

[14] Y. Li, S. K. Podilchak, D. E. Anagnostou, C. Constantinides, and T. Walkinshaw, "Compact antenna for picosatellites using a meandered folded-shorted patch array," *IEEE Antennas and Wireless Propagation Letters*, vol. 19, no. 3, pp. 477–481, 2020.

[15] S. K. Podilchak, A. P. Murdoch, and Y. M. M. Antar, "Compact, microstrip-based folded-shorted patches: PCB antennas for use on microsatellites," *IEEE Antennas and Propagation Magazine*, vol. 59, no. 2, pp. 88–95, 2017.

[16] Y. Li, S. K. Podilchak, and D. E. Anagnostou, "A miniaturized circularly polarized antenna using a meandered folded-shorted patch array for CubeSats," in *2020 14th European Conference on Antennas and Propagation (EuCAP)*, pp. 1–5, IEEE, 2020.

[17] Y. Li, S. K. Podilchak, and D. E. Anagnostou, "Compact folded-shorted patch antenna array with PCB implementation for modern small satellites," in *2020 IEEE Aerospace Conference*, pp. 1–7, IEEE, 2020.

[18] S. K. Podilchak, M. Caillet, D. Lee, Y. M. M. Antar, L. C. Chu, J. Cain, M. Hammar, D. Caldwell, and E. Barron, "A compact circularly polarized antenna using an array of folded-shorted patches," *IEEE Transactions on Antennas and Propagation*, vol. 61, no. 9, pp. 4861–4867, 2013.

[19] A. Nascetti, E. Pittella, P. Teofilatto, and S. Pisa, "High-gain S-band patch antenna system for Earth-observation CubeSat satellites," *IEEE Antennas and Wireless Propagation Letters*, vol. 14, pp. 434–437, 2014.

[20] M. J. Veljovic and A. K. Skrivervik, "Aperture-coupled low-profile wideband patch antennas for CubeSat," *IEEE Transactions on Antennas and Propagation*, vol. 67, no. 5, pp. 3439–3444, 2019.

[21] S. K. Podilchak, D. Comite, B. K. Montgomery, Y. Li, V. G.-G. Buendía, and Y. M. M. Antar, "Solar-panel integrated circularly polarized meshed patch for CubeSats and other small satellites," *IEEE Access*, vol. 7, pp. 96560–96566, 2019.

[22] T. Yasin and R. Baktur, "Bandwidth enhancement of meshed patch antennas through proximity coupling," *IEEE Antennas and Wireless Propagation Letters*, vol. 16, pp. 2501–2504, 2017.

[23] T. Yekan and R. Baktur, "Conformal integrated solar panel antennas: Two effective integration methods of antennas with solar cells.," *IEEE Antennas and Propagation Magazine*, vol. 59, no. 2, pp. 69–78, 2017.

[24] S. Zarbakhsh, M. Akbari, M. Farahani, A. Ghayekhloo, T. A. Denidni, and A.-R. Sebak, "Optically transparent subarray antenna based on solar panel for CubeSat application," *IEEE Transactions on Antennas and Propagation*, vol. 68, no. 1, pp. 319–328, 2019.

[25] Y. Cao, Y. Cai, L. Wang, Z. Qian, and L. Zhu, "A review of substrate integrated waveguide end-fire antennas," *IEEE Access*, vol. 6, pp. 66243–66253, 2018.

[26] S. Podilchak, A. Freundrofer, and Y. Antar, "Planar antenna for directive beam steering at end-fire using an array of surface-wave launchers," *Electronics letters*, vol. 45, no. 9, pp. 444–445, 2009.

[27] P. Liu, Y. Li, Z. Zhang, and P. Jia, "All-metal centipede-like end-fire antenna," *IEEE Antennas and Wireless Propagation Letters*, vol. 17, no. 10, pp. 1905–1909, 2018.

[28] H. Wang, D.-G. Fang, B. Zhang, and W.-Q. Che, "Dielectric loaded substrate integrated waveguide (SIW) H-plane horn antennas," *IEEE Transactions on Antennas and Propagation*, vol. 58, no. 3, pp. 640–647, 2009.

[29] S. Liu, R. Raad, P. I. Theoharis, and F. Tubbal, "Dual-band folded-end dipole antenna for plastic CubeSats," *IEEE Journal on Miniaturization for Air and Space Systems*, vol. 1, no. 3, pp. 172–178, 2020.

[30] X. Zhang, F. Sun, G. Zhang, and L. Hou, "Compact UHF/VHF monopole antennas for CubeSats applications," *IEEE Access*, vol. 8, pp. 133360–133366, 2020.

[31] J. Costantine, Y. Tawk, I. Maqueda, M. Sakovsky, G. Olson, S. Pellegrino, and C. G. Christodoulou, "UHF deployable helical antennas for CubeSats," *IEEE Transactions on Antennas and Propagation*, vol. 64, no. 9, pp. 3752–3759, 2016.

[32] D. Gonzalez-Ovejero, N. Chahat, R. Sauleau, G. Chattopadhyay, S. Maci, and M. Ettorre, "Additive manufactured metal-only modulated metasurface antennas," *IEEE Transactions on Antennas and Propagation*, vol. 66, no. 11, pp. 6106–6114, 2018.

[33] P. Bouça, J. N. Matos, S. R. Cunha, and N. B. Carvalho, "Low-profile aperture-coupled patch antenna array for CubeSat applications," *IEEE Access*, vol. 8, pp. 20473–20479, 2020.

[34] X. Li, J. Wang, G. Goussetis, and L. Wang, "Circularly polarized high gain leaky-wave antenna for CubeSat communication," *IEEE Transactions on Antennas and Propagation*, vol. 70, no. 9, pp. 7612–7624, 2022.

[35] R. E. Hodges, N. Chahat, D. J. Hoppe, and J. D. Vacchione, "A deployable high-gain antenna bound for Mars: Developing a new folded-panel reflectarray for the first CubeSat mission to Mars.," *IEEE Antennas and Propagation Magazine*, vol. 59, no. 2, pp. 39–49, 2017.

[36] A. Babuscia, M. Van de Loo, Q. J. Wei, S. Pan, S. Mohan, and S. Seager, "Inflatable antenna for CubeSat: fabrication, deployment and results of experimental tests," in *2014 IEEE Aerospace Conference*, pp. 1–12, IEEE, 2014.

[37] N. Chahat, R. E. Hodges, J. Sauder, M. Thomson, and Y. Rahmat-Samii, "The deep-space network telecommunication CubeSat antenna: Using the deployable Ka-band mesh reflector antenna.," *IEEE Antennas and Propagation Magazine*, vol. 59, no. 2, pp. 31–38, 2017.

[38] P. A. Warren, J. W. Steinbeck, R. J. Minelli, and C. Mueller, "Large, deployable S-band antenna for a 6U CubeSat," in *2015 29th Annual AIAA/USU Conference on Small Satellites*, Utah State University, 2015.

[39] N. Chahat, E. Thiel, J. Sauder, M. Arya, and T. Cwik, "Deployable one-meter reflectarray for 6U-class CubeSats," in *2019 13th European Conference on Antennas and Propagation (EuCAP)*, pp. 1–4, IEEE, 2019.

[40] N. Chahat, E. Decrossas, D. Gonzalez-Ovejero, O. Yurduseven, M. J. Radway, R. E. Hodges, P. Estabrook, J. D. Baker, D. J. Bell, T. A. Cwik, *et al.*, "Advanced CubeSat antennas for deep space and Earth science missions: A review," *IEEE Antennas and Propagation Magazine*, vol. 61, no. 5, pp. 37–46, 2019.

[41] N. Neveu, M. Garcia, J. Casana, R. Dettloff, D. R. Jackson, and J. Chen, "Transparent microstrip antennas for CubeSat applications," in *IEEE International Conference on Wireless for Space and Extreme Environments*, pp. 1–4, IEEE, 2013.

[42] R. M. Rodríguez-Osorio and E. F. Ramírez, "A hands-on education project: Antenna design for inter-CubeSat communications [education column]," *IEEE Antennas and Propagation Magazine*, vol. 54, no. 5, pp. 211–224, 2012.

[43] B. Alshammari, K. M. Alrushud, Y. Li, and S. K. Podilchak, "Compact folded-shorted patch array offering dual-band operation and dual-circularly polarized radiation for picosatellites and other small satellites," *Electronics Letters*, vol. 59, no. 21, p. e12980, 2023.

[44] S. Abulgasem, F. Tubbal, R. Raad, P. I. Theoharis, S. Liu, and M. U. Ali Khan, "A wideband metal-only patch antenna for CubeSat," *Electronics*, vol. 10, no. 1, p. 50, 2020.

[45] Y. Yao, S. Liao, J. Wang, K. Xue, E. A. Balfour, and Y. Luo, "A new patch antenna designed for CubeSat: Dual feed, L\S dual-band stacked, and circularly polarized.," *IEEE Antennas and Propagation Magazine*, vol. 58, no. 3, pp. 16–21, 2016.

[46] H. Lobato-Morales, S. Villarreal-Reyes, E. Guerrero-Arbona, E. Martinez-Aragon, R. Chávez-Pérez, J. Medina-Monroy, and C. Figueroa-Torres, "A 2.45-GHz circular polarization closed-loop travelling-wave antenna for CubeSats," in *2019 International Conference on Electronics, Communications and Computers (CONIELECOMP)*, pp. 154–157, IEEE, 2019.

[47] O. F. G. Palacios, R. E. D. Vargas, J. A. H. Perez, and S. B. C. Erazo, "S-band koch snowflake fractal antenna for CubeSats," in *2016 IEEE ANDESCON*, pp. 1–4, IEEE, 2016.

[48] T. F. C. Leao, V. Mooney-Chopin, C. W. Trueman, and S. Gleason, "Design and implementation of a diplexer and a dual-band VHF/UHF antenna for nanosatellites," *IEEE Antennas and Wireless Propagation Letters*, vol. 12, pp. 1098–1101, 2013.

[49] K. Schraml, A. Narbudowicz, S. Chalermwisutkul, D. Heberling, and M. J. Ammann, "Easy-to-deploy LC-loaded dipole and monopole antennas for CubeSat," in *2017 11th European Conference on Antennas and Propagation (EUCAP)*, pp. 2303–2306, IEEE, 2017.

[50] S. Liu, R. Raad, K.-W. Chin, and F. E. Tubbal, "Dipole antenna array cluster for CubeSats," in *2016 10th International Conference on Signal Processing and Communication Systems (ICSPCS)*, pp. 1–4, IEEE, 2016.

[51] A. H. Lokman, P. J. Soh, S. N. Azemi, M. F. Jamlos, A. A. Al-Hadi, S. Chalermwisutkul, and P. Akkaraekthalin, "Compact circularly polarized S-band antenna for picosatellites," in *2017 International Symposium on Antennas and Propagation (ISAP)*, pp. 1–2, IEEE, 2017.

[52] J. D. Kraus, "The helical antenna," *Proceedings of the IRE*, vol. 37, no. 3, pp. 263–272, 1949.

[53] J. Costantine, Y. Tawk, S. Moth, C. Christodoulou, and S. Barbin, "A modified helical shaped deployable antenna for CubeSats," in *2012 IEEE-APS Topical Conference on Antennas and Propagation in Wireless Communications (APWC)*, pp. 1114–1116, IEEE, 2012.

[54] B. Slade, "The basics of quadrifilar helix antennas," *Orban Microwave Inc., Orlando, FL, USA*, 2015.

[55] J. Costantine, D. Tran, M. Shiva, Y. Tawk, C. Christodoulou, and S. Barbin, "A deployable quadrifilar helix antenna for CubeSat," in *Proceedings of the 2012 IEEE International Symposium on Antennas and Propagation*, pp. 1–2, IEEE, 2012.

[56] O. Yurduseven, C. Lee, D. González-Ovejero, M. Ettorre, R. Sauleau, G. Chattopadhyay, V. Fusco, and N. Chahat, "Multibeam Si/GaAs holographic metasurface antenna at W-band," *IEEE Transactions on Antennas and Propagation*, vol. 69, no. 6, pp. 3523–3528, 2021.

[57] S. X. Ta, V. D. Le, K. K. Nguyen, and C. Dao-Ngoc, "Planar circularly polarized X-band array antenna with low sidelobe and high aperture efficiency for small satellites," *International Journal of RF and Microwave Computer-Aided Engineering*, vol. 29, no. 11, p. e21914, 2019.

[58] T. Djerafi, A. Doghri, K. Wu, and Z. Chen, "Substrate integrated waveguide antennas," *Handbook of Antenna Technologies*, pp. 1585–1655, 2015.

[59] K. Wu, D. Deslandes, and Y. Cassivi, "The substrate integrated circuits-A new concept for high-frequency electronics and optoelectronics," in *6th International Conference on Telecommunications in Modern Satellite, Cable and Broadcasting Service, 2003. TELSIKS 2003.*, vol. 1, pp. P–III, IEEE, 2003.

[60] R. De, M. P. Abegaonkar, and A. Basu, "Compact dual slot SIW cavity backed antenna for CubeSat/nanosatellite applications," *IEEE Access*, vol. 11, pp. 78802–78810, 2023.

[61] M. Zawadzki and J. Huang, "Integrated RF antenna and solar array for spacecraft application," in *Proceedings 2000 IEEE International Conference on Phased Array Systems and Technology (Cat. No. 00TH8510)*, pp. 239–242, IEEE, 2000.

[62] J. Huang, "Capabilities of printed reflectarray antennas," in *Proceedings of International Symposium on Phased Array Systems and Technology*, pp. 131–134, IEEE, 1996.

[63] R. E. Hodges, D. J. Hoppe, M. J. Radway, and N. E. Chahat, "Novel deployable reflectarray antennas for CubeSat communications," in *2015 IEEE MTT-S International Microwave Symposium*, pp. 1–4, IEEE, 2015.

[64] S. Rao, L. Shafai, and S. K. Sharma, *Handbook of Reflector Antennas and Feed Systems Volume III: Applications of Reflectors*. Artech House, 2013.

[65] A. Babuscia, B. Corbin, M. Knapp, R. Jensen-Clem, M. Van de Loo, and S. Seager, "Inflatable antenna for CubeSats: Motivation for development and antenna design," *Acta Astronautica*, vol. 91, pp. 322–332, 2013.

[66] A. Babuscia, T. Choi, J. Sauder, A. Chandra, and J. Thangavelautham, "Inflatable antenna for CubeSats: Development of the X-band prototype," in *2016 IEEE Aerospace Conference*, pp. 1–11, IEEE, 2016.

[67] N. Chahat, R. E. Hodges, J. Sauder, M. Thomson, E. Peral, and Y. Rahmat-Samii, "CubeSat deployable Ka-band mesh reflector antenna development for Earth science missions," *IEEE Transactions on Antennas and Propagation*, vol. 64, no. 6, pp. 2083–2093, 2016.

[68] N. Chahat, J. Sauder, M. Mitchell, N. Beidleman, and G. Freebury, "One-meter deployable mesh reflector for deep-space network telecommunication at X-band and Ka-band," *IEEE Transactions on Antennas and Propagation*, vol. 68, no. 2, pp. 727–735, 2020.

[69] J. Huang and A. Feria, "Inflatable microstrip reflectarray antennas at X and Ka-band frequencies," in *IEEE Antennas and Propagation Society International Symposium. 1999 Digest. Held in conjunction with: USNC/URSI National Radio Science Meeting (Cat. No. 99CH37010)*, vol. 3, pp. 1670–1673, IEEE, 1999.

[70] J. Huang, G. Sadowy, C. Derksen, L. Del Castillo, P. Smith, J. Hoffman, T. Hatake, and A. Moussessian, "Aperture-coupled thin-membrane microstrip array antenna for beam scanning application," in *2005 IEEE Antennas and Propagation Society International Symposium*, vol. 1, pp. 330–333, IEEE, 2005.

[71] M. Arya, J. F. Sauder, R. Hodges, and S. Pellegrino, "Large-area deployable reflectarray antenna for CubeSats," in *AIAA Scitech 2019 Forum*, p. 2257, 2019.

[72] Canadian Space Agency, "CubeSat in a nutshell." `https://www.asc-csa.gc.ca/eng/satellites/cubesat/what-is-a-cubesat.asp`, 2024. Accessed: 2024-04-16.

[73] N. C. L. Initiative *et al.*, "CubeSat 101: Basic concepts and processes for first-time CubeSat developers," *NASA*, vol. 2017, p. 96, 2017.

[74] CubeSat, "The CubeSat Progam." `https://www.cubesat.org/`, 2024. Accessed: 2024-04-16.

[75] European Space Agency, "Technology CubeSats." `https://www.esa.int/Enabling_Support/Space_Engineering_Technology/Technology_CubeSats`, 2024. Accessed: 2024-04-16.

[76] International Telecommunication Union, "Space Services Department (SSD)." `https://www.itu.int/en/ITU-R/space/Pages/default.aspx`, 2024. Accessed: 2024-04-16.

[77] D. Pozar, "Wideband reflectarrays using artificial impedance surfaces," *Electronics letters*, vol. 43, no. 3, p. 1, 2007.

[78] S. S. Gao, Q. Luo, and F. Zhu, *Circularly polarized antennas*. John Wiley & Sons, 2014.

[79] K.-F. Lee and K.-F. Tong, "Microstrip patch antennas—basic characteristics and some recent advances," *Proceedings of the IEEE*, vol. 100, no. 7, pp. 2169–2180, 2012.

[80] F. Xu and K. Wu, "Guided-wave and leakage characteristics of substrate integrated waveguide," *IEEE Transactions on Microwave Theory and Techniques*, vol. 53, no. 1, pp. 66–73, 2005.

[81] A. P. Feresidis and J. Vardaxoglou, "High gain planar antenna using optimised partially reflective surfaces," *IEE Proceedings-Microwaves, Antennas and Propagation*, vol. 148, no. 6, pp. 345–350, 2001.

[82] V. G.-G. Buendía, S. K. Podilchak, D. Comite, P. Baccarelli, P. Burghignoli, J. L. G. Tornero, and G. Goussetis, "Compact leaky SIW feeder offering tem parallel plate waveguide launching," *IEEE Access*, vol. 7, pp. 13373–13382, 2019.

[83] A. J. Martinez-Ros, J. L. Gomez-Tornero, and G. Goussetis, "Planar leaky-wave antenna with flexible control of the complex propagation constant," *IEEE Transactions on Antennas and Propagation*, vol. 60, no. 3, pp. 1625–1630, 2012.

[84] L. Wang, J. L. Gómez-Tornero, and O. Quevedo-Teruel, "Substrate integrated waveguide leaky-wave antenna with wide bandwidth via prism coupling," *IEEE transactions on microwave theory and techniques*, vol. 66, no. 6, pp. 3110–3118, 2019.

[85] D. Deslandes and K. Wu, "Design consideration and performance analysis of substrate integrated waveguide components," in *2002 32nd European microwave conference*, pp. 1–4, IEEE, 2002.

[86] Z.-C. Hao, W. Hong, J. X. Chen, X. P. Chen, and K. Wu, "Planar diplexer for microwave integrated circuits," *IEE Proceedings-Microwaves, Antennas and Propagation*, vol. 152, no. 6, pp. 455–459, 2005.

[87] F. J. Zucker and R. C. Johnson, "Surface-wave antennas," *Antenna Engineering Handbook*, vol. 4, 2007.

[88] S. K. Podilchak, *Planar leaky-wave antennas and microwave circuits by practical surface wave launching*. PhD thesis, Queen's University, 2013.

[89] A. Cullen, "The excitation of plane surface waves," *Proceedings of the IEE-Part IV: Institution Monographs*, vol. 101, no. 7, pp. 225–234, 1954.

[90] C. A. Balanis, *Modern antenna handbook*. John Wiley & Sons, 2011.

[91] W. W. Hansen, "Radiating electromagnetic wave guide," June 25 1946. US Patent 2,402,622.

[92] J. Hines and J. Upson, "A wide aperture tapered-depth scanning antenna," *Ohio State Univ. Res. Found*, vol. 667, 1957.

[93] J. L. Volakis, *Antenna Engineering Handbook*. McGraw-Hill Education, 2007.

[94] W. Rotman and N. Karas, "The sandwich wire antenna: A new type of microwave line source radiator," in *1958 IRE International Convention Record*, vol. 5, pp. 166–172, IEEE, 1966.

[95] S. F. Mahmoud, S. K. Podilchak, Y. M. Antar, and A. P. Freundorfer, "Perturbation analysis of a planar periodic leaky-wave antenna fed by surface waves," *IEEE Antennas and Wireless Propagation Letters*, vol. 10, pp. 174–178, 2011.

[96] G. V. Trentini, "Partially reflecting sheet arrays," *IRE Transactions on antennas and propagation*, vol. 4, no. 4, pp. 666–671, 1956.

[97] H. Yang and N. Alexopoulos, "Gain enhancement methods for printed circuit antennas through multiple superstrates," *IEEE Transactions on Antennas and Propagation*, vol. 35, no. 7, pp. 860–863, 1987.

[98] N. Alexopoulos and D. Jackson, "Fundamental superstrate (cover) effects on printed circuit antennas," *IEEE Transactions on antennas and propagation*, vol. 32, no. 8, pp. 807–816, 1984.

[99] D. Jackson, P. Burghignoli, G. Lovat, and F. Capolino, "The role of leaky waves in fabry-pérot resonant cavity antennas," in *2014 IEEE-APS Topical Conference on Antennas and Propagation in Wireless Communications (APWC)*, pp. 786–789, IEEE, 2014.

[100] T. Zhao, D. R. Jackson, J. T. Williams, H.-Y. Yang, and A. A. Oliner, "2-D periodic leaky-wave antennas-part I: metal patch design," *IEEE Transactions on Antennas and Propagation*, vol. 53, no. 11, pp. 3505–3514, 2005.

[101] F. K. Schwering and S.-T. Peng, "Design of dielectric grating antennas for millimeter-wave applications," *IEEE Transactions on Microwave Theory and Techniques*, vol. 31, no. 2, pp. 199–209, 1983.

[102] M. Guglielmi and A. Oliner, "A practical theory for dielectric image guide leaky-wave antennas loaded by periodic metal strips," in *1987 17th European Microwave Conference*, pp. 549–554, IEEE, 1987.

[103] C.-H. Kim, M.-Y. Li, and K. Chang, "Image-guide leaky-wave antenna with wide beam-scan angle," in *2009 IEEE Antennas and Propagation Society International Symposium*, pp. 1–4, IEEE, 2009.

[104] D. Deslandes, "Design equations for tapered microstrip-to-substrate integrated waveguide transitions," in *2010 IEEE MTT-S International Microwave Symposium*, pp. 704–707, IEEE, 2010.

[105] A. J. Martinez-Ros, J. L. Gómez-Tornero, and F. Quesada-Pereira, "Efficient analysis and design of novel SIW leaky-wave antenna," *IEEE Antennas and Wireless Propagation Letters*, vol. 12, pp. 496–499, 2013.

[106] A. Ip and D. R. Jackson, "Radiation from cylindrical leaky waves," *IEEE Transactions on Antennas and Propagation*, vol. 38, no. 4, pp. 482–488, 1990.

[107] D. R. Jackson and A. A. Oliner, "A leaky-wave analysis of the high-gain printed antenna configuration," *IEEE Transactions on Antennas and Propagation*, vol. 36, no. 7, pp. 905–910, 1988.

[108] F. Mesa and D. R. Jackson, "Leaky modes and high-frequency effects in microwave integrated circuits," *Encyclopedia of RF and Microwave Engineering*, 2005.

[109] T. Tamir and A. A. Oliner, "Guided complex waves. part 1: Fields at an interface," in *Proceedings of the Institution of Electrical Engineers*, vol. 110, pp. 310–324, IET, 1963.

[110] K. M. Alrushud, V. G.-G. Buendía, and S. K. Podilchak, "Compact substrate integrated waveguide quasi-endfire antenna for CubeSat integration," *IEEE Antennas and Wireless Propagation Letters*, vol. 20, no. 11, pp. 2120–2124, 2021.

[111] Y. Rahmat-Samii, V. Manohar, J. M. Kovitz, R. E. Hodges, G. Freebury, and E. Peral, "Development of highly constrained 1 m Ka-band mesh deployable offset reflector antenna for next generation CubeSat radars," *IEEE Transactions on Antennas and Propagation*, vol. 67, no. 10, pp. 6254–6266, 2019.

[112] "Maritime monitoring and messaging microsatellite (M3MSat) mission." `https://www.asc-csa.gc.ca/eng/satellites/m3msat/default.asp`. Accessed: 2024-04-16.

[113] J. Huang and A. Densmore, "Microstrip yagi array antenna for mobile satellite vehicle application," *IEEE Transactions on Antennas and Propagation*, vol. 39, no. 7, pp. 1024–1030, 1991.

[114] W.-J. Lu, J.-W. Shi, K.-F. Tong, and H.-B. Zhu, "Planar endfire circularly polarized antenna using combined magnetic dipoles," *IEEE Antennas and Wireless Propagation Letters*, vol. 14, pp. 1263–1266, 2015.

[115] V. Gómez-Guillamón Buendía, S. K. Podilchak, S. Liberto, D. E. Anagnostou, G. Goussetis, C. Constantinides, T. Walkinshaw, and M. van der Vorst, "Compact end-fire antenna designs for PicoSat integration and other small satellite missions," in *2020 50th European Microwave Conference (EuMC)*, pp. 463–466, 2021.

[116] S. Liu, R. Raad, P. I. Theoharis, and F. E. Tubbal, "A printed yagi antenna for CubeSat with multi-frequency tilt operation," *Electronics*, vol. 9, no. 6, 2020.

[117] D. Deslandes and K. Wu, "Single-substrate integration technique of planar circuits and waveguide filters," *IEEE Transactions on microwave theory and Techniques*, vol. 51, no. 2, pp. 593–596, 2003.

[118] K. Wu, M. Bozzi, and N. J. Fonseca, "Substrate integrated transmission lines: Review and applications," *IEEE Journal of Microwaves*, vol. 1, no. 1, pp. 345–363, 2021.

[119] V. G.-G. Buendia, S. K. Podilchak, G. Goussetis, and J.-L. Gomez-Tornero, "A TM_0 surface wave launcher by microstrip and substrate integrated waveguide technology," in *2017 11th European Conference on Antennas and Propagation (EUCAP)*, pp. 3859–3862, IEEE, 2017.

[120] S. K. Podilchak, P. Baccarelli, P. Burghignoli, A. P. Freundorfer, and Y. M. M. Antar, "Analysis and design of annular microstrip-based planar periodic leaky-wave antennas," *IEEE Transactions on Antennas and Propagation*, vol. 62, no. 6, pp. 2978–2991, 2014.

[121] S. Germain, D. Deslandes, and K. Wu, "Development of substrate integrated waveguide power dividers," in *CCECE 2003-Canadian Conference on Electrical and Computer Engineering. Toward a Caring and Humane Technology*, vol. 3, pp. 1921–1924, IEEE, 2003.

[122] J. L. G. Tornero, A. M. Ros, M. A. Martinez, A. M. Sala, G. Goussetis, and S. K. Podilchak, "A simple parallel-plate wave launcher in substrate integrated waveguide technology," in *2015 IEEE International Symposium on Antennas and Propagation & USNC/URSI National Radio Science Meeting*, pp. 480–481, IEEE, 2015.

[123] P. Burghignoli, G. Lovat, and D. R. Jackson, "Analysis and optimization of leaky-wave radiation at broadside from a class of 1-D periodic structures," *IEEE Transactions on Antennas and Propagation*, vol. 54, no. 9, pp. 2593–2604, 2006.

[124] N. Saeed, A. Elzanaty, H. Almorad, H. Dahrouj, T. Y. Al-Naffouri, and M.-S. Alouini, "CubeSat communications: Recent advances and future challenges," *IEEE Communications Surveys & Tutorials*, vol. 22, no. 3, pp. 1839–1862, 2020.

[125] Nanosats Database, "NanoSatellite and CubeSat Database." `https://www.nanosats.eu/database`, 2024. Accessed: 2024-04-16.

[126] G. Valerio, S. Paulotto, P. Baccarelli, P. Burghignoli, and A. Galli, "Accurate bloch analysis of 1-D periodic lines through the simulation of truncated structures," *IEEE transactions on antennas and propagation*, vol. 59, no. 6, pp. 2188–2195, 2011.

[127] N. Apaydin, L. Zhang, K. Sertel, and J. L. Volakis, "Experimental validation of frozen modes guided on printed coupled transmission lines," *IEEE transactions on microwave theory and techniques*, vol. 60, no. 6, pp. 1513–1519, 2012.

[128] Rogers Corporation, "Communication Systems." `https://www.rogerscorp.com/applications/communication-systems`, 2024. Accessed: 2024-04-16.

[129] O. Luukkonen, C. Simovski, G. Granet, G. Goussetis, D. Lioubtchenko, A. V. Raisanen, and S. A. Tretyakov, "Simple and accurate analytical model of planar grids and high-impedance surfaces comprising metal strips or patches," *IEEE Transactions on Antennas and Propagation*, vol. 56, no. 6, pp. 1624–1632, 2008.

[130] S. Podilchak, G. Labate, and L. Matekovits, "Controlling surface waves by introducing anisotropy into the conductive backing of planar dielectric slabs," in *2015 International Conference on Electromagnetics in Advanced Applications (ICEAA)*, pp. 1427–1428, IEEE, 2015.

[131] D. Deslandes and K. Wu, "Integrated microstrip and rectangular waveguide in planar form," *IEEE microwave and wireless components letters*, vol. 11, no. 2, pp. 68–70, 2001.

[132] E. D. Caballero, A. B. Martinez, H. E. Gonzalez, O. M. Belda, and V. B. Esbert, "A novel transition from microstrip to a substrate integrated waveguide with higher characteristic impedance," in *2013 IEEE MTT-S International Microwave Symposium Digest (MTT)*, pp. 1–4, IEEE, 2013.

[133] R. C. Caleffo, "New design procedure to determine the taper transition for impedance matching between microstrip line and SIW component," *Journal of Microwaves, Optoelectronics and Electromagnetic Applications*, vol. 15, pp. 247–260, 2016.

[134] Rogers Corporation, "RT/duroid® 5880 Laminates." `https://www.rogerscorp.com/advanced-electronics-solutions/rt-duroid-laminates/rt-duroid-5880-laminates`, 2024. Accessed: 2024-04-16.

[135] R. Garg, P. Bhartia, and A. Ittipiboon, "Microstrip antenna design handbook," 2000.

[136] N. Alexopoulos, "Integrated-circuit structures on anisotropic substrates," *IEEE Transactions on Microwave Theory and Techniques*, vol. 33, no. 10, pp. 847–881, 1985.

[137] D. Pozar, "Radiation and scattering from a microstrip patch on a uniaxial substrate," *IEEE Transactions on Antennas and Propagation*, vol. 35, pp. 613–621, 1987.

[138] M. M. S. Taheri, A. Abdipour, S. Zhang, and G. F. Pedersen, "Integrated millimeter-wave wideband end-fire 5G beam steerable array and low-frequency 4G LTE antenna in mobile terminals," *IEEE Transactions on Vehicular Technology*, vol. 68, no. 4, pp. 4042–4046, 2019.

[139] P. Wang, Q. Wu, R.-B. He, and Y. Shao, "Design of low profile and wideband end-fire antenna using metasurface," *IEEE Access*, vol. 8, pp. 35752–35758, 2020.

[140] J. Zhang, K. Zhao, L. Wang, S. Zhang, and G. F. Pedersen, "Dual-polarized phased array with end-fire radiation for 5G handset applications," *IEEE Transactions on Antennas and Propagation*, vol. 68, no. 4, pp. 3277–3282, 2019.

[141] A. Li and K.-M. Luk, "Millimeter-wave end-fire magneto-electric dipole antenna and arrays with asymmetrical substrate integrated coaxial line feed," *IEEE Open Journal of Antennas and Propagation*, vol. 2, pp. 62–71, 2020.

[142] A. A. Omar, J. Park, W. Kwon, and W. Hong, "A compact wideband vertically polarized end-fire millimeter-wave antenna utilizing slot, dielectric, and cavity resonators," *IEEE Transactions on Antennas and Propagation*, vol. 69, no. 9, pp. 5234–5243, 2021.

[143] N. O. Parchin, J. Zhang, R. A. Abd-Alhameed, G. F. Pedersen, and S. Zhang, "A planar dual-polarized phased array with broad bandwidth and quasi end-fire radiation for 5G mobile handsets," *IEEE Transactions on Antennas and Propagation*, 2021.

[144] D. C. Lugo, R. A. Ramirez, J. Wang, and T. M. Weller, "Multilayer dielectric end-fire antenna with enhanced gain," *IEEE Antennas and Wireless Propagation Letters*, vol. 17, no. 12, pp. 2213–2217, 2018.

[145] J. Liu, "Substrate integrated surface-wave antenna," *IEEE Transactions on Antennas and Propagation*, vol. 67, no. 8, pp. 5221–5230, 2019.

[146] J. Liang and J. Liu, "A low-profile planar surface-wave antenna with metasurface for endfire radiation," *IEEE Antennas and Wireless Propagation Letters*, vol. 19, no. 12, pp. 2452–2456, 2020.

[147] Z. Chen, R. Xu, and Z. Shen, "Design of a broadband antenna array with compact surface-wave antenna elements," *IEEE Antennas and Wireless Propagation Letters*, vol. 21, no. 2, pp. 337–340, 2021.

[148] Y. Hou, Y. Li, Z. Zhang, and M. F. Iskander, "Microstrip-fed surface-wave antenna for endfire radiation," *IEEE Transactions on Antennas and Propagation*, vol. 67, no. 1, pp. 580–584, 2018.

[149] Z. Chen and Z. Shen, "Wideband flush-mounted surface wave antenna of very low profile," *IEEE Transactions on Antennas and Propagation*, vol. 63, no. 6, pp. 2430–2438, 2015.

[150] V. G.-G. Buendía, S. K. Podilchak, S. Liberto, T. Walkinshaw, C. Constantinides, D. E. Anagnostou, G. Goussetis, and M. Van Der Vorst, "Compact and planar end-fire antenna for PicoSat and CubeSat platforms to support deployable systems," *IEEE Open Journal of Antennas and Propagation*, vol. 3, pp. 1341–1350, 2022.

[151] V. Gómez-Guillamón Buendía, S. K. Podilchak, S. Liberto, D. E. Anagnostou, G. Goussetis, C. Constantinides, T. Walkinshaw, and M. van der Vorst, "Compact end-fire antenna designs for PicoSat integration and other small satellite missions," in *2020 50th European Microwave Conference (EuMC)*, pp. 463–466, 2021.

[152] M. V. Kuznetcov, S. K. Podilchak, M. Poveda-García, P. Hilario, C. A. Alistarh, G. Goussetis, and J. L. Gómez-Tornero, "Compact leaky-wave SIW antenna with broadside radiation and dual-band operation for CubeSats," *IEEE Antennas and Wireless Propagation Letters*, vol. 20, no. 11, pp. 2125–2129, 2021.

[153] N. Marcuvitz, *Waveguide handbook*. New York, NY: McGraw-Hill, 1951.

[154] Y. Cai, Y. Zhang, Z. Qian, W. Cao, and L. Wang, "Design of compact air-vias-perforated SIW horn antenna with partially detached broad walls," *IEEE Transactions on Antennas and Propagation*, vol. 64, no. 6, pp. 2100–2107, 2016.

[155] S. K. Podilchak, L. Matekovits, A. P. Freundorfer, Y. M. M. Antar, and M. Orefice, "Controlled leaky-wave radiation from a planar configuration of width-modulated microstrip lines," *IEEE Transactions on Antennas and Propagation*, vol. 61, no. 10, pp. 4957–4972, 2013.

[156] Y. Cai, Z.-P. Qian, Y.-S. Zhang, J. Jin, and W.-Q. Cao, "Bandwidth enhancement of SIW horn antenna loaded with air-via perforated dielectric slab," *IEEE Antennas and Wireless Propagation Letters*, vol. 13, pp. 571–574, 2014.

[157] Y. Cai, Z. Qian, W. Cao, Y. Zhang, J. Jin, L. Yang, and N. Jing, "Compact wideband SIW horn antenna fed by elevated-CPW structure," *IEEE Transactions on Antennas and Propagation*, vol. 63, no. 10, pp. 4551–4557, 2015.

[158] Y. Cai, Y. Zhang, L. Yang, Y. Cao, and Z. Qian, "A low-profile wideband surface-mountable substrate-integrated waveguide horn antenna," *IEEE Antennas and Wireless Propagation Letters*, vol. 16, pp. 2730–2733, 2017.

[159] W. Li, S. Liu, X. Kong, S. Zhang, and R. Yang, "A SIW horn antenna without broad wall loaded with air-vias-perforated in arcuate arrangement," in *2019 International Conference on Microwave and Millimeter Wave Technology (ICMMT)*, pp. 1–2, IEEE, 2019.

[160] B. Hu, T. Wu, Y. Cai, W. Zhang, and B.-L. Zhang, "A novel metamaterial-based planar integrated luneburg lens antenna with wide bandwidth and high gain," *IEEE access*, vol. 8, pp. 4708–4713, 2019.

[161] X. Wang, Y. Pan, and Y. Dong, "An E-plane-focused triple-layer multibeam luneburg lens antenna for 5G millimeter-wave applications," *IEEE Antennas and Wireless Propagation Letters*, vol. 21, no. 2, pp. 227–231, 2021.

[162] R. E. Collin, *Field theory of guided waves*, vol. 5. John Wiley & Sons, 1990.

[163] K. Alrushud, B. Alshammari, and S. K. Podilchak, "Towards optically semi-transparent planar endfire antennas for CubeSats and other small satellites," in *2023 IEEE Conference on Antenna Measurements and Applications (CAMA)*, pp. 674–676, IEEE, 2023.

[164] Z. Shafiq, M. Kuznetcov, V. G.-G. Buendia, D. E. Anagnostou, and S. K. Podilchak, "A planar horn antenna for TM surface wave launching using substrate integrated waveguide technology," in *2019 13th European Conference on Antennas and Propagation (EuCAP)*, pp. 1–3, IEEE, 2019.

[165] M. V. Kuznetcov, V. G.-G. Buendía, Z. Shafiq, L. Matekovits, D. E. Anagnostou, and S. K. Podilchak, "Printed leaky-wave antenna with aperture control using width-modulated microstrip lines and TM surface-wave feeding by SIW technology," *IEEE Antennas and Wireless Propagation Letters*, vol. 18, no. 9, pp. 1809–1813, 2019.

[166] M. Kuznetcov, V. G.-G. Buendía, K. Alrushud, and S. K. Podilchak, "Simple matching technique using finite metasurface to control surface waves," in *2022 16th European Conference on Antennas and Propagation (EuCAP)*, pp. 1–5, IEEE, 2022.

[167] R. Yang, Z. Lei, L. Chen, Z. Wang, and Y. Hao, "Surface wave transformation lens antennas," *IEEE Transactions on Antennas and Propagation*, vol. 62, no. 2, pp. 973–977, 2014.

[168] K. Wang, Y. Li, Z. Liang, S. Y. Zheng, and Y. Long, "A high-gain endfire periodic leaky-wave antenna using dspsl-based rhombic element," *IEEE Transactions on Antennas and Propagation*, vol. 70, no. 11, pp. 11109–11114, 2022.